Target-oriented seismic imaging and inversion with marchenko redatuming and double-focusing

Shoja, S.M. Aydin

Important note
To cite this publication, please use the final published version (if applicable).
Please check the document version above.

TARGET-ORIENTED SEISMIC IMAGING AND INVERSION WITH MARCHENKO REDATUMING AND DOUBLE-FOCUSING

Dissertation

for the purpose of obtaining the degree of doctor
at Delft University of Technology
by the authority of the Rector Magnificus, prof. dr. ir. T.H.J.J. van der Hagen,
chair of the Board for Doctorates
to be defended publicly on
Monday 18 December 2023 at 17:30 o'clock

by

Seyed Mohammad Aydin SHOJA

Master of Science in Geophysics, University of Tehran, Iran
born in Kerman, Iran

This dissertation has been approved by the promotors.

Composition of the doctoral committee:

Rector Magnificus	chairperson
Prof. dr. ir. C.P.A. Wapenaar	Delft University of Technology, *promotor*
Prof. dr. ir. E.C. Slob	Delft University of Technology, *promotor*

Independent members:

Prof. dr. L.G. Evers	Delft University of Technology
Prof. dr. R.K. Snieder	Colorado School of Mines, USA
Dr. ir. D.J. Verschuur	Delft University of Technology
Dr. K. Loër	Delft University of Technology
Dr. I. Pires de Vasconcelos	Shearwater GeoServices, UK
Prof. dr. P.J. Vardon	Delft University of Technology, reserve member

An electronic copy of this dissertation is available at https://repository.tudelft.nl/.

CONTENTS

SUMMARY

Reflection seismology aims to estimate the Earth's subsurface elastic parameters for further investigation by geologists and engineers. This involves generating elastic waves using seismic sources and recording the Earth's response with receivers. The subsurface model is typically considered a combination of a background model and a short-wavelength reflectivity model. There are two main paths to estimate these parameters: non-linear waveform inversion to directly compute the elastic parameters or depth migration to estimate a structural image or reflectivity of the subsurface.

Reverse-Time Migration (RTM) is a common depth migration technique that migrates recorded wavefields from the space-time domain to the space-depth domain. It utilizes the Born approximation and the adjoint of the Born operator to produce an RTM image. However, RTM can suffer from errors, such as noise, temporal and spatial limitations, and multiple reflections.

Least-Squares Reverse-Time Migration (LSRTM) is used to overcome some of these errors. LSRTM involves resolving the reflectivity model by least-squares inversion, which is computationally expensive. Gradient-based optimization algorithms are often employed to reduce the computational burden, but they still require solving the wave equation and its adjoint for a large model in multiple iterations. One way to reduce the computational cost is by limiting the computational domain to a target region of interest.

Target-oriented LSRTM, known as TOLSRTM, focuses on the wavefield just above the target by bypassing the overburden. This approach proves beneficial when the overburden generates strong internal multiple reflections that obscure the reflections from the target area. However, a redatuming method is required to predict all orders of multiples. Marchenko redatuming is a data-driven technique that predicts the Green's functions at the boundary of the target region, incorporating all orders of internal multiples. It allows for double-sided redatuming, considering both the source and receiver perspectives. By combining the LSRTM algorithm and Marchenko double-focusing, a target-oriented LSRTM algorithm is devised that can predict interactions between the target and overburden and remove the effects of the overburden in the image. Predicting these interactions results in an artifact-free image, a better convergence rate, and a high-resolution image of the target.

Target-oriented migration algorithms typically consider only the upper horizontal boundary of the region of interest (ROI), neglecting wavefields entering the ROI from the medium beneath the lower boundary. To address this, a target-enclosed LSRTM algorithm is proposed, including both the ROI's upper and lower boundaries. Including the lower

boundary provides transmission information and can improve inversion convergence. In addition, this algorithm is adopted for virtual receivers created by Marchenko redatuming. In the case of physical receivers at the boundaries of the target zone, the target-enclosed algorithm can incorporate the transmission information emanating from the lower boundary to the upper one. Consequently, when the initial model is far from the actual model, the resulting image partly recovers the long wavelength part of the model in agreement with the Born approximation criteria. Moreover, when an initial model closer to the actual model is used, the algorithm can partially recover the vertical interfaces of the perturbation. In the case of virtual receivers at the boundaries of the target zone, since the Marchenko redatuming is performed in the initial background model, the redatumed wavefields at the lower boundary suffer from kinematic errors. Therefore, the algorithm can not recover the long wavelength part of the model.

The thesis concludes with a discussion of the results obtained from applying the algorithms to marine datasets. The images resulting from the Marchenko double-focusing based target-oriented LSRTM algorithm show improvements in both resolution and artifact reduction by suppressing the overburden generated internal multiple effects. Moreover, the double-focusing enables the user to reduce the computational costs of the LSRTM algorithm and choose finer spatial sampling for the image.

An appendix proposes a formulation for integrating the target-oriented algorithms with non-linear inversion like Full Waveform Inversion (FWI). The results of this proposed algorithm show its effectiveness by reducing the internal multiple related artifacts and increasing resolution and faster convergence.

SAMENVATTING

Reflectieseismologie heeft als doel de elastische eigenschappen van de ondergrond van de aarde te schatten voor verder onderzoek door geologen en ingenieurs. Dit omvat het genereren van elastische golven met behulp van seismische bronnen en het registreren van de respons van de aarde met ontvangers. Het is gebruikelijk om onderscheid te maken tussen een achtergrondmodel en een korte-golflengte reflectiviteitsmodel. Er zijn twee belangrijke manieren om deze parameters te schatten: niet-lineaire golfvorm inversie om rechtstreeks de elastische parameters te berekenen, of dieptemigratie om een structureel beeld of de reflectiviteit van de ondergrond te verkrijgen.

Reverse-Time Migratie (RTM) is een veelgebruikte techniek voor dieptemigratie die geregistreerde golfvelden migreert van het plaats-tijd domein naar het plaats-diepte domein. Hierbij wordt gebruik gemaakt van de Born-benadering en de adjoint van de Born-operator om een RTM-beeld te produceren. RTM kan echter te maken krijgen met fouten zoals ruis, temporele en ruimtelijke beperkingen, en meervoudige reflecties.

Least-Squares Reverse-Time Migratie (LSRTM) wordt gebruikt om enkele van deze fouten te voorkomen. LSRTM houdt in dat het reflectiviteitsmodel wordt geschat door middel van least-squares inversie, wat veel rekenkracht vergt. Optimalisatie-algoritmen die zijn gebaseerd op gradiëntmethoden worden vaak gebruikt om de rekenlast te verminderen, maar ze vereisen nog altijd het oplossen van de golfvergelijking en de adjoint ervan voor een groot model in meerdere iteraties. Een manier om de rekentijd terug te dringen is om het rekengebied te beperken tot een kleiner interessegebied.

Doelgerichte LSRTM, bekend als TOLSRTM, richt zich op het golfveld net boven het interessegebied door de bovenliggende lagen over te slaan. Deze aanpak is voordelig wanneer de bovenliggende lagen sterke interne meervoudige reflecties genereren die de reflecties van het interessegebied verbergen. Er is echter een redatuming-methode nodig om alle ordes van meervoudige reflecties te voorspellen. Marchenko-redatuming is een datagedreven techniek die de Greense-functies voorspelt op de grens van het interessegebied, waarbij alle ordes van interne meervoudige reflecties worden meegenomen. Hiermee is tweezijdige redatuming mogelijk, vanuit zowel het bron- als ontvanger-perspectief. Door het LSRTM-algoritme en Marchenko dubbele focussering te combineren, is een doelgericht LSRTM-algoritme ontwikkeld dat de interacties tussen het interessegebied en de bovenliggende lagen kan voorspellen en de effecten van de bovenliggende lagen in het beeld kan verwijderen.

Doelgerichte migratie-algoritmen houden meestal alleen rekening met de bovenste horizontale begrenzing van het interessegebied (ROI), waarbij golfvelden die het ROI bin-

nenkomen vanuit het medium onder de onderste begrenzing worden genegeerd. Om dit aan te pakken, wordt een doelomsloten LSRTM-algoritme voorgesteld, waarbij zowel de bovenste als de onderste begrenzingen van het ROI worden opgenomen. Het opnemen van de onderste begrenzing verschaft transmissie-informatie en kan de convergentie van de inversie verbeteren. Verder wordt dit algoritme toegepast op virtuele ontvangers die zijn gecreëerd door Marchenko-redatuming.

Het proefschrift wordt afgesloten met een bespreking van de resultaten die zijn verkregen door de algoritmen toe te passen op mariene datasets. In een appendix wordt een formulering voorgesteld voor het integreren van de doelgerichte algoritmen met niet-lineaire inversietechnieken zoals Full Waveform Inversion (FWI).

1

INTRODUCTION

The goal of exploration seismology is to estimate the Earth's subsurface elastic parameters and pass them to the geologists and engineers for more investigation. The first step to estimate these parameters is to generate elastic waves with active seismic sources and record Earth's response with receivers. It is common to consider the model of the subsurface as a superposition of a background model (m_0), which corresponds to the long wavelengths, and a short-wavelength perturbation model (δm). After preprocessing the recorded wavefields, there are two paths to estimate the parameters; One path is to directly compute the elastic parameters through non-linear waveform inversion, where the parameter $m = m_0 + \delta m$ is estimated. Another path is to estimate a structural image or the reflectivity (δm) of the subsurface by means of depth migration.

1.1. LEAST-SQUARES REVERSE-TIME MIGRATION

Depth migration is a process in which the recorded wavefields in the space-time domain are migrated to their origin in the space-space domain [1]. A depth migration process is based on a linear relationship between the recorded data and the perturbation model (δm). Since this process includes a time-to-depth conversion, it requires a velocity model. One of the common depth migration techniques is called Reverse-Time Migration (RTM) [2–4]. In RTM, the underlying linear relation is the Born approximation of the Lippmann-Schwinger integral, so the RTM image is produced by applying the adjoint of the Born operator to the observed data. As a result of being directly derived from the two-way wave equation, the RTM formulation gives the an accurate imaging result [5]. However, this approach may suffer from many errors such as noise [6], temporal band limitations, limited recording aperture [7], spatial aliasing, and multiple reflections [8].

As mentioned above, RTM uses the adjoint of the Born operator, which is an approximation of its inverse. One way to compute the inverse of the operator and reduce some of the named errors is to resolve δm by least-squares inversion. This approach, known as Least-Squares Reverse-Time Migration (LSRTM), is a common algorithm for producing a high-resolution perturbation model of the subsurface.

1

Nevertheless, LSRTM is computationally expensive [9] as it requires computing the Hessian matrix. To avoid computing the Hessian matrix, researchers opt for gradient-based optimization algorithms [10]. Nevertheless, these optimization algorithms require solving the wave equation and its adjoint for a large model in many iterations and storing large data volumes [7, 11, 12], which is computationally expensive. Reducing the computational burden of LSRTM is possible by reducing the computational domain. In other words, limiting ourselves to a relatively small target region of interest.

1.2. TARGET-ORIENTED LEAST-SQUARES REVERSE-TIME MIGRATION

The "target-oriented" approach [13–18] divides the medium into two parts: an overburden and a target. To achieve this, the target-oriented LSRTM, referred to as TOLSRTM, focuses on the wavefield above the target by bypassing the overburden. The process of extrapolating the wavefield from its current acquisition surface to another surface is known as redatuming [19–22].

Aside from its computational advantages, target-oriented LSRTM proves beneficial in scenarios where the overburden generates strong internal multiple reflections that obscure the reflections from the target area. However, for this method to function accurately, a reliable model of the overburden capable of producing reflections of all orders is required. The inaccuracies in overburden models and the artifacts caused by internal multiple reflections in LSRTM images have garnered significant attention from researchers. Guo and Alkhalifah [18, 23], for instance, introduced a least-squares waveform redatuming technique that redatums the data to the target boundary and combines it with full waveform inversion.

1.3. TARGET-ORIENTED LEAST-SQUARES REVERSE-TIME MIGRATION WITH MARCHENKO DOUBLE-FOCUSING

Marchenko redatuming has emerged as a promising data-driven technique for predicting the Green's functions at the boundary of the target region, encompassing all orders of internal multiples [24–28]. This method enables the prediction of internal multiples by utilizing the reflection response at the surface, in combination with the direct arrival between the surface and the target boundary in a smooth background velocity model of the overburden. By solving the Marchenko equations, we obtain the medium's response stimulated by virtual sources located at the target boundary and recorded by receivers at the surface, incorporating all multiple reflections.

Consequently, the initial step of Marchenko redatuming can be seen as source-side redatuming within the physical medium, considering reflections in the overburden that are not accounted for in the background model. Diekmann et al. [29] employed

Marchenko equations to predict the in-volume Green's function of a target of interest, utilizing this wavefield as the incident wavefield in the Lippmann-Schwinger integral. Similarly, Cui et al. [30] utilized the reciprocity theorem to derive a forward modeling equation based on Marchenko wavefields for Full waveform inversion.

An additional outcome of the Marchenko integrals is the downgoing component of the focusing function, which represents the inverse of the transmission response of the overburden. This focusing function can also be applied on the receiver side to achieve double-sided redatuming, encompassing both the source and receiver perspectives. This process, known as Marchenko double-focusing, employs the Marchenko focusing function to enable double-sided redatuming [31].

1.4. TARGET-ENCLOSED LEAST-SQUARES REVERSE-TIME MIGRATION

The conventional approach for target-oriented migration typically employs redatuming algorithms that consider only the upper horizontal boundary of the Region of Interest (ROI) or target [18, 20, 21, 23–25, 27, 32]. This approach overlooks situations where the ROI is bounded by two boundaries, leading to a situation where wavefields entering the ROI from the medium beneath the lower boundary of the ROI are disregarded. This omission hampers the convergence of the inversion process. Additionally, incorporating the lower boundary in the algorithm can provide transmission information to the inversion. However, the direct study of including the lower boundary in the inversion process has been rarely explored.

Notably, Cui et al. [30] present a representation using a reciprocity theorem and Marchenko redatuming to include surrounding boundaries in target-oriented Full Waveform Inversion (FWI). Diekmann et al. [33] utilize a Marchenko-retrieved Green's function of the ROI and integrate it into the Lippmann-Schwinger integral, establishing a linear inversion process. Van der Neut et al. [34] devise a target-enclosed imaging algorithm with the aid of a reciprocity theorem. Among these papers, only van der Neut et al. [34] directly investigate the consequences of including the lower boundary in the imaging process, while the others merely imply its effects implicitly.

Recently, Zheglova et al. [35] introduce a target-enclosed FWI algorithm based on an interferometric objective function, which solely relies on kinematic information from the overburden and does not necessitate prior knowledge of the underburden.

1.5. OUTLINE OF THIS THESIS

In this thesis, we address the following question: How to develop a method capable of predicting the multiple scatterings and integrate it into the formalism of LSRTM to improve its functionality?

1

Chapter 2 of the thesis presents the development of the Marchenko double-focusing target-oriented LSRTM algorithm. The upgoing Marchenko double-focused data is considered as the "observed data" and is utilized as input for the LSRTM algorithm. The TOLSRTM algorithm is completed by formulating a forward modeling process that matches the Marchenko double-focused data with the predicted data of the target region. This forward modeling incorporates the downgoing wavefields from the Marchenko equation and a Born model of the target, utilizing the Marchenko downgoing wavefield as a virtual source for modeling and inversion. This algorithm offers the advantage of predicting all interactions between the target and the overburden, resulting in less degraded and high-resolution images.

Chapter 3 extends the work of [34] and investigates the contribution of the lower boundary by introducing a target-enclosed LSRTM algorithm. The chapter begins with a brief explanation of LSRTM and then derives a target-enclosed representation for Green's functions on the upper and lower boundaries of the Region of Interest (ROI) using the reciprocity theorem. This target-enclosed representation is connected to LSRTM to establish the algorithm. The derived equations are tested using numerical examples, initially employing physical receivers at the ROI boundaries to assess the results in an ideal scenario. Additionally, the potential of using virtual receivers in the algorithm is explored briefly by employing Marchenko redatuming. Both physical and virtual receiver cases are evaluated using a homogeneous background and a smooth background velocity model for migration.

Chapter 4 applies the Marchenko double-focusing target-oriented LSRTM algorithm to generate high-resolution and artifact-free images of a marine dataset from the Vøring region in the Norwegian Sea.

Chapter 5 presents the concluding remarks of the thesis.

The thesis also includes an Appendix proposing a formulation that can facilitate the integration of the target-oriented algorithm presented in this thesis with non-linear inversions, such as Full Waveform Inversion (FWI).

REFERENCES

[1] J. F. Claerbout. *Imaging the Earth's Interior*. BlackWell Scientific Publications, 1985.

[2] E. Baysal, D. D. Kosloff and J. W. C. Sherwood. 'Reverse time migration'. In: *GEOPHYSICS* 48.11 (1983), pp. 1514–1524. DOI: 10.1190/1.1441434.

[3] H.-W. Zhou, H. Hu, Z. Zou, Y. Wo and O. Youn. 'Reverse time migration: A prospect of seismic imaging methodology'. In: *Earth-Science Reviews* 179 (2018), pp. 207–227. DOI: https://doi.org/10.1016/j.earscirev.2018.02.008.

[4] L. Zhang, E. Slob, J. van der Neut and K. Wapenaar. 'Artifact-free reverse time migration'. In: *GEOPHYSICS* 83.5 (2018), A65–A68. DOI: 10.1190/geo2017-0795.1.

[5] J. B. Bednar. 'A brief history of seismic migration'. In: *GEOPHYSICS* 70.3 (2005), 3MJ–20MJ. DOI: 10.1190/1.1926579.

[6] G. Dutta, M. Giboli, C. Agut, P. Williamson and G. T. Schuster. 'Least-squares reverse time migration with local Radon-based preconditioning'. In: *GEOPHYSICS* 82.2 (2017), S75–S84. DOI: 10.1190/geo2016-0117.1.

[7] Y. Tang. 'Target-oriented wave-equation least-squares migration/inversion with phase-encoded Hessian'. In: *GEOPHYSICS* 74.6 (2009), WCA95–WCA107. DOI: 10.1190/1.3204768.

[8] Y. Liu, X. Liu, A. Osen, Y. Shao, H. Hu and Y. Zheng. 'Least-squares reverse time migration using controlled-order multiple reflections'. In: *GEOPHYSICS* 81.5 (2016), S347–S357. DOI: 10.1190/geo2015-0479.1.

[9] W. Dai, P. Fowler and G. T. Schuster. 'Multi-source least-squares reverse time migration'. In: *Geophysical Prospecting* 60.4 (2012), pp. 681–695. DOI: https://doi.org/10.1111/j.1365-2478.2012.01092.x.

[10] J. Nocedal and S. J. Wright. *Numerical optimization*. Springer, 2006.

[11] F. J. Herrmann and X. Li. 'Efficient least-squares imaging with sparsity promotion and compressive sensing'. In: *Geophysical Prospecting* 60.4 (2012), pp. 696–712. DOI: https://doi.org/10.1111/j.1365-2478.2011.01041.x.

[12] M. Farshad and H. Chauris. 'Sparsity-promoting multiparameter pseudoinverse Born inversion in acoustic media'. In: *GEOPHYSICS* 86.3 (2021), S205–S220. DOI: 10.1190/geo2020-0527.1.

[13] A. A. Valenciano, B. Biondi and A. Guitton. 'Target-oriented wave-equation inversion'. In: *GEOPHYSICS* 71.4 (2006), A35–A38. DOI: 10.1190/1.2213359.

1

[14] P. Haffinger, A. Gisolf and P. M. v. d. Berg. 'Towards high resolution quantitative subsurface models by full waveform inversion'. In: *Geophysical Journal International* 193.2 (Feb. 2013), pp. 788–797. ISSN: 0956-540X. DOI: 10.1093/gji/ggt021.

[15] B. Willemsen, A. Malcolm and W. Lewis. 'A numerically exact local solver applied to salt boundary inversion in seismic full-waveform inversion'. In: *Geophysical Journal International* 204.3 (Feb. 2016), pp. 1703–1720. DOI: 10.1093/gji/ggv547.

[16] S. Yuan, N. Fuji, S. Singh and D. Borisov. 'Localized time-lapse elastic waveform inversion using wavefield injection and extrapolation: 2-D parametric studies'. In: *Geophysical Journal International* 209.3 (Mar. 2017), pp. 1699–1717. DOI: 10.1093/gji/ggx118.

[17] Z. Zhao and M. K. Sen. 'Fast image-domain target-oriented least-squares reverse time migration'. In: *GEOPHYSICS* 83.6 (2018), A81–A86. DOI: 10.1190/geo2018-0033.1.

[18] Q. Guo and T. Alkhalifah. 'Target-oriented waveform redatuming and high-resolution inversion: Role of the overburden'. In: *GEOPHYSICS* 85.6 (2020), R525–R536. DOI: 10.1190/geo2019-0640.1.

[19] J. R. Berryhill. 'Wavěequation datuming before stack'. In: *GEOPHYSICS* 49.11 (1984), pp. 2064–2066. DOI: 10.1190/1.1441620.

[20] G. T. Schuster and M. Zhou. 'A theoretical overview of model-based and correlation-based redatuming methods'. In: *GEOPHYSICS* 71.4 (2006), SI103–SI110. DOI: 10.1190/1.2208967.

[21] N. Luiken and T. van Leeuwen. 'Seismic wavefield redatuming with regularized multi-dimensional deconvolution'. In: *Inverse Problems* 36.9 (Sept. 2020). DOI: 10.1088/1361-6420/aba9d1.

[22] D. F. Barrera, J. Schleicher and J. Brackenhoff. 'Interferometric redatuming by deconvolution and correlation-based focusing'. In: *GEOPHYSICS* 86.1 (2021), Q1–Q13. DOI: 10.1190/geo2019-0208.1.

[23] Q. Guo and T. Alkhalifah. 'Datum-based waveform inversion using a subsurface-scattering imaging condition'. In: *GEOPHYSICS* 84.4 (2019), S251–S266. DOI: 10.1190/geo2018-0615.1.

[24] M. Ravasi. 'Rayleigh-Marchenko redatuming for target-oriented, true-amplitude imaging'. In: *GEOPHYSICS* 82.6 (2017), S439–S452. DOI: 10.1190/geo2017-0262.1.

[25] D. Vargas, I. Vasconcelos, Y. Sripanich and M. Ravasi. 'Scattering-based focusing for imaging in highly complex media from band-limited, multicomponent data'. In: *GEOPHYSICS* 86.5 (2021), WC141–WC157. DOI: 10.1190/geo2020-0939.1.

[26] M. Dukalski and K. de Vos. 'Marchenko inversion in a strong scattering regime including surface-related multiples'. In: *Geophysical Journal International* 212.2 (Oct. 2017), pp. 760–776. DOI: 10.1093/gji/ggx434.

[27] K. Wapenaar, J. Thorbecke, J. van der Neut, F. Broggini, E. Slob and R. Snieder. 'Marchenko imaging'. In: *GEOPHYSICS* 79.3 (2014), WA39–WA57. DOI: 10.1190/geo2013-0302.1.

[28] L. Diekmann and I. Vasconcelos. 'Focusing and Green's function retrieval in three-dimensional inverse scattering revisited: A single-sided Marchenko integral for the full wave field'. In: *Phys. Rev. Research* 3 (1 2021), p. 013206. DOI: 10.1103/PhysRevResearch.3.013206.

[29] L. Diekmann, I. Vasconcelos and T. van Leeuwen. 'A note on Marchenko-linearised full waveform inversion for imaging'. In: *Geophysical Journal International* 234.1 (Feb. 2023), pp. 228–242. DOI: 10.1093/gji/ggad066.

[30] T. Cui, J. Rickett, I. Vasconcelos and B. Veitch. ' Target-oriented full-waveform inversion using Marchenko redatumed wavefields'. In: *Geophysical Journal International* 223.2 (July 2020), pp. 792–810. ISSN: 0956-540X. DOI: 10.1093/gji/ggaa333.

[31] M. Staring, R. Pereira, H. Douma, J. van der Neut and K. Wapenaar. 'Source-receiver Marchenko redatuming on field data using an adaptive double-focusing method'. In: *GEOPHYSICS* 83.6 (2018), S579–S590. DOI: 10.1190/geo2017-0796.1.

[32] A. Shoja, J. van der Neut and K. Wapenaar. 'Target-oriented least-squares reverse-time migration using Marchenko double-focusing: reducing the artefacts caused by overburden multiples'. In: *Geophysical Journal International* 233.1 (Apr. 2023), pp. 13–32. DOI: 10.1093/gji/ggac438.

[33] L. Diekmann, I. Vasconcelos, D. Cummings and A. Curtis. 'Towards exact linearized full-waveform inversion via Marchenko redatuming'. In: *First International Meeting for Applied Geoscience & Energy Expanded Abstracts*. 2021, pp. 3380–3384. DOI: 10.1190/segam2021-3583558.1.

[34] J. van der Neut, M. Ravasi, Y. Liu and I. Vasconcelos. 'Target-enclosed seismic imaging'. In: *GEOPHYSICS* 82.6 (2017), Q53–Q66. DOI: 10.1190/geo2017-0166.1.

[35] P. Zheglova, M. Ravasi, I. Vasconcelos and A. Malcolm. 'Target-enclosing inversion using an interferometric objective function'. In: *Geophysical Journal International* 232.1 (Aug. 2022), pp. 37–52. DOI: 10.1093/gji/ggac297.

2

TARGET-ORIENTED LEAST-SQUARES REVERSE-TIME MIGRATION USING MARCHENKO DOUBLE-FOCUSING: REDUCING THE ARTEFACTS CAUSED BY OVERBURDEN MULTIPLES

Geophysicists have widely used least-squares reverse-time migration (LSRTM) to obtain high-resolution images of the subsurface. However, LSRTM is computationally expensive and it can suffer from multiple reflections. Recently, a target-oriented approach to LSRTM has been proposed, which focuses the wavefield above the target of interest. Remarkably, this approach can be helpful for imaging below complex overburdens and subsalt domains. Moreover, this approach can significantly reduce the computational burden of the problem by limiting the computational domain to a smaller area. Nevertheless, target-oriented LSRTM still needs an accurate velocity model of the overburden to focus the wavefield accurately and predict internal multiple reflections correctly. A viable alternative to an accurate velocity model for internal multiple prediction is Marchenko redatuming. This method is a novel data-driven method that can predict Greens functions at any arbitrary depth, including all orders of multiples. The only requirement for this method is a smooth background velocity model of the overburden. Moreover, with Marchenko double-focusing, one can make virtual sources and receivers at a boundary above the target and bypass the overburden. This thesis chapter proposes a new algorithm for target-oriented LSRTM,

---

2

which fits the Marchenko double-focused data with predicted data. The predicted data of the proposed method is modelled by a virtual source term created by Marchenko double-focusing on a boundary above the target of interest. This virtual source term includes all the interactions between the target and the overburden. Moreover, the Marchenko double-focused data and the virtual source term are free of multiples generated in the overburden. Consequently, our target-oriented LSRTM algorithm suppresses the multiples purely generated inside the overburden. Our algorithm correctly accounts for all orders of multiples caused by the interactions between the target and the overburden, resulting in a significant reduction of the artefacts caused by the overburden internal multiple reflections and improves amplitude recovery in the target image compared to conventional LSRTM.

2.1. INTRODUCTION

In seismic exploration, geophysicists estimate the Earth's wave propagation parameters, such as the subsurface velocity and density. To evaluate these parameters, an array of sources and receivers is deployed at the surface of the Earth to generate and record seismic waves. A common approach to retrieve the subsurface parameters is to consider the model of the subsurface as a superposition of a background model (m_0), which corresponds to the long wavelengths, and a short-wavelength reflectivity model (δm). This scale separation is based on a weak-scattering assumption [2]. In seismic migration, we aim to obtain a structural image of δm.

Migration is an imaging process based on a linear relation between the recorded data and the reflectivity model (δm). One of the common migration techniques is called Reverse-Time Migration (RTM) [3–5]. In RTM, the underlying linear relation is the Born integral, so the RTM image is produced by applying the adjoint of the Born operator to the observed data. However, this approach may suffer from many errors such as noise [6], temporal band limitations, limited recording aperture [7], spatial aliasing, and multiple reflections [8].

One way to reduce some of these errors is to resolve δm by least-squares inversion. This approach, known as Least-Squares reverse-time migration (LSRTM), is the most common algorithm for producing a high-resolution reflectivity model of the subsurface. Nevertheless, LSRTM is computationally expensive [9] as it requires solving the wave equation and its adjoint for a large model in many iterations and storing large data volumes [7, 10, 11]. Reducing the computational burden of LSRTM is possible by reducing the computational domain. In other words, by limiting ourselves to a relatively small target region of interest. This so-called "target-oriented" approach [12–17] divides the medium into two parts: an overburden and a target. Target-oriented LSRTM (TOLSRTM) achieves this goal by bypassing the overburden and focusing the wavefield above the target of interest. This process, in which a wavefield is extrapolated from its current acquisition surface to another surface, is called redatuming [18–21].

Target-oriented LSRTM, in addition to its lower computational costs, can also be helpful in cases the overburden produces strong internal multiple reflections that mask the reflections of the target region. Nonetheless, for this method to work correctly, a model of the overburden, which can produce all orders of reflections, is needed. Researchers have shown a strong interest in solving the problems caused by inaccurate overburden models and the artifacts that internal multiple reflections can create in LSRTM images. For example, Guo and Alkhalifah [17, 22] introduced a least-squares waveform redatuming method to redatum the data to the boundary of the target and combined it with full waveform inversion.

Among different redatuming methods, Marchenko redatuming showed itself as a promising data-driven tool for predicting the Green's functions at the boundary of the target region with all orders of internal multiples [23–26]. The Marchenko

redatuming can predict the internal multiples by only having the direct arrival between the surface and the target boundary in a smooth background velocity model of the overburden. Once we solve the Marchenko equations, we get the response of the medium stimulated by virtual sources at the boundary of the target and recorded by receivers at the surface, including all orders of multiple reflections. Hence, the first step of Marchenko redatuming can be interpreted as source-side redatuming in the physical medium (including reflections in the overburden that are not encoded in the background model). Diekmann et al. [27] used Marchenko equations to predict the in-volume Green's function of a target of interest and used this wavefield as the incident wavefield inside the scattering integral. Cui et al. [28] used the reciprocity theorem to derive a forward modeling equation based on Marchenko wavefields for Full waveform inversion. Moreover, one of the byproducts of the Marchenko integrals is the downgoing part of the focusing function, which is the inverse of the transmission response of the overburden. This focusing function can also be applied at the receiver side to achieve double-sided (meaning source and receiver) redatuming [29]. The process of double-sided redatuming with the help of the Marchenko focusing function is called Marchenko double-focusing.

In this chapter, we consider the upgoing Marchenko double-focused data as the "observed data" that we feed to an LSRTM algorithm. To complete our TOLSRTM algorithm, we formulate a forward modeling to match the Marchenko double-focused data with the predicted data of the target region. This forward modeling is based on the downgoing wavefields from the Marchenko equation and a Born model of the target. This Marchenko downgoing wavefield acts as virtual source for the modeling and the inversion.

The organization of this chapter is as follows: First, we briefly review least-squares reverse-time migration and target-oriented LSRTM. Second, Marchenko redatuming and double-focusing are explained. Then, our method of combining target-oriented LSRTM and Marchenko double-focusing is introduced. In the results section, we show numerical examples of our method, and we exhibit the consequences of using an inaccurate velocity model for redatuming and TOLSRTM. Finally, results and potential future directions are discussed.

2.2. THEORY

2.2.1. LEAST-SQUARES REVERSE-TIME MIGRATION

We start to formulate our target-oriented algorithm by briefly reviewing classical reverse-time migration with sources and receivers at the acquisition surface. Classical RTM is based on the Born approximation where the incident wavefield (P^{inc}) is approximated by the background Green's function

$$P^{inc}(\mathbf{x}, \mathbf{x}_s, \omega) \approx G_0(\mathbf{x}, \mathbf{x}_s, \omega) W(\omega). \tag{2.1}$$

Here $W(\omega)$ is the wavelet signature, and ω is the angular frequency. Moreover, $\mathbf{x} = (x_1, x_2, x_3)$ is a location inside the medium, $\mathbf{x}_s$ is the source location, and $G_0(\mathbf{x}, \mathbf{x}_s, \omega)$ is the Fourier transform of the causal solution of the scalar wave equation in the background velocity model, which in the frequency domain and with a constant density (ρ_0) is equal to the Helmholtz equation:

$$\nabla^2 G_0 + k_0^2 G_0 = -i\omega\rho_0\delta(\mathbf{x} - \mathbf{x}_s), \tag{2.2}$$

where $k_0(\mathbf{x}) = \frac{\omega}{c_0(\mathbf{x})}$ is the wavenumber, c_0 is background velocity, and i is the imaginary unit.

The reflectivity model is defined as $\delta m = (\frac{1}{c^2} - \frac{1}{c_0^2})$, where c is the perturbed velocity. Here, δm is connected to the scattered data (P^{scat}) through the following linear equation [30]:

$$P_{pred}^{scat}(\mathbf{x}_r, \mathbf{x}_s, \delta m, \omega) = \frac{\omega^2}{\rho_0} \int_V G_0(\mathbf{x}_r, \mathbf{x}, \omega)\delta m(\mathbf{x}) G_0(\mathbf{x}, \mathbf{x}_s, \omega) W(\omega)\, d\mathbf{x}. \tag{2.3}$$

This integral is taken over the volume of the model (V). Subscripts "r" and "s" are used to specify receiver and source, respectively. Equation 2.3 can be written in the operator form as:

$$P_{pred}^{scat}(\mathbf{x}_r, \mathbf{x}_s, \delta m, \omega) = \mathscr{L}\delta m. \tag{2.4}$$

Here $\mathscr{L}$ is the forward Born operator.

In the standard reverse-time migration method, the reflectivity model is approximately retrieved by applying the adjoint of $\mathscr{L}$ to the observed scattered data:

$$\delta m^{mig}(\mathbf{x}) = \mathscr{L}^\dagger P_{obs}^{scat}. \tag{2.5}$$

Green's functions (G_0) which constitute the kernel $\mathscr{L}$, only consider wave propagation in the smooth background and do not contain reflections from the perturbations. As a result, this kernel is unable to interpret the multiple-scattered waves correctly. Moreover, since the adjoint of this kernel is only an approximation of its inverse, the resolution of the retrieved reflectivity model is low.

To overcome the resolution issue, researchers have utilized a least-squares approach by replacing the adjoint ($\mathscr{L}^\dagger$) with a damped least-squares solution [6, 31]:

$$\delta m^{mig} = [\mathscr{L}^\dagger\mathscr{L} + \epsilon]^{-1}\mathscr{L}^\dagger P_{obs}^{scat}. \tag{2.6}$$

However, computing the Hessian matrix ($\mathscr{L}^\dagger\mathscr{L}$) and its inverse is prohibitive. Alternatively, updating the reflectivity model is preferred by an iterative algorithm that minimizes the L2-norm of the difference between observed and predicted data

$$C(\delta m) = \frac{1}{2}\left\| P_{pred}^{scat}(\delta m) - P_{obs}^{scat} \right\|_2^2. \tag{2.7}$$

We can solve this optimization problem for instance by a conjugate gradient algorithm. Since in least-squares reverse-time migration, the background velocity model (c_0) is kept unchanged, and only the reflectivity model (δm) is updated, the Green's functions of Equation 2.3 are only computed once. For an overview of least-squares reverse-time migration, we refer to Schuster [2].

2.2.2. Target-oriented least-squares reverse-time migration

Researchers have proposed to implement the imaging and inversion in a target-oriented manner [12–17]. In this way, the wavefield can be focused below a complex overburden to produce virtual sources and receivers right above the target [18–21]. These redatumed wavefields can be used for imaging and inversion. The advantages of this approach are as follows: 1) The wavefield is focused below specific structures, such as salt domes, and 2) the computational costs are lower because the computational domain can be reduced significantly. However, current methods need a reasonable estimation of the velocity model of the overburden (i.e., the part of the model above the target of interest), which can predict internal multiple reflections. Otherwise, these overburden-generated multiple reflections produce artifacts inside the retrieved image of the target.

Marchenko redatuming enables us to take these overburden-generated multiples into account and improve the quality of the target-oriented LSRTM images. The following section gives a brief review of Marchenko redatuming by double-focusing.

2.2.3. Marchenko redatuming by double-focusing

Marchenko redatuming is a novel data-driven method that can retrieve the Green's function at a surface above the target area with all orders of its multiple-scattered events. The only requirements for this method are the reflection response at the surface and a smooth background velocity model of the overburden that can predict the direct arrival from the surface to the redatuming level.

In order to retrieve Green's functions at the redatuming level, the coupled Marchenko-type representations are solved iteratively. These equations are [26]

$$
\begin{aligned}
G_{Mar}^{-}(\mathbf{x}_v, \mathbf{x}_r, \omega) = \int_{\mathscr{D}_{acq}} R(\mathbf{x}_r, \mathbf{x}_s, \omega) f_1^{+}(\mathbf{x}_s, \mathbf{x}_v, \omega)\, d\mathbf{x}_s \\
- f_1^{-}(\mathbf{x}_r, \mathbf{x}_v, \omega),
\end{aligned}
\tag{2.8}
$$

and

$$
\begin{aligned}
G_{Mar}^{+}(\mathbf{x}_v, \mathbf{x}_r, \omega) = -\int_{\mathscr{D}_{acq}} R(\mathbf{x}_r, \mathbf{x}_s, \omega) f_1^{-}(\mathbf{x}_s, \mathbf{x}_v, \omega)^{*}\, d\mathbf{x}_s \\
+ f_1^{+}(\mathbf{x}_r, \mathbf{x}_v, \omega)^{*}.
\end{aligned}
\tag{2.9}
$$

In these equations $\mathcal{D}_{acq}$ is the acquisition surface where $\mathbf{x}_s$ and $\mathbf{x}_r$ are located, G_{Mar}^- and G_{Mar}^+ are up-going and down-going parts of the Marchenko redatumed Green's function (Fig. 2.1a and 2.1b), respectively. Further, f_1^- is the up-going part, and f_1^+ is the down-going part of the focusing function, and the subscript "v" stands for a virtual point, which is located on the redatuming level. We denote this redatuming level by $\mathcal{D}_{tar}$. Moreover, $R(\mathbf{x}_r, \mathbf{x}_s, \omega)$ is the dipole response of the medium at the acquisition surface. R is related to the upgoing Green's function (G^-) with the following relation:

$$R(\mathbf{x}_r, \mathbf{x}_s, \omega) = \frac{\partial_{3,s} G^-(\mathbf{x}_r, \mathbf{x}_s, \omega)}{\frac{1}{2} i \omega \rho(\mathbf{x}_s)}, \tag{2.10}$$

where $\partial_{3,s}$ is the partial derivative in the downward direction taken at $\mathbf{x}_s$. Note that before inserting $R(\mathbf{x}_r, \mathbf{x}_s, \omega)$ into Equations 2.8 and 2.9, we need to remove horizontally propagating waves and surface-related multiples. For more information on the derivation of these integrals and their solution for computing the focusing functions and Green's functions, please refer to Wapenaar et al. [26] and Thorbecke et al. [32].

The above-mentioned equations can be interpreted as source-side redatuming, as the receivers are still located at the acquisition surface. To relocate receivers to the target level, Staring et al. [29] suggested convolving the up-going and down-going parts of the Marchenko redatumed Green's function with the (filtered) downgoing focusing function in a multi-dimensional sense:

$$G_{df}^{-,+}(\mathbf{x}_v, \mathbf{x}_v', \omega) = \int_{\mathcal{D}_{acq}} G_{Mar}^-(\mathbf{x}_v, \mathbf{x}_r, \omega) \mathscr{F}_1^+(\mathbf{x}_r, \mathbf{x}_v', \omega) \, d\mathbf{x}_r, \tag{2.11}$$

and

$$G_{df}^{+,+}(\mathbf{x}_v, \mathbf{x}_v', \omega) = \int_{\mathcal{D}_{acq}} G_{Mar}^+(\mathbf{x}_v, \mathbf{x}_r, \omega) \mathscr{F}_1^+(\mathbf{x}_r, \mathbf{x}_v', \omega) \, d\mathbf{x}_r, \tag{2.12}$$

where

$$\mathscr{F}_1^+(\mathbf{x}_r, \mathbf{x}_v', \omega) = \frac{\partial_{3,r} f_1^+(\mathbf{x}_r, \mathbf{x}_v', \omega)}{\frac{1}{2} i \omega \rho(\mathbf{x}_r)}. \tag{2.13}$$

Here the vertical derivative is taken with respect to $\mathbf{x}_r$. In Equations 2.11 and 2.12, the first superscript on the left-hand side expresses the direction of the propagation at the receiver location, the second one shows the same at the source location, and "df" means "double-focused." The above-mentioned procedure is called "Marchenko double-focusing."

Through Marchenko double-focusing, we retrieve a down-going Green's function ($G_{df}^{+,+}$) which contains a band-limited delta function and interactions between target and overburden, and an up-going Green's function ($G_{df}^{-,+}$), which is the up-going response to $G_{df}^{+,+}$ from the target at the redatuming level, still including interactions between target and overburden on the source side (Fig. 2.1c and 2.1d). In comparison, "conventional double-focusing" is the act of using the inverse of

the direct arrival of the transmission response of the overburden instead of the downgoing Marchenko focusing function for double-focusing. Considering that the inverse of the direct arrival of the transmission response of the overburden does not contain multiple reflections, it is unable to predict and remove the multiples generated by the overburden. In the next section, "double-focusing" is a general term referring to both methods, and it is mentioned wherever a distinction is necessary.

(a)   (b)

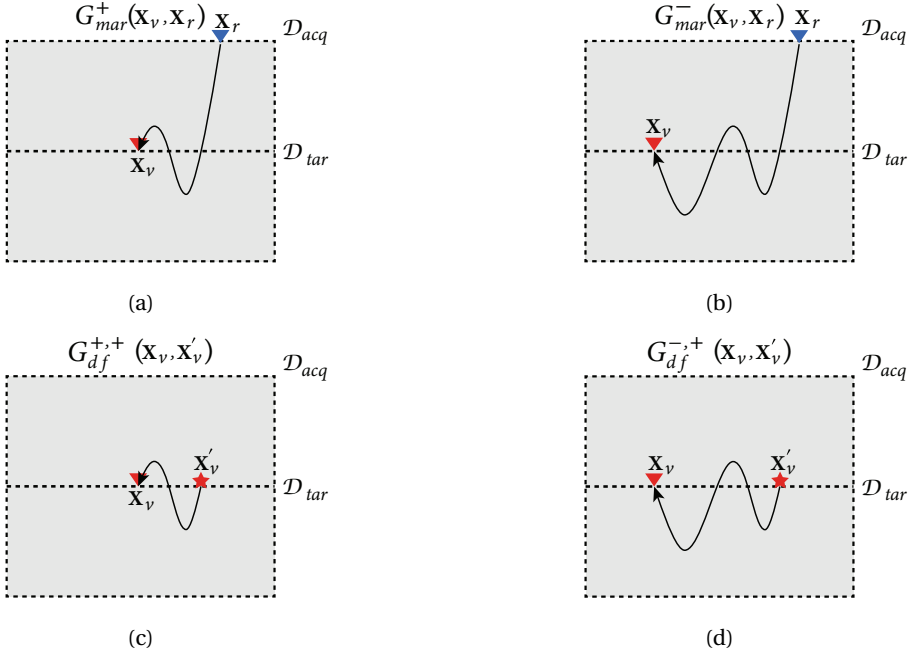(c)   (d)

Figure 2.1.: The Green's functions resulting from Marchenko redatuming and double-focusing.   a) Downgoing part of the Marchenko Green's function, b) upgoing part of the Marchenko Green's function, c) downgoing Marchenko double-focused Green's function and d) upgoing Marchenko double-focused Green's function

2.2.4. TARGET-ORIENTED LSRTM BY MARCHENKO DOUBLE-FOCUSING

In this section, I will combine the Marchenko double-focusing scheme with LSRTM to derive a new forward modeling operator and cost function for the target-oriented approach. This new forward modeling operator and cost function are the target-oriented counterparts of Equation 2.3 and Equation 2.7, respectively.

The up-going Green's function is related to the down-going Green's function at the redatuming level with this equation [33]:

$$G^{-,+}(\mathbf{x}_{vr}, \mathbf{x}'_{vs}, \omega) = \int_{\mathscr{D}_{tar}} R^{tar}(\mathbf{x}_{vr}, \mathbf{x}_{vs}, \omega) G^{+,+}(\mathbf{x}_{vs}, \mathbf{x}'_{vs}, \omega) \, d\mathbf{x}_{vs}. \tag{2.14}$$

Here $\mathbf{x}_{vs}$ and $\mathbf{x}_{vr}$ are located at $\mathscr{D}_{tar}$, and "vr" and "vs" stand for virtual receiver/source. In addition, $R^{tar}(\mathbf{x}_{vr}, \mathbf{x}_{vs}, \omega)$ is the dipole reflection response of the target at the redatuming level with a reflection-free half-space as the overburden. Substitution of the double-focused Green's functions into Equation 2.14 lays the foundation of our target-oriented scheme. However, double-focused data suffers from limited aperture, meaning we can not retrieve the far-offset section of the data at the depth (R^{tar}) simply because the large propagation angles do not reach the surface within the limits of the acquisition aperture.

To address this issue, consider we would put actual sources and receivers at the target boundary. The Green's functions of this configuration are related to the double-focused Green's functions via

$$G_{df}^{-,+}(\mathbf{x}'_{vr}, \mathbf{x}_{vs}, \omega) \approx \int_{\mathscr{D}_{tar}} \Gamma(\mathbf{x}'_{vr}, \mathbf{x}_{vr}, \omega) G^{-,+}(\mathbf{x}_{vr}, \mathbf{x}_{vs}, \omega) \, d\mathbf{x}_{vr}. \tag{2.15}$$

Here

$$\Gamma(\mathbf{x}'_{vr}, \mathbf{x}_{vr}, \omega) = \int_{\mathscr{D}_{acq}} G_d^+(\mathbf{x}'_{vr}, \mathbf{x}_s, \omega)^{-1} G_d^+(\mathbf{x}_{vr}, \mathbf{x}_s, \omega) \, d\mathbf{x}_s \tag{2.16}$$

is a point-spread function (PSF) with characteristics of a band-limited delta function that imposes temporal and spatial band limitations to the upgoing Green's function. In this equation, G_d^+ is the first arrival of the Green's function between the target boundary and the surface. $\Gamma(\mathbf{x}'_{vr}, \mathbf{x}_{vr}, \omega)$ is a filter that removes high propagation angles from the data. In other words, Gamma takes the full band reflection response of the target (R^{tar}) once to the surface by applying G_d^+ to it, and then takes it back to the focusing level by applying the inverse of the G_d^+ to the result of the previous step. In this way, R^{tar} goes under the same process as the other double-focused wavefields.

To make Equation 2.14 compatible with the double-focused Green's functions, we assume

$$G_{df}^{+,+}(\mathbf{x}_{vs}, \mathbf{x}'_{vs}, \omega) \approx G^{+,+}(\mathbf{x}_{vs}, \mathbf{x}'_{vs}, \omega), \tag{2.17}$$

and then we convolve both sides of it with the PSF in Equation 4.15 and use Equation 2.15 to reach

$$\begin{aligned} G_{df}^{-,+}(\mathbf{x}'_{vr}, \mathbf{x}'_{vs}, \omega) = \\ \int_{\mathscr{D}_{tar}} \int_{\mathscr{D}_{tar}} \Gamma(\mathbf{x}'_{vr}, \mathbf{x}_{vr}, \omega) R^{tar}(\mathbf{x}_{vr}, \mathbf{x}_{vs}, \omega) G_{df}^{+,+}(\mathbf{x}_{vs}, \mathbf{x}'_{vs}, \omega) \, d\mathbf{x}_{vr} \, d\mathbf{x}_{vs}. \end{aligned} \tag{2.18}$$

In other words, $G_{df}^{-,+}$ is related to the $G_{df}^{+,+}$ with a temporal and spatial band-limited version of $R^{tar}(\mathbf{x}_{vr}, \mathbf{x}_{vs}, \omega)$, which we can write as:

$$\hat{R}^{tar}(\mathbf{x}'_{vr}, \mathbf{x}_{vs}, \omega) = \int_{\mathscr{D}_{tar}} \Gamma(\mathbf{x}'_{vr}, \mathbf{x}_{vr}, \omega) R^{tar}(\mathbf{x}_{vr}, \mathbf{x}_{vs}, \omega) \, d\mathbf{x}_{vr}, \tag{2.19}$$

and subsequently rewrite equation 2.18 as:

$$G_{df}^{-,+}(\mathbf{x}'_{vr}, \mathbf{x}'_{vs}, \omega) = \int_{\mathscr{D}_{tar}} \hat{R}^{tar}(\mathbf{x}'_{vr}, \mathbf{x}_{vs}, \omega) G_{df}^{+,+}(\mathbf{x}_{vs}, \mathbf{x}'_{vs}, \omega) \, d\mathbf{x}_{vs}. \tag{2.20}$$

By taking $\hat{R}^{tar}$ as a function of δm of the target, this equation will become the forward modeling equation for our target-oriented least-squares reverse-time migration. We take the observed scattered wavefield as

$$\hat{P}_{obs}^{scat} = G_{df}^{-,+}(\mathbf{x}_{vr}', \mathbf{x}_{vs}', \omega) W(\omega), \tag{2.21}$$

and the predicted scattered wavefield as

$$\hat{P}_{pred}^{scat}(\mathbf{x}_{vr}', \mathbf{x}_{vs}', \delta m, \omega) = \\ \int_{\mathscr{D}_{tar}} \hat{R}_{pred}^{tar}(\mathbf{x}_{vr}', \mathbf{x}_{vs}, \delta m, \omega) G_{df}^{+,+}(\mathbf{x}_{vs}, \mathbf{x}_{vs}', \omega) W(\omega) \, d\mathbf{x}_{vs}. \tag{2.22}$$

Additionally, it is possible to take the $G_{df}^{+,+}$ as a function of δm and solve a non-linear problem for applications where the target is subject to changes [34, 35].

To demonstrate the relation between Equation 2.22 and Equation 2.3, first, consider Equation 2.19 and insert it into Equation 2.22

$$\hat{P}_{pred}^{scat}(\mathbf{x}_{vr}', \mathbf{x}_{vs}', \delta m, \omega) = \\ \int_{\mathscr{D}_{tar}} \int_{\mathscr{D}_{tar}} \Gamma(\mathbf{x}_{vr}', \mathbf{x}_{vr}, \omega) R_{pred}^{tar}(\mathbf{x}_{vr}, \mathbf{x}_{vs}, \delta m, \omega) G_{df}^{+,+}(\mathbf{x}_{vs}, \mathbf{x}_{vs}', \omega) W(\omega) \, d\mathbf{x}_{vs} \, d\mathbf{x}_{vr}. \tag{2.23}$$

Next, consider

$$R_{pred}^{tar}(\mathbf{x}_{vr}, \mathbf{x}_{vs}, \delta m, \omega) = \frac{\omega^2}{\rho_0} \int_V G_0(\mathbf{x}_{vr}, \mathbf{x}, \omega) \delta m(\mathbf{x}) \frac{\partial_{3,vs} G_0(\mathbf{x}, \mathbf{x}_{vs}, \omega)}{\frac{1}{2} i \omega \rho_0} \, d\mathbf{x}, \tag{2.24}$$

where we used Equation 2.10 to rewrite Equation 2.3 for reflection response (dipole response) instead of scattered pressure wavefield (monopole response). Then, we insert Equation 2.24 into Equation 2.23, and then we rearrange the integrals to reach

$$\hat{P}_{pred}^{scat}(\mathbf{x}_{vr}', \mathbf{x}_{vs}', \delta m, \omega) = \\ \frac{\omega^2}{\rho_0} \int_v \left[\int_{\mathscr{D}_{tar}} \Gamma(\mathbf{x}_{vr}', \mathbf{x}_{vr}, \omega) G_0(\mathbf{x}_{vr}, \mathbf{x}, \omega) \, d\mathbf{x}_{vr} \right] \\ \times \delta m(\mathbf{x}) \left[\int_{\mathscr{D}_{tar}} \frac{\partial_{3,vs} G_0(\mathbf{x}, \mathbf{x}_{vs}, \omega)}{\frac{1}{2} i \omega \rho(\mathbf{x}_{vs})} G_{df}^{+,+}(\mathbf{x}_{vs}, \mathbf{x}_{vs}', \omega) W(\omega) \, d\mathbf{x}_{vs} \right] \, d\mathbf{x}. \tag{2.25}$$

We redefine the term in the first square bracket as

$$\hat{G}_0(\mathbf{x}_{vr}', \mathbf{x}, \omega) = \int_{\mathscr{D}_{tar}} \Gamma(\mathbf{x}_{vr}', \mathbf{x}_{vr}, \omega) G_0(\mathbf{x}_{vr}, \mathbf{x}, \omega) \, d\mathbf{x}_{vr}, \tag{2.26}$$

which is the spatial and temporal band limited Green's function of the target area, and the term in the second square bracket as

$$P_{df}^{inc}(\mathbf{x}, \mathbf{x}_{vs}', \omega) = \\ \int_{\mathscr{D}_{tar}} \frac{\partial_{3,vs} G_0(\mathbf{x}, \mathbf{x}_{vs}, \omega)}{\frac{1}{2} i \omega \rho(\mathbf{x}_{vs})} G_{df}^{+,+}(\mathbf{x}_{vs}, \mathbf{x}_{vs}', \omega) W(\omega) \, d\mathbf{x}_{vs}, \tag{2.27}$$

which is the incident wavefield computed by a Marchenko double-focused downgoing wavefield, so that it includes the interactions between the target and the overburden. Then we reach the following equation, which has a similar structure as Equation 2.3:

$$\hat{P}^{scat}_{pred}(\mathbf{x}'_{vr}, \mathbf{x}'_{vs}, \delta m, \omega) = \frac{\omega^2}{\rho_0} \int_v \hat{G}_0(\mathbf{x}'_{vr}, \mathbf{x}, \omega) \delta m(\mathbf{x}) P^{inc}_{df}(\mathbf{x}, \mathbf{x}'_{vs}, \omega) d\mathbf{x}, \tag{2.28}$$

where v is the target volume. Finally, the new cost function is

$$C(\delta m) = \frac{1}{2} \left\| \hat{P}^{scat}_{pred}(\delta m) - \hat{P}^{scat}_{obs} \right\|^2_2, \tag{2.29}$$

which we solve with a conjugate gradient algorithm.

It is possible to compute Equations 2.27 and 2.28 in two ways. The first way is to compute the background Green's function (G_0) with an algorithm of choice, e.g. finite-difference, and then insert it in Equations 2.27 and 2.28. The second way is to inject $G^{+,+}_{df}$ as a downward radiating dipole line source for each $\mathbf{x}'_{vs}$ location in the target background medium with a numerical PDE solver to compute P^{inc}_{df}. Then inject $\frac{\omega^2}{\rho_0} \delta m(\mathbf{x}) P^{inc}_{df}$ as a contrast source to compute $\hat{P}^{scat}_{pred}$. The decision of choosing the appropriate computation method is based on the dimensions of the target and the number of virtual sources.

2.3. NUMERICAL RESULTS

2.3.1. MARCHENKO DOUBLE-FOCUSING VS. CONVENTIONAL DOUBLE-FOCUSING

To validate our theory, we use two different synthetic models. We compute the reflection data sets at the acquisition surface using a finite-difference algorithm [36] and a dipole (vertical force) source with a flat spectrum wavelet (0 to 100 Hz). The injection rate is represented as an $i\omega$ factor in Equation 2.2. Further, we use a spatial sampling of 2.5 m in both directions and a time sampling of 0.4 ms. To reduce the data size, we set the receiver temporal sampling to 4 ms. For the sake of better visualization, we convolve all time-space records with a 30 Hz Ricker wavelet.

For computational simplicity, we define the target area of both models as a homogeneous background and constant density with an embedded velocity perturbation (fig. 2.2). Consequently, we use the analytical solution of the Helmholtz equation for a homogeneous 2D medium to compute the Green's functions for TOLSRTM [37, 38]:

$$G_0(\mathbf{x}, \mathbf{x}_s, \omega) = \frac{1}{2\pi} K_0 \left(\frac{-i\omega}{c_0} |\mathbf{x} - \mathbf{x}_s| \right). \tag{2.30}$$

Here K_0 is the modified Bessel function of the second kind and zeroth order. In the TOLSRTM algorithm, the spatial sampling is set to 5 m and the time sampling is 4 ms.

Note that we do not commit an inverse crime in these examples. As we mentioned earlier, to compute $\hat{P}_{obs}^{scat}$, we compute the reflection response at the acquisition surface by a finite-difference algorithm. Then we apply Marchenko double-focusing to this data set. On the other hand, to compute $\hat{P}_{pred}^{scat}$ we use Equations 2.30, 2.28, and 2.27. In all of the mentioned steps, we deal with convolutions that lead to a loss of resolution. To avoid it, we compute everything with a flat spectrum wavelet (0 to 100 Hz), and then we convolve both $\hat{P}_{obs}^{scat}$ and $\hat{P}_{pred}^{scat}$ with a 30 Hz Ricker wavelet.

For comparison, we compute the redatuming operator in two different ways for both models. First, we isolate the direct arrival of the transmission response of the overburden with a time window and use it as an estimation of the redatuming operator and redatum the surface data with it. This approach is equivalent to conventional redatuming of primary reflections [18]. Second, we solve the coupled Marchenko equations with the help of this direct arrival to compute the redatumed Green's and focusing functions [32]. We calculate the direct arrival in this way to avoid kinematic errors. We discuss the issue of kinematic errors later in section 2.3.3.

SIMPLE MODEL

As a first example, we define a model with a single-layered overburden and a single small diffractor with dimensions of 5 meters by 5 meters inside a homogeneous background as the target (Fig. 2.2). The background velocity is set to 1500 m/s, and the velocity of the overburden layer is 3000 m/s. The density is constant and equal to 2500 kg/m^3 everywhere. For this model, 101 sources and receivers with a spacing of 10 meters are used. The number and spacing of real and virtual sources and receivers are the same. In Figure 2.2 blue crosses are the actual source and receiver locations, and the red dots are the virtual source and receivers locations. Moreover, the overburden is designed such that a higher-order multiple reflection coincides with the primary event of the diffractor. We design it in this way to show that our method can handle the overburden-related multiple reflections correctly.
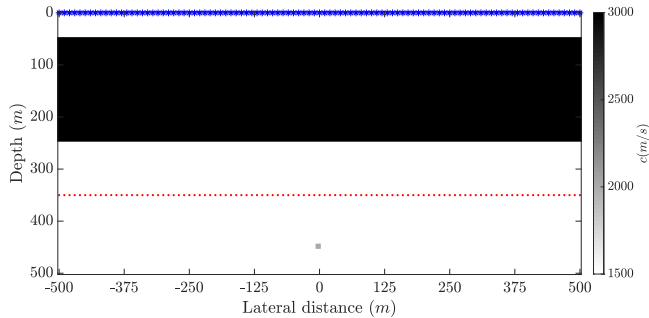

Figure 2.2.: Velocity model with a single-layered overburden and a small diffractor in the target.

In Figure 2.3, the common-source record at the acquisition surface is shown for this model. The diffractor response of the simple model is visible around 0.5 seconds in this figure and it partly coincides with a higher-order multiple reflection.
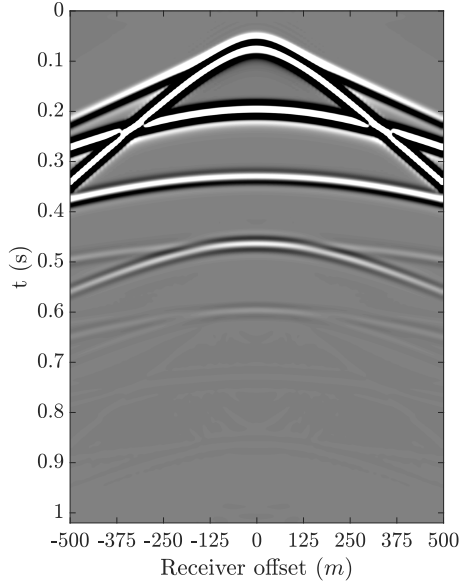
2

Figure 2.3.: Common-source record at the surface of a source located at lateral distance = 0 in the simple model. A linear time-varying ($\frac{t}{dt}$) gain is applied to this record to amplify weaker events.

In Figure 2.4, we show the double-focused data of this model. From here onward, we use the subscript 'Cdf' for the data produced by 'conventional double-focusing', and 'Mdf' for 'Marchenko double-focused' data. In Figure 2.4b, it is visible that the overburden-related multiple reflections have been suppressed by applying Marchenko double-focusing, yet the interactions between the overburden and the target are still present. Moreover, in Figure 2.5, we show the double-focused down-going Green's function (Eq. 2.12). The downgoing wavefield of the Marchenko double-focusing (Fig. 2.5b) contains the higher-order interactions between the target and the overburden, whereas the downgoing wavefield of the conventional double-focusing does not include these interactions. Injecting the downgoing Marchenko double-focused wavefield into the target from the focusing depth reproduces these high-order interactions in the predicted data of the TOLSRTM algorithm.

In Figure 2.6 the predicted data of both approaches after 20 iterations are shown. The predicted data of the conventional double-focusing is not a good fit for the conventional double-focused data. In contrast, the predicted data of the Marchenko double-focusing approach is a better fit for Marchenko double-focused data. In

2

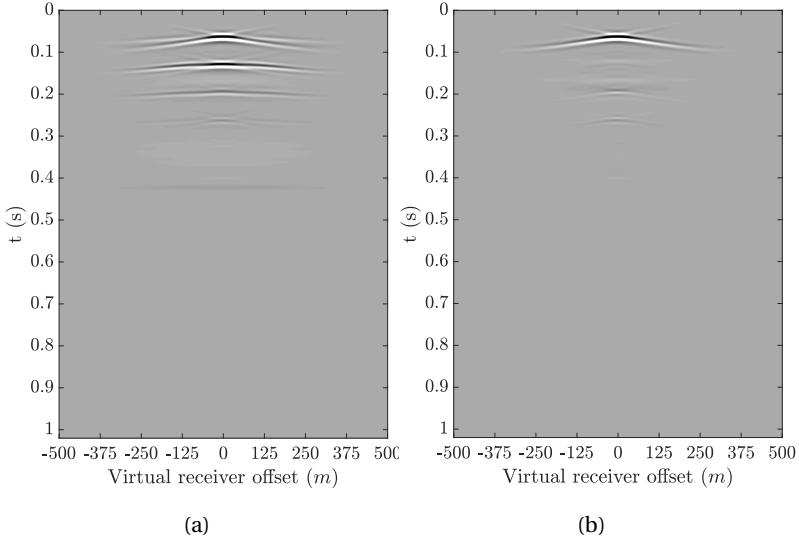(a)   (b)

Figure 2.4.: Double-focused (upgoing) data of model with a single-layered overburden corresponding to a virtual source at the middle. a) Conventional double-focused data ($G_{Cdf}^{-,+}$) by applying conventional redatuming operators, and b) Marchenko double-focused data ($G_{Mdf}^{-,+}$). The maximum and the minimum value of the grey-level scale of both figures are the same and a linear time-varying ($\frac{t}{dt}$) gain is applied to both records to amplify weaker events.

Figure 2.6b, the weak multiple reflections generated by interactions between target and overburden can be seen inside the red box. This confirms that our method is not only able to suppress multiple reflections generated inside the overburden significantly but also able to predict the interactions between the target and the overburden.

Figures 2.7 and 2.8 show the imaging result of these two approaches for the first iteration and after 20 iterations for the model with single-layered overburden. Note the horizontal event in Figure 2.7, coming from the overburden multiple, which overlaps the image of the target. In Figure 2.8, this horizontal event is strongly suppressed. To demonstrate the resolution improvement of our method, we compare the horizontal and vertical sections of the image of different approaches in Figures 2.9a and 2.9b. As these figures are showing, our approach has a superior resolution. A comparison of the convergence rate of the cost functions of these approaches is also shown in Figure 2.10.
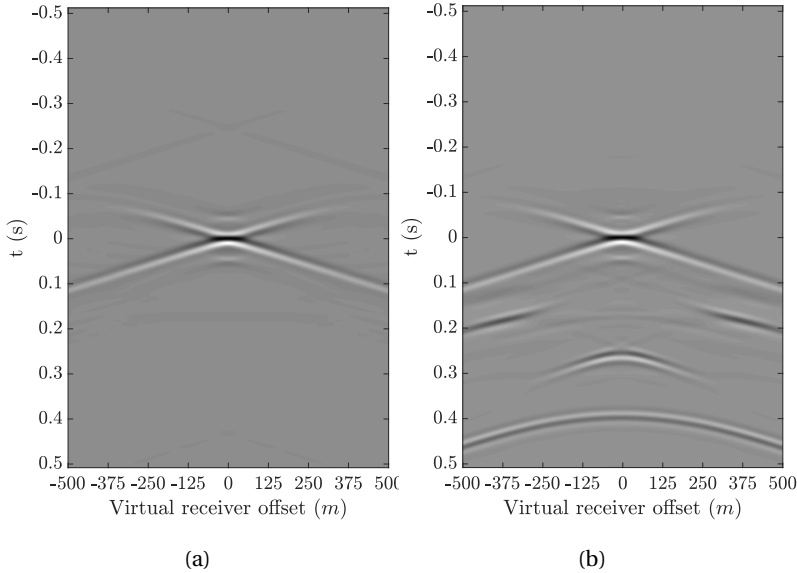
Figure 2.5.: Virtual source wavefield of the model with a single-layered overburden at the middle virtual source location. a) The conventional double-focused source ($G^{+,+}_{Cdf}$) by applying conventional redatuming operators, and b) Marchenko double-focused source ($G^{+,+}_{Mdf}$). The maximum and the minimum value of the grey-level scale of both figures are the same and a linear time-varying ($\frac{t}{dt}$) gain is applied to both records to amplify weaker events.

SYNCLINE MODEL

As a second example, we design a model with more layers and a syncline-shaped layer in its overburden (Fig. 2.11a) and a line reflector with a width of 5 meters in the target region. In this model, the background velocity of the target area is 2400 m/s, and the velocity of the reflector is 2700 m/s. Moreover, density variations are introduced in the overburden (Fig. 2.11b) to generate substantial internal multiples, but the density of the target region is constant and equal to 1000 kg/m^3. For this model, 301 sources and receivers with the same spacing as in the first model are deployed. The number and spacing of real and virtual sources and receivers are the same. In Figures 2.11a, and 2.11b blue crosses are the actual source and receiver locations, and the red dots are the virtual source and receivers locations.

Figure 2.12 shows the middle common-source record at the acquisition surface for the model with the syncline overburden. In Figure 2.13, we show the conventional double-focused data (Fig. 2.13a), the predicted data in case of conventional double-focusing (Fig. 2.13c), the Marchenko double-focused data (Fig. 2.13b) and the predicted data in case of Marchenko double-focusing (Fig. 2.13d) for the model with
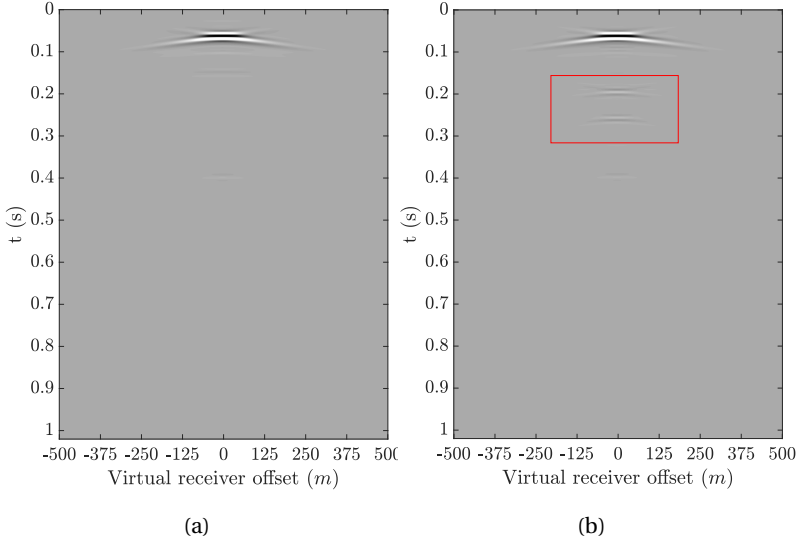
Figure 2.6.: Predicted data with a virtual source located at the middle of the model with a single-layered overburden after 20 iterations. a) Conventional double-focusing, and b) Marchenko double-focusing. Weak multiple reflections that are predicted by our method can be seen inside the red box. The maximum and the minimum value of the grey-level scale of both figures are the same and a linear time-varying ($\frac{t}{dt}$) gain is applied to both records to amplify weaker events.

the syncline overburden. In Figure 2.13b, it can be seen, compared to conventional double-focused data (Fig. 2.13a), that the multiples purely generated in overburden are suppressed by applying Marchenko double-focusing. In addition, by comparing Figure 2.13c and Figure 2.13d we see that the predicted data of Marchenko double-focusing not only predicts the primary reflection, but also predicts the multiples that are generated by interactions between the target and the overburden. Moreover, in Figure 2.14, we show the double-focused down-going Green's function (Eq. 2.12). We see that the virtual source wavefield for the conventional double-focused predicted data contains only a bandlimited delta function, whereas the virtual source wavefield for the Marchenko double-focused predicted data contains additional events to predict the target and overburden interactions in the Marchenko double-focused data in Figure 2.13b.

Consequently, the conventional double-focusing approach is unable to fit the predicted data, whereas the Marchenko double-focusing approach can produce predicted data with an acceptable fit to the Marchenko double-focused data. Note that the predicted data of our proposed method can predict the interactions between the target and the overburden, without the knowledge of the overburden reflectivity model, by taking $G_{Mdf}^{+,+}$ as the virtual source wavefield. This source contains these
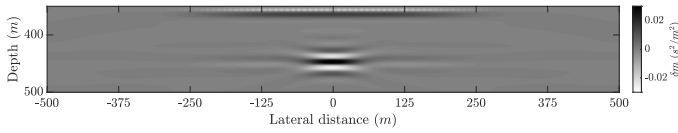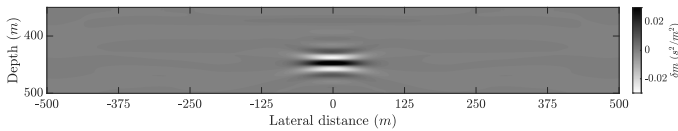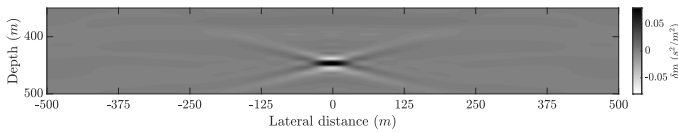
(a) RTM
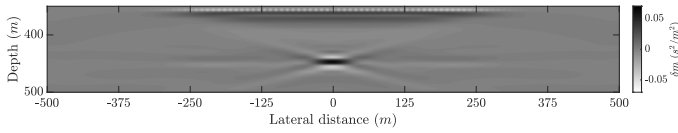
(b) LSRTM

Figure 2.7.: Retrieved target image of the model with a single-layered overburden by conventional double-focusing operators. a) RTM, and b) LSRTM after 20 iterations.

(a) RTM

(b) LSRTM

Figure 2.8.: Retrieved target image of the model with a single-layered overburden by Marchenko double-focusing. a) RTM, and b) LSRTM after 20 iterations.

interactions, as can be seen in Figure 2.14b.

Figures 2.15 and 2.16 show the imaging result of these two approaches for the first iteration and after 20 iterations for the model with the syncline overburden. To demonstrate the improvement of vertical resolution and lateral continuity, we compare the horizontal and vertical sections of the image of different approaches in

(a) Horizontal cross-section
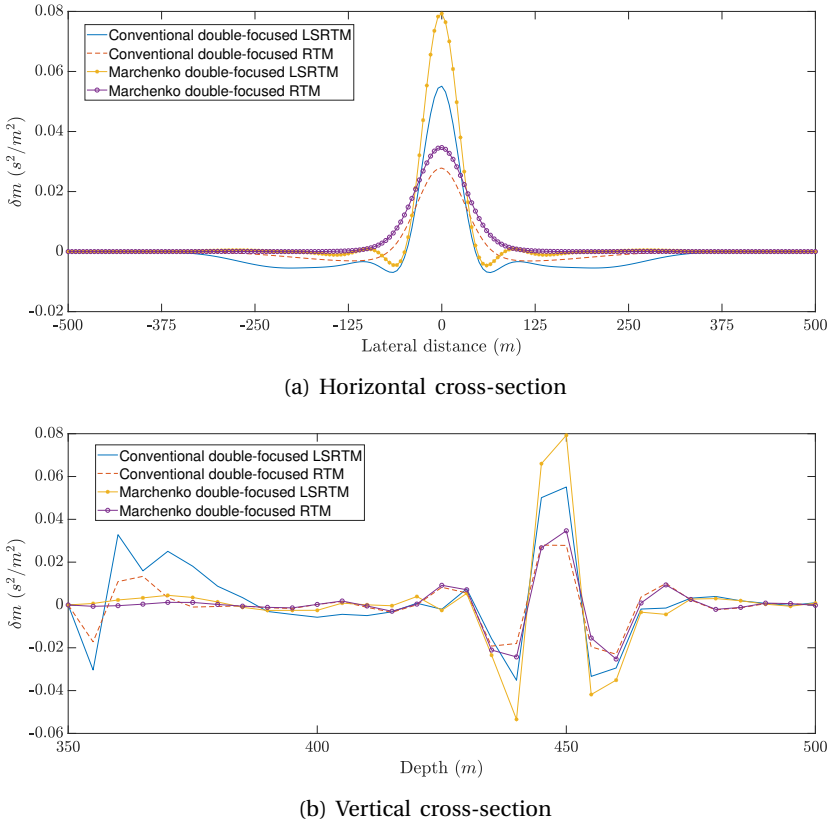

(b) Vertical cross-section

Figure 2.9.: A comparison of the horizontal and vertical cross-section of the retrieved image of the simple model with different approaches. a) A horizontal cross-section at depth of 450 m, and b) A vertical cross section at lateral distance zero.

Figures 2.17a and 2.17b. As these figures are showing, our approach has a superior vertical resolution and lateral continuity. A comparison of the cost functions of these different approaches to TOLSRTM is also shown in Figure 2.18. TOLSRTM converges faster when Mdf (instead of Cdf) is used for redatuming, since the multiple reflections are correctly taken into account.

2.3.2. INVESTIGATING THE EFFECT OF THE POINT-SPREAD FUNCTION

In this section, we investigate the effect of the PSF and the necessity of applying it to the reflection response of the target area. In Figure 2.19, we show the effect of the PSF (Eq. 4.15) on the true reflection response (as modeled during each iteration of TOLSRTM) of the target area of the simple model and compare it with Marchenko
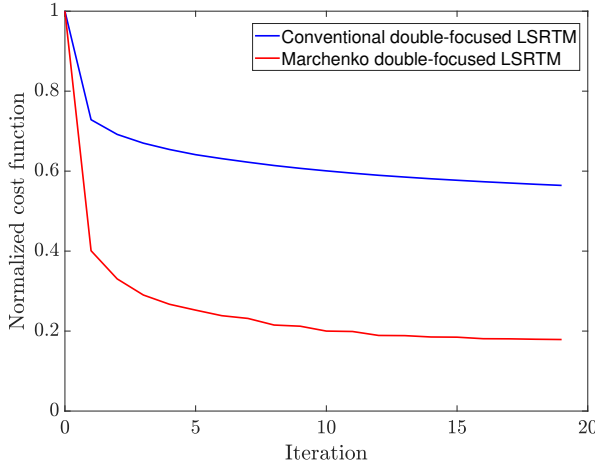
Figure 2.10.: A comparison between convergence rate of cost functions of different approaches to TOLSRM for the simple model.

double-focused data. Figure 2.19a shows the modeled data (Eq. 2.28) in the true perturbation model without PSF. Figure 2.19b shows the same after the PSF has been applied. Figure 2.19c shows the Marchenko double-focused data. We can see the effect of the PSF by analyzing Figures 2.19b and 2.19c. The PSF not only imposes a band limitation on the data but also dampens the far-offsets such that the predicted data fits the observed data better. Thus, applying the PSF to the reflection response is necessary for better convergence. Moreover, in Figure 2.20 the cost function of TOLSRTM with and without PSF is shown. From this Figure, we conclude that including the PSF in our formulation successfully improves the convergence.

2.3.3. INACCURATE VELOCITY MODEL

To determine the sensitivity of our algorithm to kinematic errors, we define a model similar to the model with a syncline in the overburden but with a high-velocity inclusion in the overburden and a more complex target (Fig. 2.21a). We use a smooth version of this model (Fig. 2.21b) to estimate the direct arrival between the surface and the focusing level. In addition, we use the target part of this smooth velocity model to compute the background Green's functions with a finite difference algorithm for the forward and adjoint kernels. The density model is shown in Figure 2.21c. In Figure 2.22 we show images as obtained by applying our methodology with the inaccurate velocity model. The yellow arrows and ellipses in Figure 2.22 indicate discontinuities and depth estimation errors caused by velocity inaccuracies. Moreover, the red arrows in this figure designate a couple of artifacts that are removed by our method, and the white arrows and ellipses show the amplitude improvements resulting from our method. Despite the fact

2
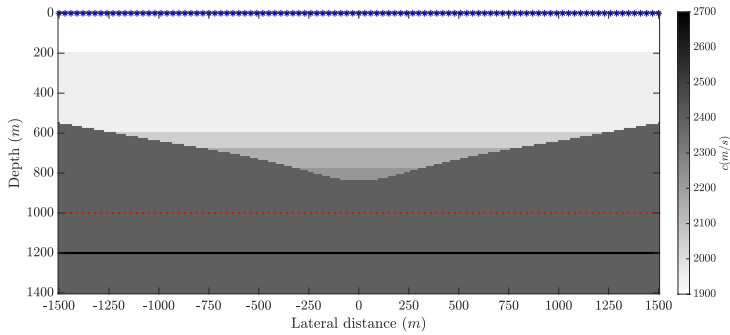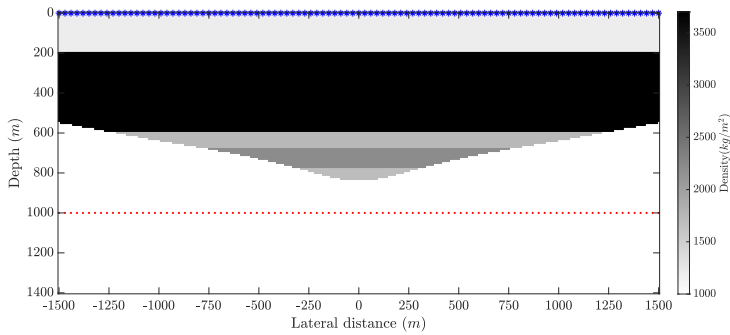
(a) Velocity model

(b) Density model

Figure 2.11.: Velocity and density of the model with the syncline overburden and a line reflector in the target.

that we use a wrong velocity model, our algorithm which is based on Marchenko double-focusing is still able to correctly predict and reduce the artifacts caused by the overburden-related multiple reflections and improves the quality and amplitude recovery of the LSRTM image. The observation that Marchenko imaging is not sensitive to errors in the velocity model is not new, see for instance Broggini et al. [39].

2.4. DISCUSSION

Our numerical results suggest that our Marchenko target-oriented LSRTM can recover a clearer image of the target of interest than conventional TOLSRTM. The retrieved
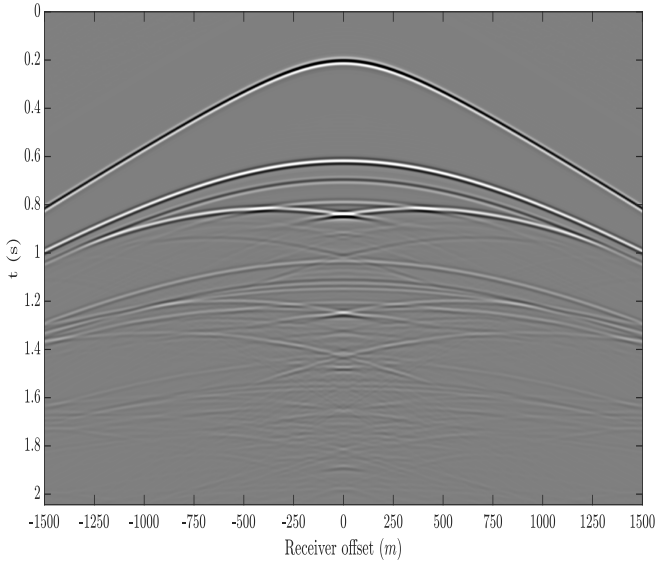
Figure 2.12.: Common-source record at the surface of a source located at lateral distance = 0 in the model with the syncline overburden. A linear time-varying ($\frac{t}{dt}$) gain is applied to this record to amplify weaker events.

image of the model with single-layered overburden using Marchenko double-focusing (Fig. 2.8b) has no (or at least a reduced) imprint of the overburden-related spurious reflector. In contrast, the recovered image using conventional redatuming operators (Fig. 2.7b) could not handle this spurious reflector even after 20 iterations. A further investigation into the resolution improvement of our LSRTM algorithm compared to the conventional double-focused LSRTM, shows that our algorithm is able to improve the resolution in both horizontal and vertical directions (Fig. 2.9). The model with the syncline overburden demonstrates the power of using Marchenko double-focusing for target-oriented LSRTM in removing the strong overburden-related multiple reflection artifacts. The image that is obtained with the conventional redatuming operator (Fig. 2.15b) is overwhelmed by artifacts from the overburden. On the other hand, our algorithm is able to remove these artifacts and retrieves a clear image of the target area (Fig. 2.16b). In addition, our TOLSRTM algorithm can model data that can predict the interactions between the target area and the overburden without the knowledge of the overburden reflectivity model. Moreover, the Marchenko equation has been derived for elastic media too [40–42]. Hence, we expect that the current methodology can also be extended to elastic LSRTM.

Furthermore, a comparison between Figure 2.4b and Figure 2.19 shows the necessity of applying the PSF to the modeled reflection data of the target. Without imposing this PSF on the modeled data, the predicted data (Fig. 2.19a) do not match
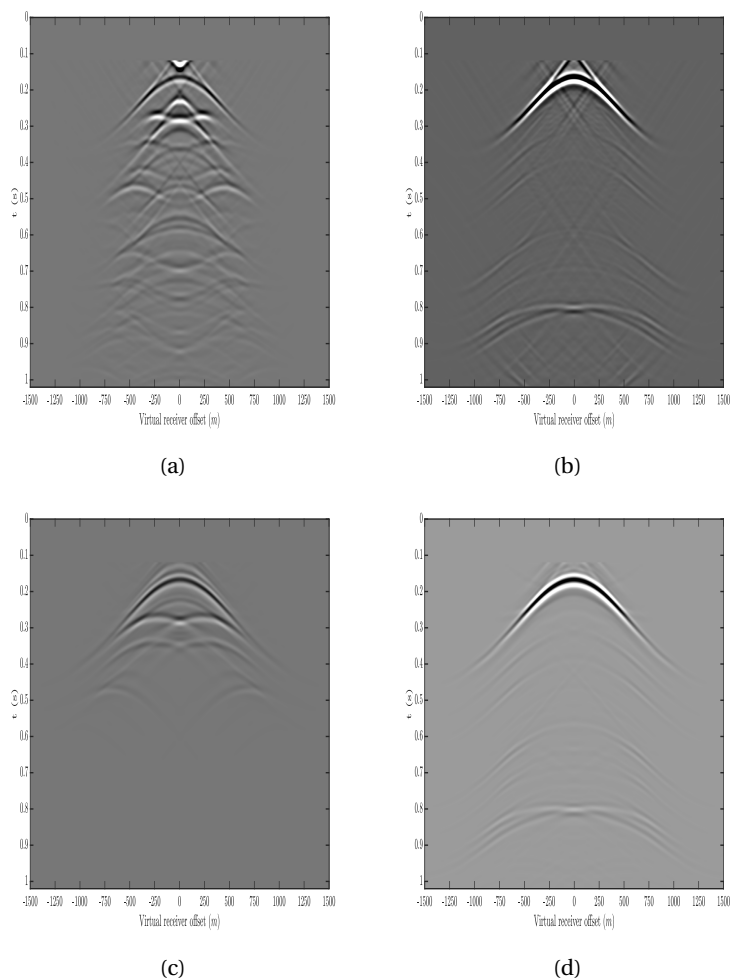
(a)   (b)

(c)   (d)

Figure 2.13.: A comparison between Double-focused data and predicted data of the model with the syncline overburden corresponding to the middle virtual source. a) Conventional double-focused data, b) Marchenko double-focused data, c) predicted data of conventional double-focusing, and d) predicted data of Marchenko double-focusing. The first few time samples are set to zero to mute focusing artifacts. The maximum and the minimum value of the grey-level scale of all figures are the same.

the observed data (Fig. 2.19c). Hence, the TOLSRTM without PSF converges slowly compared to the case where the PSF is applied to it (Fig. 2.20).

In our last example, we addressed the issue of velocity inaccuracies in the

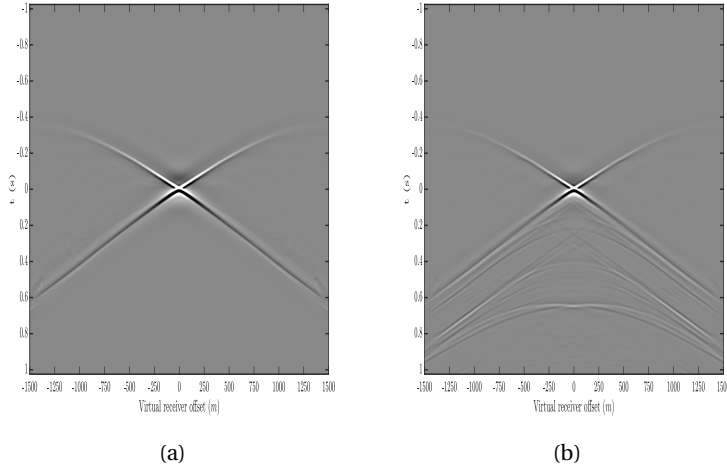(a)   (b)

Figure 2.14.: Virtual source wavefield of the model with the syncline overburden for the middle virtual source. a) The conventional double-focused source ($G_{Cdf}^{+,+}$) by applying conventional redatuming operators, and b) Marchenko double-focused source ($G_{Mdf}^{+,+}$). The maximum and the minimum value of the grey-level scale of both figures are the same.
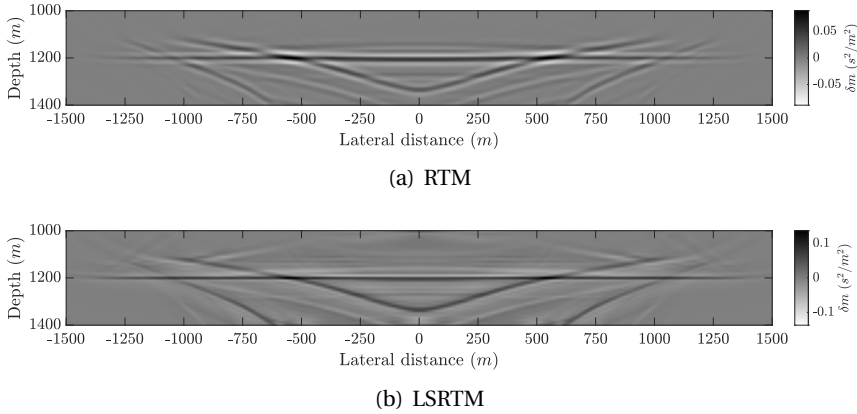

(a) RTM

(b) LSRTM

Figure 2.15.: Retrieved target image of the model with the syncline overburden by conventional double-focusing operators. a) RTM, and b) LSRTM after 20 iterations

overburden. As Figure 2.22 shows our method is able to improve the quality of the image by suppressing the overburden-generated multiples and predicting the interactions between target and overburden, even if the overburden velocity model
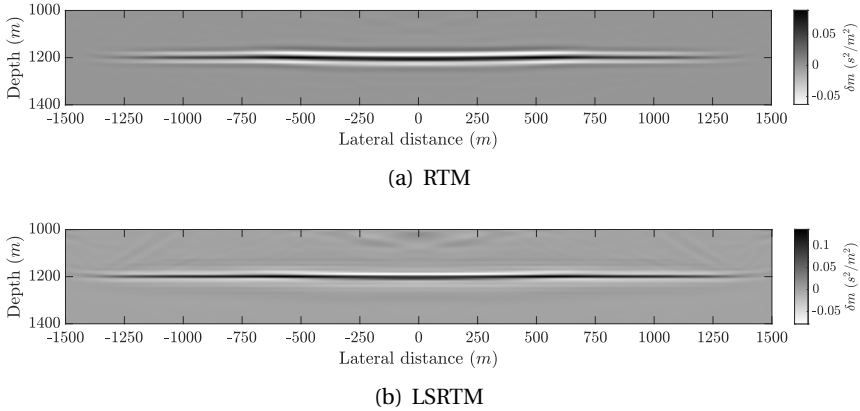
(a) RTM

(b) LSRTM

Figure 2.16.: Retrieved target image of the model with the syncline overburden by Marchenko double-focusing. a) RTM, and b) LSRTM after 20 iterations.

is inaccurate.

The Marchenko redatuming algorithm used in this chapter requires surface-related multiples to be removed from the acquired reflection data. However, researchers exploited the possibility of including the surface-related multiple reflections within the Marchenko framework [23, 25, 43]. Consequently, it is quite straightforward to include surface-related multiples in our algorithm.

2.5. CONCLUSION

We have introduced a target-oriented LSRTM algorithm that can correctly handle the internal multiple reflections generated in the overburden and interactions between target and overburden. To achieve this, we solved the Marchenko equations to obtain the Marchenko double-focused data and the downgoing part of the focusing function. By having these Green's functions and focusing operators, we can formulate a Born integral that can be used as the forward modeling operator and an adjoint modeling operator can also be constructed for target-oriented LSRTM. Importantly, we have to apply a point-spread function to the reflection response of the target to account for the finite spatial bandwidth caused by the overburden and the finite recording aperture at the acquisition surface.

Since LSRTM and full waveform inversion are closely related, the question may arise: "Can we modify our algorithm for target-oriented full waveform inversion?". To address this question, in the appendix of this thesis, I propose a method based on Marchenko target-replacement technique to develop a 1D target-oriented FWI algorithm. Despite the acceptable performance of the proposed method in the
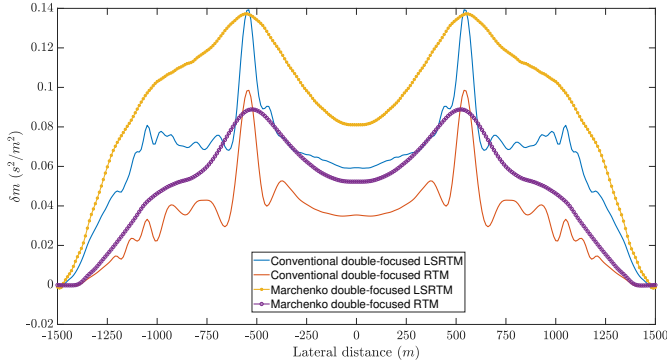
(a) Horizontal cross-section
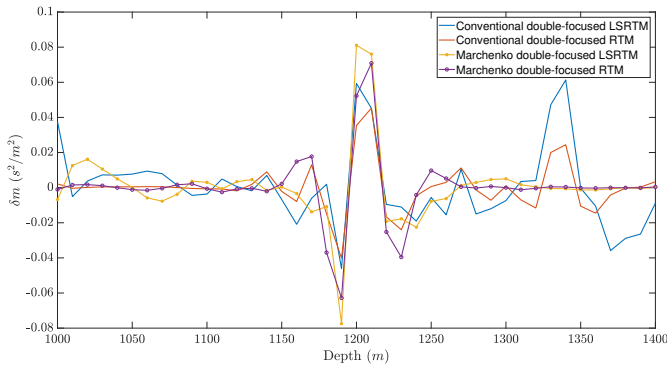
(b) Vertical cross-section

Figure 2.17.: A Comparison of the Horizontal and vertical cross-section of the retrieved image of the model with the syncline overburden with different approaches. a) A horizontal cross-section at depth of 1200 m, and b) A vertical cross-section at lateral distance zero.

appendix for the 1D situation, we have to mention that the double-focused data does not include the diving waves, so it is dominated by the medium-to-short wavelengths and does not include long wavelengths. These long wavelengths are crucial for velocity recovery in the 2D and 3D full waveform inversion process. Moreover, the evanescent waves, such as refracted waves, are not handled by the current redatuming methodologies. The aforementioned issues put a limit on modifying our algorithm to be applied for target-oriented full waveform inversion, which requires long-to-medium wavelengths. However, recently some advancement has been made towards including evanescent waves within the Marchenko framework [44–46]. Nevertheless, the double-focused data contains all target reflections correctly (but not the other waveforms). Therefore, another possible future direction of
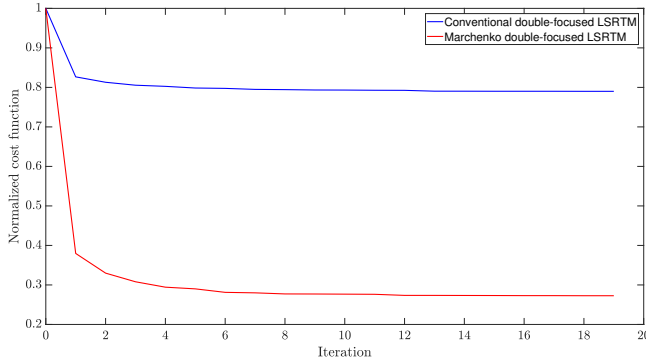
Figure 2.18.: A comparison between convergence rate of cost functions of different approaches to TOLSRM for the model with the syncline overburden.

this research is to investigate the potential of our method in improving inversion methods that rely on reflections only, such as joint migration inversion [47] and reflection waveform inversion [48].

In recent years, the focus of the seismic exploration community has shifted toward fast and high-resolution imaging and inversion methods. Our proposed target-oriented LSRTM is able to produce such images in a relatively small target region and has a relatively faster convergence rate while correctly accounting for multiple reflections caused by the overburden.
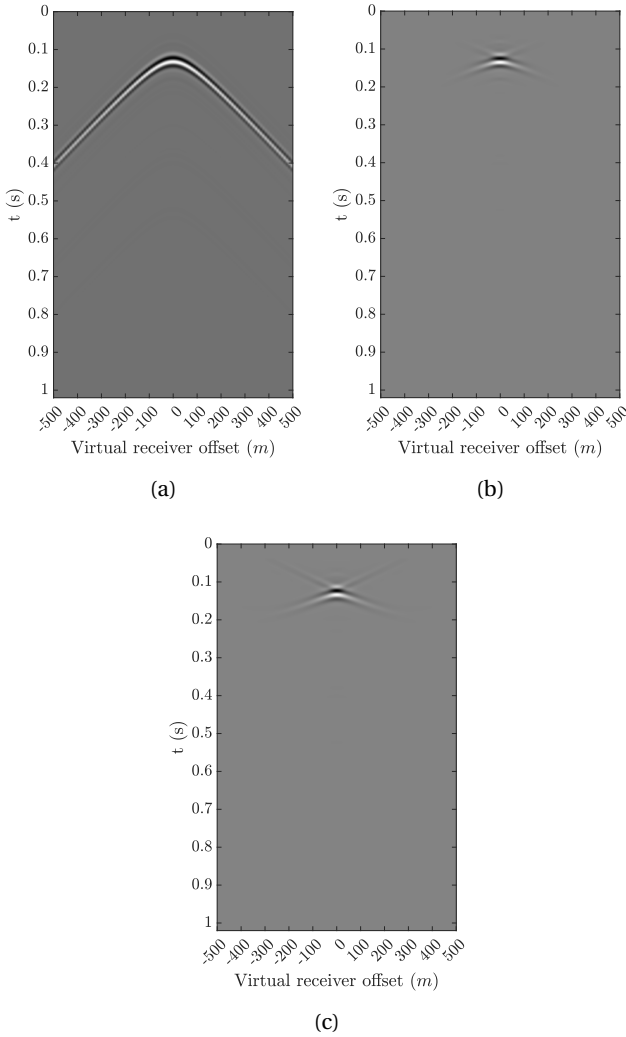
(a)

(b)

(c)

Figure 2.19.: Comparison of the reflection response of target area of the model with a single-layered overburden. a) Without PSF, and b) With PSF, and c) double-focused data. The maximum and the minimum value of the grey-level scale of figures are set to the maximum and the minimum of the input.
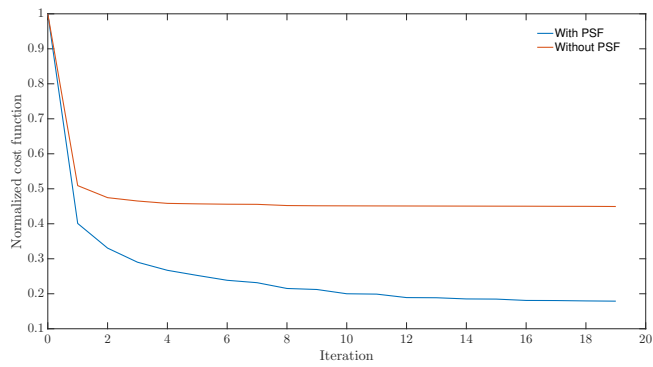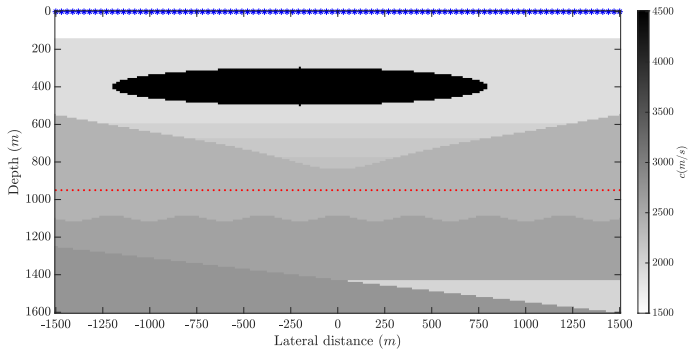
2

Figure 2.20.: Comparison of the cost function of the TOLSRTM with and without PSF.

(a)
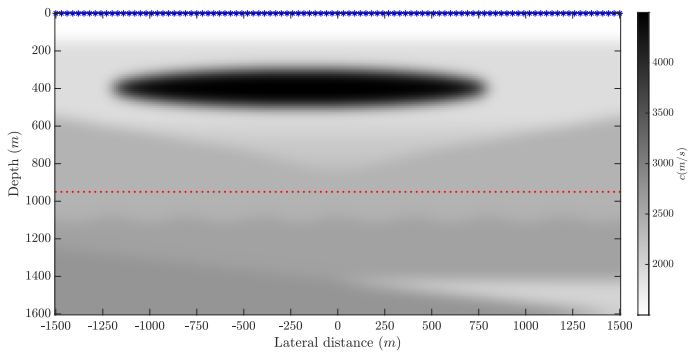
(b)
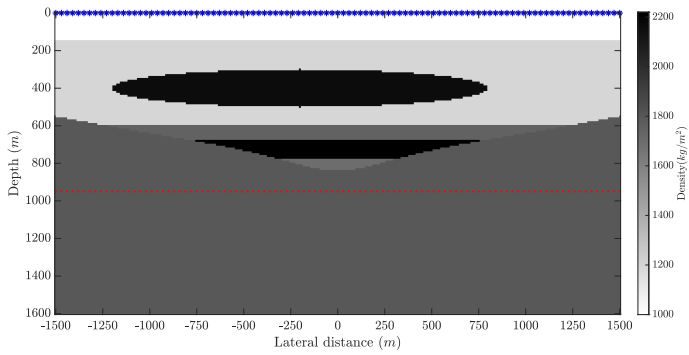
(c)

Figure 2.21.: Velocity model: a) True model, b) smooth model, and c) density model

(a)

(b)
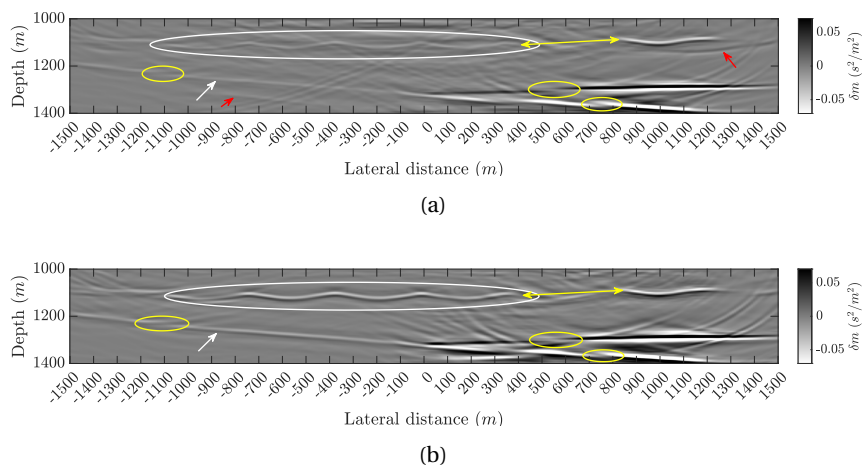
Figure 2.22.: Target-oriented LSRTM with the Erroneous velocity model. a) Conventional double-focusing, and b) Marchenko double-focusing. The red arrows show some overburden artifacts that are removed, the white arrows and ellipses show amplitude improvement and the yellow ones show some of the effects of velocity errors. The value of the grey-level scale is set to 25% of the maximum value.

REFERENCES

[1] A. Shoja, J. van der Neut and K. Wapenaar. 'Target-oriented least-squares reverse-time migration using Marchenko double-focusing: reducing the artefacts caused by overburden multiples'. In: *Geophysical Journal International* 233.1 (Apr. 2023), pp. 13–32. DOI: 10.1093/gji/ggac438.

[2] G. T. Schuster. *SEISMIC INVERSION*. Society of Exploration Geophysicists, 2017.

[3] E. Baysal, D. D. Kosloff and J. W. C. Sherwood. 'Reverse time migration'. In: *GEOPHYSICS* 48.11 (1983), pp. 1514–1524. DOI: 10.1190/1.1441434.

[4] H.-W. Zhou, H. Hu, Z. Zou, Y. Wo and O. Youn. 'Reverse time migration: A prospect of seismic imaging methodology'. In: *Earth-Science Reviews* 179 (2018), pp. 207–227. DOI: https://doi.org/10.1016/j.earscirev.2018.02.008.

[5] L. Zhang, E. Slob, J. van der Neut and K. Wapenaar. 'Artifact-free reverse time migration'. In: *GEOPHYSICS* 83.5 (2018), A65–A68. DOI: 10.1190/geo2017-0795.1.

[6] G. Dutta, M. Giboli, C. Agut, P. Williamson and G. T. Schuster. 'Least-squares reverse time migration with local Radon-based preconditioning'. In: *GEOPHYSICS* 82.2 (2017), S75–S84. DOI: 10.1190/geo2016-0117.1.

[7] Y. Tang. 'Target-oriented wave-equation least-squares migration/inversion with phase-encoded Hessian'. In: *GEOPHYSICS* 74.6 (2009), WCA95–WCA107. DOI: 10.1190/1.3204768.

[8] Y. Liu, X. Liu, A. Osen, Y. Shao, H. Hu and Y. Zheng. 'Least-squares reverse time migration using controlled-order multiple reflections'. In: *GEOPHYSICS* 81.5 (2016), S347–S357. DOI: 10.1190/geo2015-0479.1.

[9] W. Dai, P. Fowler and G. T. Schuster. 'Multi-source least-squares reverse time migration'. In: *Geophysical Prospecting* 60.4 (2012), pp. 681–695. DOI: https://doi.org/10.1111/j.1365-2478.2012.01092.x.

[10] F. J. Herrmann and X. Li. 'Efficient least-squares imaging with sparsity promotion and compressive sensing'. In: *Geophysical Prospecting* 60.4 (2012), pp. 696–712. DOI: https://doi.org/10.1111/j.1365-2478.2011.01041.x.

[11] M. Farshad and H. Chauris. 'Sparsity-promoting multiparameter pseudoinverse Born inversion in acoustic media'. In: *GEOPHYSICS* 86.3 (2021), S205–S220. DOI: 10.1190/geo2020-0527.1.

[12] A. A. Valenciano, B. Biondi and A. Guitton. 'Target-oriented wave-equation inversion'. In: *GEOPHYSICS* 71.4 (2006), A35–A38. DOI: 10.1190/1.2213359.

[13] P. Haffinger, A. Gisolf and P. M. v. d. Berg. 'Towards high resolution quantitative subsurface models by full waveform inversion'. In: *Geophysical Journal International* 193.2 (Feb. 2013), pp. 788–797. ISSN: 0956-540X. DOI: 10.1093/gji/ggt021.

[14] B. Willemsen, A. Malcolm and W. Lewis. 'A numerically exact local solver applied to salt boundary inversion in seismic full-waveform inversion'. In: *Geophysical Journal International* 204.3 (Feb. 2016), pp. 1703–1720. DOI: 10.1093/gji/ggv547.

[15] S. Yuan, N. Fuji, S. Singh and D. Borisov. 'Localized time-lapse elastic waveform inversion using wavefield injection and extrapolation: 2-D parametric studies'. In: *Geophysical Journal International* 209.3 (Mar. 2017), pp. 1699–1717. DOI: 10.1093/gji/ggx118.

[16] Z. Zhao and M. K. Sen. 'Fast image-domain target-oriented least-squares reverse time migration'. In: *GEOPHYSICS* 83.6 (2018), A81–A86. DOI: 10.1190/geo2018-0033.1.

[17] Q. Guo and T. Alkhalifah. 'Target-oriented waveform redatuming and high-resolution inversion: Role of the overburden'. In: *GEOPHYSICS* 85.6 (2020), R525–R536. DOI: 10.1190/geo2019-0640.1.

[18] J. R. Berryhill. 'Wavĕequation datuming before stack'. In: *GEOPHYSICS* 49.11 (1984), pp. 2064–2066. DOI: 10.1190/1.1441620.

[19] G. T. Schuster and M. Zhou. 'A theoretical overview of model-based and correlation-based redatuming methods'. In: *GEOPHYSICS* 71.4 (2006), SI103–SI110. DOI: 10.1190/1.2208967.

[20] N. Luiken and T. van Leeuwen. 'Seismic wavefield redatuming with regularized multi-dimensional deconvolution'. In: *Inverse Problems* 36.9 (Sept. 2020). DOI: 10.1088/1361-6420/aba9d1.

[21] D. F. Barrera, J. Schleicher and J. Brackenhoff. 'Interferometric redatuming by deconvolution and correlation-based focusing'. In: *GEOPHYSICS* 86.1 (2021), Q1–Q13. DOI: 10.1190/geo2019-0208.1.

[22] Q. Guo and T. Alkhalifah. 'Datum-based waveform inversion using a subsurface-scattering imaging condition'. In: *GEOPHYSICS* 84.4 (2019), S251–S266. DOI: 10.1190/geo2018-0615.1.

[23] M. Ravasi. 'Rayleigh-Marchenko redatuming for target-oriented, true-amplitude imaging'. In: *GEOPHYSICS* 82.6 (2017), S439–S452. DOI: 10.1190/geo2017-0262.1.

[24] D. Vargas, I. Vasconcelos, Y. Sripanich and M. Ravasi. 'Scattering-based focusing for imaging in highly complex media from band-limited, multicomponent data'. In: *GEOPHYSICS* 86.5 (2021), WC141–WC157. DOI: 10.1190/geo2020-0939.1.

[25] M. Dukalski and K. de Vos. 'Marchenko inversion in a strong scattering regime including surface-related multiples'. In: *Geophysical Journal International* 212.2 (Oct. 2017), pp. 760–776. DOI: 10.1093/gji/ggx434.

[26] K. Wapenaar, J. Thorbecke, J. van der Neut, F. Broggini, E. Slob and R. Snieder. 'Marchenko imaging'. In: *GEOPHYSICS* 79.3 (2014), WA39–WA57. DOI: 10.1190/geo2013-0302.1.

[27] L. Diekmann, I. Vasconcelos, D. Cummings and A. Curtis. 'Towards exact linearized full-waveform inversion via Marchenko redatuming'. In: *First International Meeting for Applied Geoscience & Energy Expanded Abstracts*. 2021, pp. 3380–3384. DOI: 10.1190/segam2021-3583558.1.

[28] T. Cui, J. Rickett, I. Vasconcelos and B. Veitch. ' Target-oriented full-waveform inversion using Marchenko redatumed wavefields'. In: *Geophysical Journal International* 223.2 (July 2020), pp. 792–810. ISSN: 0956-540X. DOI: 10.1093/gji/ggaa333.

[29] M. Staring, R. Pereira, H. Douma, J. van der Neut and K. Wapenaar. 'Source-receiver Marchenko redatuming on field data using an adaptive double-focusing method'. In: *GEOPHYSICS* 83.6 (2018), S579–S590. DOI: 10.1190/geo2017-0796.1.

[30] M. Born, E. Wolf, A. B. Bhatia, P. C. Clemmow, D. Gabor, A. R. Stokes, A. M. Taylor, P. A. Wayman and W. L. Wilcock. *Principles of Optics: Electromagnetic Theory of Propagation, Interference and Diffraction of Light*. 7th ed. Cambridge University Press, 1999. DOI: 10.1017/CBO9781139644181.

[31] D. W. Marquardt. 'An Algorithm for Least-Squares Estimation of Nonlinear Parameters'. In: *Journal of the Society for Industrial and Applied Mathematics* 11.2 (1963), pp. 431–441. URL: http://www.jstor.org/stable/2098941.

[32] J. W. Thorbecke, E. Slob, J. Brackenhoff, J. van der Neut and K. Wapenaar. 'Implementation of the Marchenko method'. In: *GEOPHYSICS* 82.6 (2017), WB29–WB45. DOI: 10.1190/geo2017-0108.1.

[33] K. Wapenaar, J. Fokkema, M. Dillen and P. Scherpenhuijsen. 'One-way acoustic reciprocity and its applications in multiple elimination and time-lapse seismics'. In: *SEG Technical Program Expanded Abstracts 2000*. 2005, pp. 2377–2380. DOI: 10.1190/1.1815939.

[34] S. Shoja, G. Meles and K. Wapenaar. 'A Proposal for Marchenko-Based Target-Oriented Full Waveform Inversion'. In: *Proceedings of EAGE 2020 Annual Conference & Exhibition Online* 2020.1 (2020), pp. 1–5. DOI: https://doi.org/10.3997/2214-4609.202011020.

[35] K. Wapenaar and M. Staring. 'Marchenko-Based Target Replacement, Accounting for All Orders of Multiple Reflections'. In: *Journal of Geophysical Research: Solid Earth* 123.6 (2018), pp. 4942–4964. DOI: https://doi.org/10.1029/2017JB015208.

[36] J. W. Thorbecke and D. Draganov. 'Finite-difference modeling experiments for seismic interferometry'. In: *GEOPHYSICS* 76.6 (2011), H1–H18. DOI: 10.1190/geo2010-0039.1.

[37] M. P. M. and H. Feshbach. *Methods of Theoretical Physics*. New York: McGraw-Hill, 1953.

[38] P. M. van den Berg. 'Acoustic Waves'. In: *Forward and Inverse Scattering Algorithms based on Contrast Source Integral Equations*. John Wiley & Sons, Ltd, 2021. Chap. 2, pp. 79–179. ISBN: 9781119741602. DOI: https://doi.org/10.1002/9781119741602.ch2.

[39] F. Broggini, R. Snieder and K. Wapenaar. 'Data-driven wavefield focusing and imaging with multidimensional deconvolution: Numerical examples for reflection data with internal multiples'. In: *GEOPHYSICS* 79.3 (2014), WA107–WA115. DOI: 10.1190/geo2013-0307.1.

[40] C. Reinicke, M. Dukalski and K. Wapenaar. 'Comparison of monotonicity challenges encountered by the inverse scattering series and the Marchenko demultiple method for elastic waves'. In: *GEOPHYSICS* 85.5 (2020), Q11–Q26. DOI: 10.1190/geo2019-0674.1.

[41] K. Wapenaar and E. Slob. 'On the Marchenko equation for multicomponent single-sided reflection data'. In: *Geophysical Journal International* 199.3 (Oct. 2014), pp. 1367–1371. DOI: 10.1093/gji/ggu313.

[42] C. A. da Costa Filho, M. Ravasi, A. Curtis and G. A. Meles. 'Elastodynamic Green's function retrieval through single-sided Marchenko inverse scattering'. In: *Phys. Rev. E* 90 (6 2014), p. 063201. DOI: 10.1103/PhysRevE.90.063201.

[43] S. Singh, R. Snieder, J. van der Neut, J. Thorbecke, E. Slob and K. Wapenaar. 'Accounting for free-surface multiples in Marchenko imaging'. In: *GEOPHYSICS* 82.1 (2017), R19–R30. DOI: 10.1190/geo2015-0646.1.

[44] K. Wapenaar, R. Snieder, S. de Ridder and E. Slob. 'GreenŠs function representations for Marchenko imaging without up/down decomposition'. In: *Geophysical Journal International* 227.1 (June 2021), pp. 184–203. DOI: 10.1093/gji/ggab220.

[45] K. Wapenaar. 'The Marchenko method for evanescent waves'. In: *Geophysical Journal International* 223.2 (Aug. 2020), pp. 1412–1417. DOI: 10.1093/gji/ggaa375.

[46] L. Diekmann and I. Vasconcelos. 'Focusing and Green's function retrieval in three-dimensional inverse scattering revisited: A single-sided Marchenko integral for the full wave field'. In: *Phys. Rev. Research* 3 (1 2021), p. 013206. DOI: 10.1103/PhysRevResearch.3.013206.

[47] D. J. Verschuur, X. R. Staal and A. J. Berkhout. 'Joint migration inversion: Simultaneous determination of velocity fields and depth images using all orders of scattering'. In: *The Leading Edge* 35.12 (2016), pp. 1037–1046. DOI: 10.1190/tle35121037.1.

[48] R. Brossier, S. Operto and J. Virieux. 'Velocity model building from seismic reflection data by full-waveform inversion'. In: *Geophysical Prospecting* 63.2 (2015), pp. 354–367. DOI: https://doi.org/10.1111/1365-2478.12190.

3

TARGET-ENCLOSED LEAST-SQUARES SEISMIC IMAGING

Least-Squares Reverse-Time Migration (LSRTM) is a method that seismologists utilize to compute a high-resolution subsurface image. Nevertheless, LSRTM is a computationally demanding problem. One way to reduce the computational costs of the LSRTM is to choose a small region of interest and compute the image of that region. However, finding representations that account for the wavefields entering the target region from the surrounding boundaries is necessary. This chapter confines the region of interest between two boundaries above and below this region. The acoustic reciprocity theorem is employed to derive representations for the wavefields at the upper and lower boundaries of the target region. With the help of these representations, a target-enclosed LSRTM algorithm is developed to compute a high-resolution image of the region of interest. Moreover, the possibility of using virtual receivers created by Marchenko redatuming is investigated.

3.1. INTRODUCTION

Wavefield migration is the art of computing the medium reflectivity from the recorded wavefield passing through the medium. Many migration algorithms are available, such as Kirchhoff migration [2], one-way wave equation migration [3], and Reverse-Time Migration (RTM) [4–6]. RTM is one of the common migration algorithms. RTM is commonly implemented by applying the adjoint of the Born operator to the recorded data [7]. However, the inverse of the operator is needed for the true image. Consequently, the migration result suffers from amplitude and resolution issues [8–10]. One way to address this problem is to solve the migration problem with a least-squares solution called Least-Squares Reverse-Time Migration (LSRTM). The least-squares solution is usually applied as an iterative optimization problem.

However, LSRTM is computationally expensive [9, 11–13]. To reduce the computation cost of the LSRTM, one can reduce the computation domain by confining the model to a Region of Interest (ROI) by recording or computing the wavefields at the boundary of this region. The process of migrating for a ROI is called target-oriented migration [14–20]. However, deploying receivers on the boundaries of ROI usually is not possible due to physical obstacles.

Due to the aforementioned accessibility issue, the typical approach for target-oriented migration is to opt for redatuming algorithms and only consider the upper horizontal boundary of the ROI or target [19, 21–27]. In cases where the ROI is enclosed between two boundaries, i.e., when wavefields are entering the ROI from the underburden through the lower boundary [28, 29], the shortcoming of only considering the upper boundary is that any wavefield entering the ROI from the medium below the lower boundary of the ROI is unaccounted for, hindering the convergence of the inversion process. Moreover, including the lower boundary in the algorithm can add transmission information to the inversion. However, including the lower boundary in the inversion process has rarely been studied directly. For instance, Cui et al. [30] derive a representation with a reciprocity theorem and Marchenko redatuming to include surrounding boundaries in target-oriented full waveform inversion (FWI), Diekmann et al. [31] use a Marchenko retrieved Green's function of the ROI and insert it in the Lippmann-Schwinger integral to create a linear inversion process, and van der Neut et al. [32] design a target-enclosed imaging algorithm with the help of a reciprocity theorem. Of the above-mentioned papers, only [32] directly studies the consequences of including the lower boundary in the imaging process, and the others only implicitly imply the effects of it.

This chapter, which is an extension of [32], studies the contribution of the lower boundary by introducing a target-enclosed LSRTM algorithm. To derive this algorithm, we start by explaining the LSRTM briefly. Next, we derive a target-enclosed representation for Green's functions on the upper and lower boundaries of the ROI by using the reciprocity theorem. Then, we connect this target-enclosed representation to LSRTM to complete our algorithm. After deriving the required equations, we

test our algorithm with numerical examples. First, we use physical receivers at the boundaries of the ROI to check the results in the ideal situation. Then, we briefly introduce Marchenko redatuming to explore the possibility of using virtual receivers in our algorithm. For both physical and virtual receivers cases we use both a homogeneous background and a smooth background velocity as the velocity model for migration. Finally, we finish the chapter by discussing the results and providing a conclusion.

3.2. THEORY

To develop the theory, we start with a brief discussion of LSRTM. Next, a representation of the target-enclosed Green's function is given with the help of the reciprocity theorem. Finally, to derive our target-enclosed LSRTM formulation, we combine LSRTM with the target-enclosed representations. In the entire theory section, we are in the frequency-space domain, and for simplicity, we drop the dependency on angular frequency (ω).

3.2.1. LEAST-SQUARES REVERSE-TIME MIGRATION

We start the explanation of LSRTM by investigating the Born integral for the scattered wavefield by a scattering potential [7, 33, 34]. Here we follow the convention of [34]:

$$P^{scat}(\mathbf{x}') = \int_{\mathcal{V}} \gamma_0^2(\mathbf{x}) G_0(\mathbf{x}',\mathbf{x}) \chi^c(\mathbf{x}) P^{inc}(\mathbf{x}) d\mathbf{x}. \tag{3.1}$$

In this equation, $\mathbf{x}'$ is the observation location, $\mathbf{x}$ is a location inside the computation volume ($\mathcal{V}$), $P^{scat}(\mathbf{x}')$ is the scattered pressure field at the observation point, $P^{inc}(\mathbf{x})$ is the incident pressure field at the computation point and $G_0(\mathbf{x}',\mathbf{x})$ is the background Green's function between $\mathbf{x}$ and $\mathbf{x}'$. Moreover, $\gamma_0(\mathbf{x}) = \frac{-i\omega}{c_0(\mathbf{x})}$ and $\chi^c(\mathbf{x}) = 1 - \frac{c_0^2(\mathbf{x})}{(c^{scat}(\mathbf{x}))^2}$ is the propagation velocity perturbation, where $c_0(\mathbf{x})$ and $c^{scat}(\mathbf{x})$ are the background and scatterer's velocity, respectively.

It is possible to rewrite this equation in matrix form:

$$\mathbf{P}_{pred}^{scat}(\delta\mathbf{m}) = \mathbf{L}\delta\mathbf{m}. \tag{3.2}$$

Here, $\mathbf{L}$ is matrix form of the integral operator of equation 3.1 and $\delta\mathbf{m}$ is a vector, containing the perturbation $\chi^c(\mathbf{x})$.

To obtain an estimation of $\delta\mathbf{m}$, we can apply the adjoint of $\mathbf{L}$ to the observed data:

$$\delta\mathbf{m}^{img} = \mathbf{L}^\dagger \mathbf{P}_{obs}^{scat}, \tag{3.3}$$

where $\dagger$ denotes complex conjugate transposition.

We can go one step further to obtain a high-resolution estimation of the image by minimizing the following objective function [35]:

$$J(\delta\mathbf{m}) = \frac{1}{2}\|\mathbf{P}^{scat}_{pred}(\delta\mathbf{m}) - \mathbf{P}^{scat}_{obs}\|^2_2. \tag{3.4}$$

Different optimization algorithms, such as conjugate gradient, can minimize this function. This optimization problem is known as Least-Squares Reverse-Time Migration (LSRTM).

3.2.2. TARGET-ENCLOSED REPRESENTATIONS

LSRTM is a computationally expensive algorithm. In order to reduce its computational burden, seismologists usually opt for a target-oriented algorithm, limiting the medium to a smaller region. As we mentioned in section 3.1, target-oriented algorithms usually redatum the data to the upper boundary of the target and ignore any information coming from the lower boundary.

In this section, the idea is to find a representation that can account for a heterogeneous medium above the upper and below the lower boundary of the target area. To derive this representation, we follow [32]. The starting point of the derivation is the acoustic reciprocity theorem of the convolution type [22], which connects the wavefields of two different states via

$$\int_{\partial\mathcal{V}_u} \rho^{-1}(p^+_A(\partial_3 p^-_B) + p^-_A(\partial_3 p^+_B))d\mathbf{x} = \int_{\partial\mathcal{V}_l} \rho^{-1}(p^+_A(\partial_3 p^-_B) + p^-_A(\partial_3 p^+_B))d\mathbf{x}. \tag{3.5}$$

Here, we consider a volume $\mathcal{V}$, which is limited by two infinite horizontal surfaces. States A and B (Fig. 3.1) are defined in two different media which are identical inside the volume $\mathcal{V}$ with boundaries denoted by $\partial\mathcal{V}_u$ (upper) and $\partial\mathcal{V}_l$ (lower), and arbitrary outside of this volume. In addition, p^+ and p^- are decomposed wavefields on the boundaries where + means downgoing and − means upgoing, and ∂_3 is the partial derivative in direction x_3 (downward).

To continue the derivation we define Green's function $G(\mathbf{x},\mathbf{x}_s)$ as the solution of the following Helmholtz equation:

$$\nabla^2 G + k(\mathbf{x})^2 G = -\rho\delta(\mathbf{x}-\mathbf{x}_s), \tag{3.6}$$

where $k(\mathbf{x}) = \frac{\omega}{c(\mathbf{x})}$ is the wavenumber, and c is the propagation velocity.

A representation for Green's function at the upper boundary of the target ($\partial\mathcal{V}_u$) can be derived by defining state A in the actual medium and state B in a medium identical to medium A inside the volume $\mathcal{V}$ (target) and homogeneous outside of it. We denote the Green's functions of state A with $G(\mathbf{x},\mathbf{x}_s)$ and Green's function of state B with $G_{tar}(\mathbf{x},\mathbf{x}_u)$. In state A we define $p^{\pm}_A = G^{\pm}(\mathbf{x},\mathbf{x}_s)$, where $\mathbf{x}_s$ is a location at Earth's surface $\partial\mathcal{V}_0$. For state B we have $p^{\pm}_B = G^{\pm}_{tar}(\mathbf{x},\mathbf{x}_u)$. Here, $\mathbf{x}_u$ is located at the upper boundary $\partial\mathcal{V}_u$ and $G^{\pm}_{tar}(\mathbf{x},\mathbf{x}_u)$ is stimulated by an impulsive point source
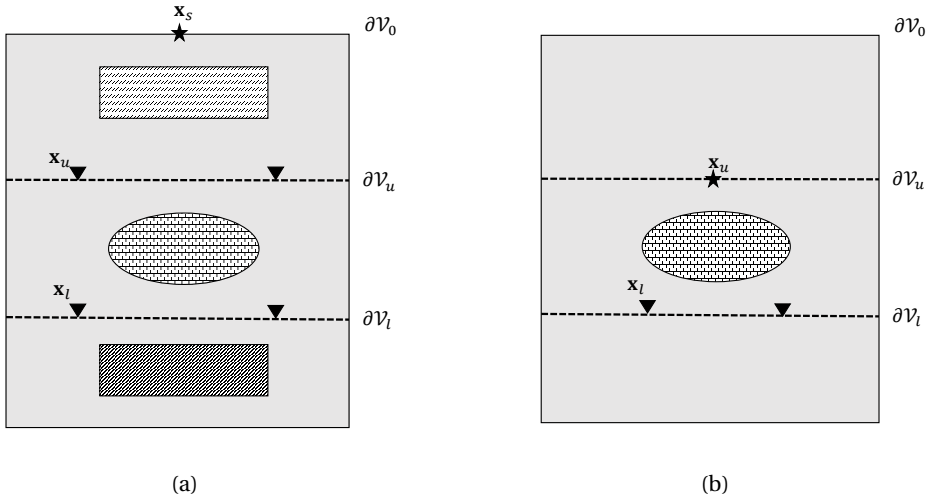
Figure 3.1.: (a) State A and (b) state B. Black stars depict source locations, and black reversed triangles depict receiver locations.

at $\mathbf{x}_u$. Since the half-space above the target is homogeneous in state B, the vertical derivative of the $G_{tar}^+(\mathbf{x}, \mathbf{x}_u)$ at $\partial\mathcal{V}_u$ is

$$\lim_{x_{u,3} \to x_{u,3^+}} \partial_3 G_{tar}^+(\mathbf{x}, \mathbf{x}_u) = -\frac{\rho}{2}\delta(\mathbf{x}_H - \mathbf{x}_{u,H}). \tag{3.7}$$

Here, $x_{u,3} \to x_{u,3^+}$ means the limit from below the boundary, where $\mathbf{x}_H$ and $\mathbf{x}_{u,H}$ denote the horizontal coordinates of $\mathbf{x}$ and $\mathbf{x}_u$, respectively. In addition, since in state B the medium below the target is reflection-free, $G_{tar}^-(\mathbf{x}, \mathbf{x}_u)$ and its derivative disappear at the lower boundary $\partial\mathcal{V}_l$. By substituting all of the ingredients into equation 3.5, the following can be reached:

$$G^-(\mathbf{x}_u, \mathbf{x}_s) = \int_{\partial\mathcal{V}_u} G^+(\mathbf{x}, \mathbf{x}_s)\frac{2\partial_3}{\rho(\mathbf{x})}G_{tar}^-(\mathbf{x}, \mathbf{x}_u)d\mathbf{x} + \int_{\partial\mathcal{V}_l} G^-(\mathbf{x}, \mathbf{x}_s)\frac{2\partial_3}{-\rho(\mathbf{x})}G_{tar}^+(\mathbf{x}, \mathbf{x}_u)d\mathbf{x}. \tag{3.8}$$

This equation is the base for our target-enclosed LSRTM derivation. The first integral on the right-hand side of Equation 3.8 accounts for anything entering the medium from the upper boundary, and the second integral accounts for anything that comes from the lower boundary.

3.2.3. TARGET-ENCLOSED LSRTM

To merge this representation with LSRTM, we use

$$\int_{\partial\mathcal{V}} p_A^{\pm}(\mathbf{x})\partial_3 p_B^{\mp}(\mathbf{x})d\mathbf{x} = -\int_{\partial\mathcal{V}} p_B^{\mp}(\mathbf{x})\partial_3 p_A^{\pm}(\mathbf{x})d\mathbf{x} \tag{3.9}$$

[36], and we use Green's function reciprocity:

$$G^-_{tar}(\mathbf{x}'_u, \mathbf{x}_u) = G^-_{tar}(\mathbf{x}_u, \mathbf{x}'_u) \tag{3.10}$$

$$G^+_{tar}(\mathbf{x}_l, \mathbf{x}_u) = G^-_{tar}(\mathbf{x}_u, \mathbf{x}_l), \tag{3.11}$$

where $\mathbf{x}'_u$ is an element of $\partial \mathcal{V}_u$ and $\mathbf{x}_l$ is an element of $\partial \mathcal{V}_l$. We rewrite Equation 3.8 as follows:

$$G^-(\mathbf{x}_u, \mathbf{x}_s) W(\omega) = \int_{\partial \mathcal{V}_u} G^-_{tar}(\mathbf{x}_u, \mathbf{x}'_u) S_u(\mathbf{x}'_u, \mathbf{x}_s) d\mathbf{x}'_u + \int_{\partial \mathcal{V}_l} G^-_{tar}(\mathbf{x}_u, \mathbf{x}_l) S_l(\mathbf{x}_l, \mathbf{x}_s) d\mathbf{x}_l, \tag{3.12}$$

where $W(\omega)$ is the source signature,

$$S_u(\mathbf{x}'_u, \mathbf{x}_s) = \frac{2\partial'_{3,u}}{-\rho(\mathbf{x}'_u)} G^+(\mathbf{x}'_u, \mathbf{x}_s) W(\omega) \tag{3.13}$$

is the dipole source from the upper boundary of the target, which accounts for reflections from above the upper boundary of the target. Further

$$S_l(\mathbf{x}_l, \mathbf{x}_s) = \frac{2\partial_{3,l}}{\rho(\mathbf{x}_l)} G^-(\mathbf{x}_l, \mathbf{x}_s) W(\omega) \tag{3.14}$$

is the dipole source term from the lower boundary of the target, which accounts for the reflections generated below the target. Fig. 3.2 represents the right-hand side of Equation 3.12.

As said above, the second integral on the right-hand side of equation 3.12 is the contribution of the medium below the target to the data. This integral can be split into two terms: 1) the arrival from the lower boundary to the upper one in the background, and 2) the forward scatterings inside the target region. In mathematical terms:

$$\int_{\partial \mathcal{V}_l} G^-_{tar}(\mathbf{x}_u, \mathbf{x}_l) S_l(\mathbf{x}_l, \mathbf{x}_s) d\mathbf{x}_l = \int_{\partial \mathcal{V}_l} G^-_{0,tar}(\mathbf{x}_u, \mathbf{x}_l) S_l(\mathbf{x}_l, \mathbf{x}_s) d\mathbf{x}_l$$
$$+ \int_{\partial \mathcal{V}_l} G^{-,scat}_{tar}(\mathbf{x}_u, \mathbf{x}_l) S_l(\mathbf{x}_l, \mathbf{x}_s) d\mathbf{x}_l. \tag{3.15}$$

Here, $G^-_{0,tar}(\mathbf{x}_u, \mathbf{x}_l)$ is the Green's function in the background model of the target, and $G^{-,scat}_{tar}(\mathbf{x}_u, \mathbf{x}_l)$ is the Green's function that contains the scattered events. By substituting equation 3.15 in equation 3.12 and taking the background contribution to the left-hand side we end up with:

$$G^-(\mathbf{x}_u, \mathbf{x}_s) W(\omega) - \int_{\partial \mathcal{V}_l} G^-_{0,tar}(\mathbf{x}_u, \mathbf{x}_l) S_l(\mathbf{x}_l, \mathbf{x}_s) d\mathbf{x}_l = \int_{\partial \mathcal{V}_u} G^{-,scat}_{tar}(\mathbf{x}_u, \mathbf{x}'_u) S_u(\mathbf{x}'_u, \mathbf{x}_s) d\mathbf{x}'_u$$
$$+ \int_{\partial \mathcal{V}_l} G^{-,scat}_{tar}(\mathbf{x}_u, \mathbf{x}_l) S_l(\mathbf{x}_l, \mathbf{x}_s) d\mathbf{x}_l. \tag{3.16}$$

Importantly, the Green's function $G^-_{tar}(\mathbf{x}_u, \mathbf{x}'_u)$ in the first integral on the right-hand side of equation 3.12 is the scattered Green's function inside the target, so we rename
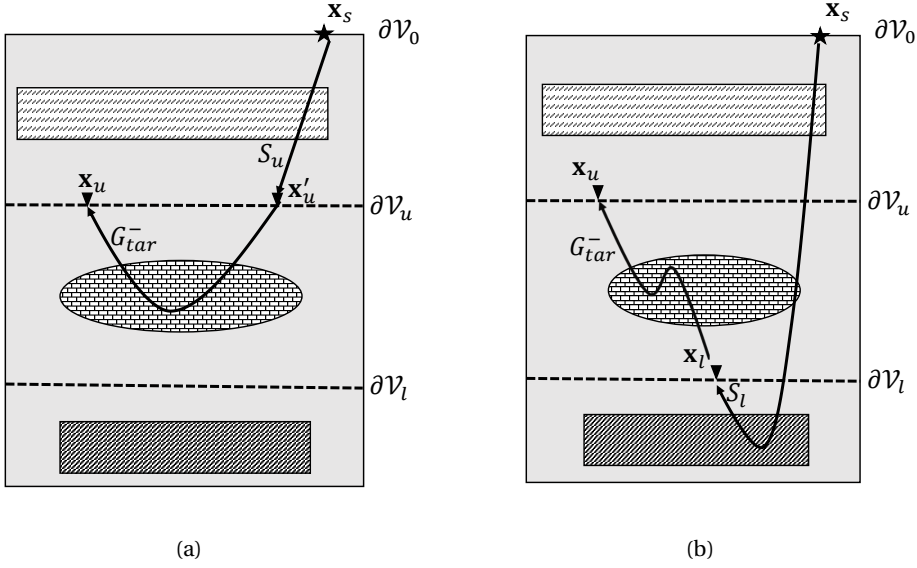
Figure 3.2.: (a) The first integral on the right-hand side of Equation 3.12, and (b) the second integral on the right-hand side of Equation 3.12.

it to $G_{tar}^{-,scat}(\mathbf{x}_u, \mathbf{x}_u')$.

To obtain our target-enclosed LSRTM algorithm, we take three steps: First, we assign

$$P_{obs}^{scat,TE}(\mathbf{x}_u, \mathbf{x}_s) = G^-(\mathbf{x}_u, \mathbf{x}_s)W(\omega) - \int_{\partial V_l} G_{0,tar}^-(\mathbf{x}_u, \mathbf{x}_l)S_l(\mathbf{x}_l, \mathbf{x}_s)d\mathbf{x}_l, \qquad (3.17)$$

where "TE" stands for "Target-Enclosed". Second we compute the scattered Green's functions $(G_{tar}^{-,scat}(\mathbf{x}_u, \mathbf{x}_u')$ and $G_{tar}^{-,scat}(\mathbf{x}_u, \mathbf{x}_l))$ with equation 3.1

$$G_{tar}^{-,scat}(\mathbf{x}_u, \mathbf{x}_u') = \int_V \gamma_0^2(\mathbf{x})G_{0,tar}(\mathbf{x}_u, \mathbf{x})\chi^c(\mathbf{x})G_{0,tar}(\mathbf{x}, \mathbf{x}_u')d\mathbf{x}, \qquad (3.18)$$

and

$$G_{tar}^{-,scat}(\mathbf{x}_u, \mathbf{x}_l) = \int_V \gamma_0^2(\mathbf{x})G_{0,tar}(\mathbf{x}_u, \mathbf{x})\chi^c(\mathbf{x})G_{0,tar}(\mathbf{x}, \mathbf{x}_l)d\mathbf{x}, \qquad (3.19)$$

where $\mathbf{x}$ is a location inside the target volume. Using this in the right-hand side of Equation 3.16, we obtain

$$\int_{\partial V_u} G_{tar}^{-,scat}(\mathbf{x}_u, \mathbf{x}_u')S_u(\mathbf{x}_u', \mathbf{x}_s)d\mathbf{x}_u' + \int_{\partial V_l} G_{tar}^{-,scat}(\mathbf{x}_u, \mathbf{x}_l)S_l(\mathbf{x}_l, \mathbf{x}_s)d\mathbf{x}_l =$$
$$\int_V \gamma_0^2(\mathbf{x})G_{tar}^{-,scat}(\mathbf{x}_u, \mathbf{x})\chi^c(\mathbf{x})P^{inc,TE}(\mathbf{x}, \mathbf{x}_s)d\mathbf{x}, \quad (3.20)$$

where

$$P^{inc,TE}(\mathbf{x},\mathbf{x}_s) = \int_{\partial V_u} G^-_{0,tar}(\mathbf{x},\mathbf{x}'_u) S_u(\mathbf{x}'_u,\mathbf{x}_s) d\mathbf{x}'_u + \int_{\partial V_l} G^-_{0,tar}(\mathbf{x},\mathbf{x}_l) S_l(\mathbf{x}_l,\mathbf{x}_s) d\mathbf{x}_l. \qquad (3.21)$$

Finally, we complete our derivation by assigning

$$P^{scat,TE}_{pred}(\mathbf{x}_u,\mathbf{x}_s) = \int_V \gamma_0^2(\mathbf{x}) G_{0,tar}(\mathbf{x}_u,\mathbf{x}) \chi^c(\mathbf{x}) P^{inc,TE}(\mathbf{x},\mathbf{x}_s) d\mathbf{x}. \qquad (3.22)$$

Our approach computes an incident wavefield, which contains all of the information from the surrounding medium of the target of interest. This means our approach is not limited to one kind of parametrization, and it can be implemented for any parametrization choice. Further, It is also possible to inject S_u and S_l as dipole sources using a finite-difference algorithm instead of solving Equations 3.21 and 3.22. Finally, we can solve the following least-squares problem, i.e., minimizing the objective function:

$$J(\delta\mathbf{m}) = \frac{1}{2}\|\mathbf{P}^{scat,TE}_{pred}(\delta\mathbf{m}) - \mathbf{P}^{scat,TE}_{obs}\|_2^2. \qquad (3.23)$$

3.2.4. MARCHENKO GREEN'S FUNCTION RETRIEVAL

We obtained a target-enclosed LSRTM algorithm in the previous section. Nevertheless, in most real-world situations, one does not have physical access to the boundaries of the region of interest. The alternative to physical receivers inside the medium is to create virtual receivers with redatuming. Marchenko redatuming is a state-of-the-art data-driven approach that can compute Green's functions at any depth level with all orders of multiple reflections from the reflection response at the surface and a smooth background model of the medium.

To summarise, these redatumed Green's functions are retrieved by iteratively solving the Marchenko-type representations. These representations are [22]

$$G^-_{Mar}(\mathbf{x}_v,\mathbf{x}_s) = \int_{\partial V_0} R(\mathbf{x}_s,\mathbf{x}'_s) f_1^+(\mathbf{x}'_s,\mathbf{x}_v) d\mathbf{x}'_s - f_1^-(\mathbf{x}_s,\mathbf{x}_v), \qquad (3.24)$$

and

$$G^+_{Mar}(\mathbf{x}_v,\mathbf{x}_s) = -\int_{\partial V_0} R(\mathbf{x}_s,\mathbf{x}'_s) f_1^-(\mathbf{x}'_s,\mathbf{x}_v)^* d\mathbf{x}'_s + f_1^+(\mathbf{x}_s,\mathbf{x}_v)^*. \qquad (3.25)$$

Here, ∂V_0 is the surface, $\mathbf{x}_s$ and $\mathbf{x}'_s$ are locations at the surface, and $\mathbf{x}_v$ is a virtual location on an arbitrary depth. Moreover, $f_1^\pm$ are upgoing (-) and downgoing (+) parts of the focusing function. In addition, $R(\mathbf{x}_s,\mathbf{x}'_s)$ is the reflection response at the surface which is related to the upgoing Green's function of the medium via

$$R(\mathbf{x}_s,\mathbf{x}'_s) = \frac{2\partial'_{3,s}}{-\rho(\mathbf{x}'_s)} G^-(\mathbf{x}_s,\mathbf{x}'_s). \qquad (3.26)$$

Here, $\partial'_{3,s}$ is the vertical partial derivative at $\mathbf{x}'_s$. We refer to [37] for a comprehensive explanation of the derivation and numerical algorithms for solving these equations.

Consequently, we can substitute Marchenko Green's functions with the target boundaries Green's functions as follows:

$$G^+(\mathbf{x}_u, \mathbf{x}_s) \approx G^+_{Mar}(\mathbf{x}_u, \mathbf{x}_s), \tag{3.27}$$

$$G^-(\mathbf{x}_u, \mathbf{x}_s) \approx G^-_{Mar}(\mathbf{x}_u, \mathbf{x}_s), \tag{3.28}$$

and

$$G^-(\mathbf{x}_l, \mathbf{x}_s) \approx G^-_{Mar}(\mathbf{x}_l, \mathbf{x}_s). \tag{3.29}$$

Equations 3.27 and 3.29 can be used in equations 3.13 and 3.14 to obtain the source terms S_u and S_l, whereas equation 3.28 can be used in equation 3.17 to obtain the observed target-oriented scattered response.

3.3. NUMERICAL RESULTS

3.3.1. SINGLE-SIDED ALGORITHM VS. DOUBLE-SIDED ALGORITHM

In this section, we aim to visualize the performance of target-enclosed LSRTM. Here we use direct modeling of the Green's functions with receivers inside the medium; in section B we use the Marchenko method to retrieve these Green's functions from the reflection response at the surface. A model with dimensions of 1000 m by 650 m is designed as shown in Fig. 3.3. The spatial grid sampling is 5 m in both directions. The target region consists of a rectangular velocity anomaly embedded in a homogeneous background and a constant density. A total of 201 sources are placed at the surface, and 402 receivers are on the target's upper (250 m) and lower (550 m) boundaries. The required Green's functions and wavefields are computed by a finite-difference algorithm [38] and a Ricker wavelet with a dominant frequency of 30 Hz, where the recording time sampling of the receivers is set to 4 ms. According to the theory section, the wavefields at the receiver positions are decomposed into upgoing and downgoing components. Fig. 3.4 shows the upgoing component of the data at the upper boundary with a source located at $\mathbf{x}_s = (0,0)$, corresponding to the first term on the right-hand side of Equation 3.17. We study the effects of including the lower boundary with two different cases: 1) a homogeneous background velocity and 2) a smooth background velocity for migration.

HOMOGENEOUS BACKGROUND VELOCITY

In this section, we show the results using a homogeneous background velocity in the target area. The true perturbation model of this case is shown in Fig. 3.5. We design two scenarios to demonstrate the performance and consequences of the target-enclosed algorithm. For the first scenario, we only consider the upper boundary of the target in the inversion process and completely ignore the lower boundary contribution. We call this scenario "single-sided algorithm." For this
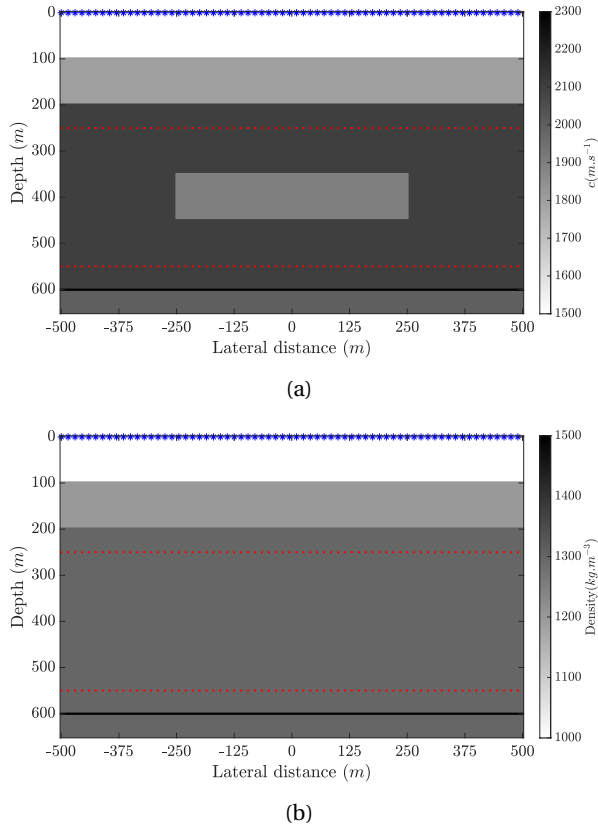
(a)

(b)

Figure 3.3.: (a) Velocity model and (b) density model. The blue stars at the surface are source locations, and the red dots are the boundaries of the target.

scenario, the observed data is the same as Fig. 3.4. For the second one, we include the lower boundary contribution, which is the "double-sided algorithm" explained in the previous section. The observed data for this scenario is shown in Fig. 3.6a, which corresponds to the left-hand side of Equation 3.17, whereas Fig. 3.4 shows $G^-(\mathbf{x}_u, \mathbf{x}_s)W(\omega)$. The black arrows in Figures 3.4 and 3.6a indicate the full reflection from the reflector below the lower boundary and the forward scattered part of it, respectively. Figures 3.6b and 3.6c show the predicted data of single-sided and double-sided algorithms, respectively, after 30 iterations of LSRTM. A detailed investigation of Fig. 3.6 proves that the double-sided algorithm can predict the forward scattered event that is passing through the perturbation, which is indicated by a black arrow in Fig. 3.6c.

To move our investigation further, we show the imaging results of both algorithms in Fig. 3.7. Figures 3.7a and 3.7b show the RTM images of both approaches. As we can see, the RTM result of the double-sided algorithm faintly reveals the long
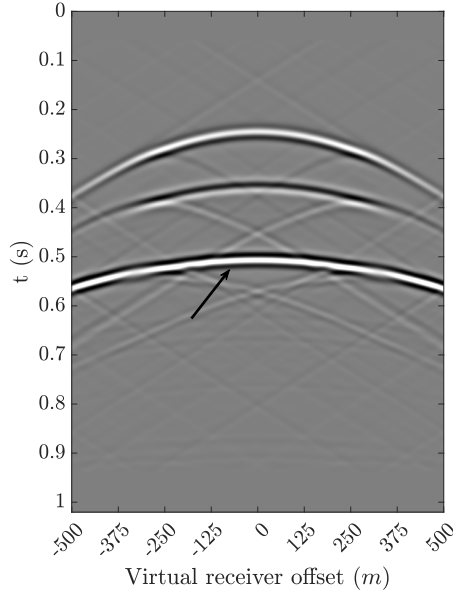
Figure 3.4.: Upgoing component of data at the upper boundary with a source located at $\mathbf{x}_s = (0,0)$. This is the data corresponding to the first term on the right-hand side of Equation 3.17. The black arrow indicates the total event generated by the reflector below the target region described by the left-hand side of Equation 3.15.
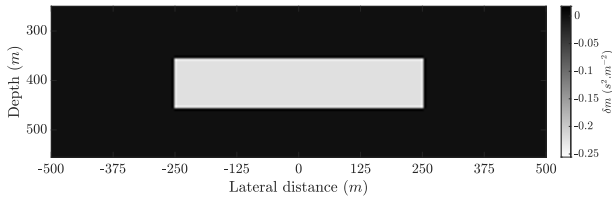

Figure 3.5.: True perturbation model in a homogeneous background.

wavelength part of the model. Moving to the LSRTM results in Figures 3.7c and 3.7d, we observe an interesting outcome. The LSRTM result of the single-sided algorithm shows that it cannot recover the long wavelength part of the model (Fig. 3.7c). In contrast, the double-sided algorithm can incorporate the information embedded inside the forward scattered field (Fig. 3.7d), and it recovers the long
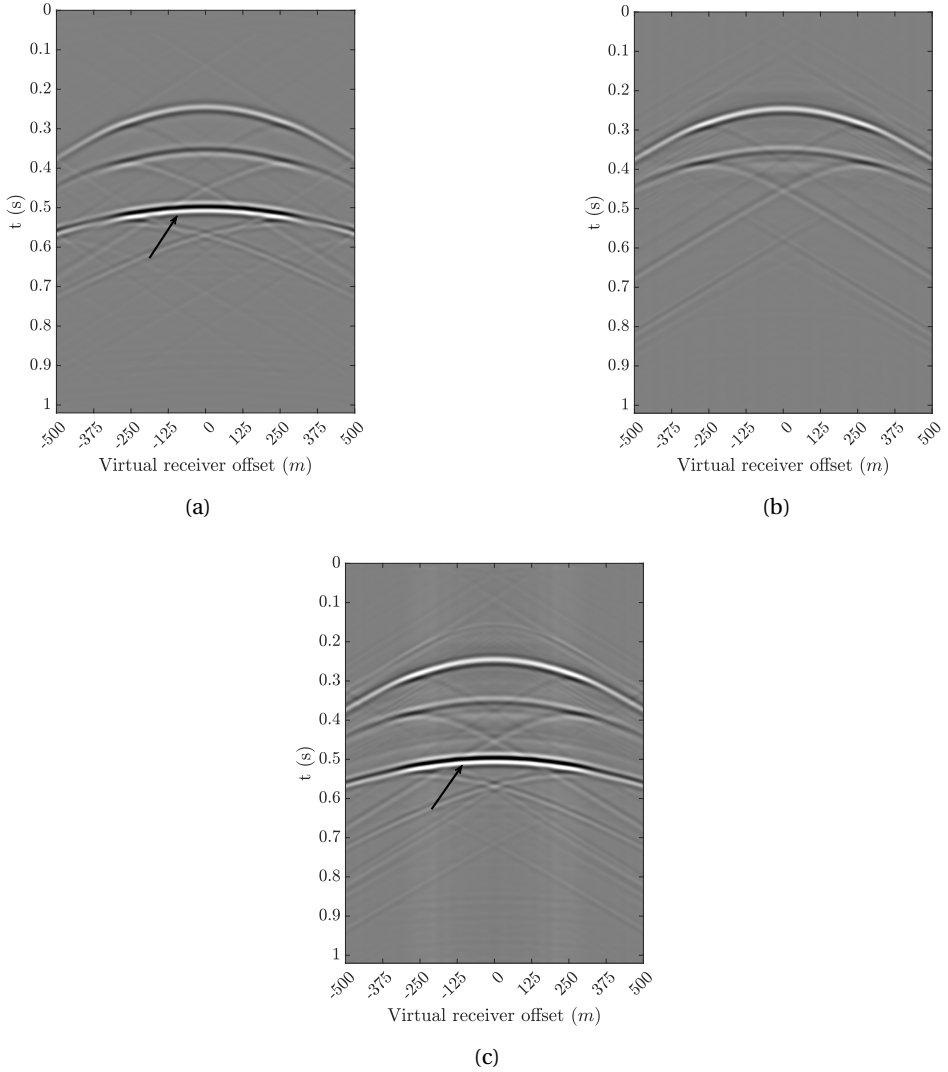
(a)

(b)

(c)

Figure 3.6.: Homogeneous background velocity case, data domain: (a) Upgoing component of double-sided observed data at the upper boundary (Equation 3.17), (b) predicted data of single-sided algorithm after 30 iterations of LSRTM, and (c) predicted data of double-sided algorithm after 30 iterations of LSRTM. All wavefields are recorded at the upper boundary of the target (250 m). The black arrow indicates the scattered event generated by the reflector below the target region described by the second term on the right-hand side of Equation 3.15.

wavelength parts of the volume perturbation. Moreover, Fig. 3.8 shows the horizontal cross-section of the retrieved perturbation. In this figure, we can see the double-sided approach can recover the vertical boundaries of the perturbation. Nevertheless, since the background velocity for the migration is not updated during LSRTM, the fit of the reflected event from below the target is not accurate.
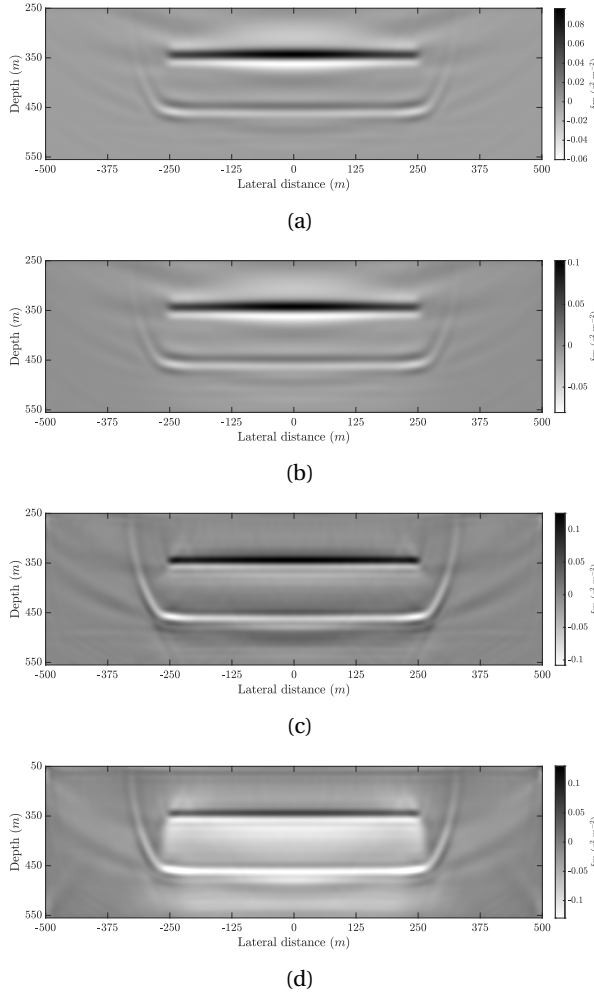

(a)

(b)

(c)

(d)

Figure 3.7.: Homogeneous background velocity case, image domain: (a) RTM image of the single-sided algorithm, (b) RTM image of the double-sided algorithm, (c) LSRTM image of the single-sided algorithm after 30 iterations, and (d) LSRTM image of the double-sided algorithm after 30 iterations.

To conclude this section, we compare the cost functions of both approaches in
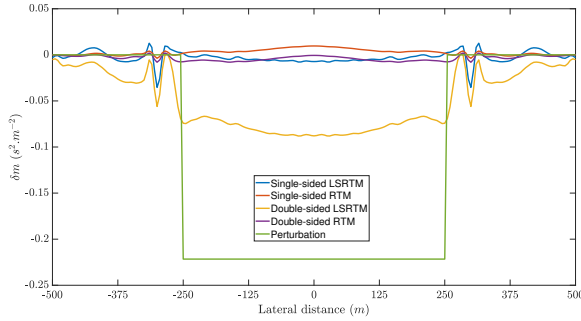
Figure 3.8.: Horizontal cross-section at the depth of 400 m of the retrieved perturbation with a homogeneous migration velocity.

Fig. 3.9. The cost function of target-oriented LSRTM shows a slow convergence rate. In comparison, the target-enclosed approach includes the extra information coming from the lower boundary, so its cost function converges faster and to a lower minimum.
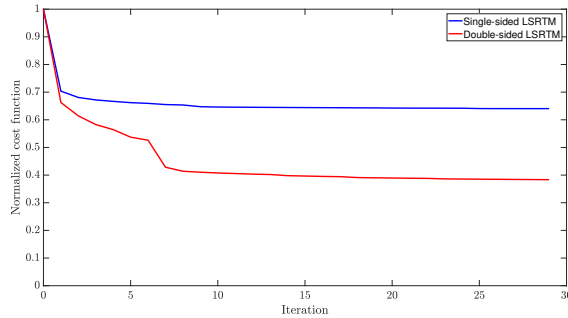

Figure 3.9.: Cost function comparison of homogeneous background velocity case.

SMOOTH BACKGROUND VELOCITY

This section uses a smooth background velocity for migration. The setup is exactly the same as before, except for the background velocity. The perturbation model for this case is shown in Fig. 3.10. Again, we do the same two scenarios as before, i.e., "single-sided" and "double-sided." For the single-sided scenario, the observed data is the same as before (Fig. 3.4). However, since the right-hand side of the equation 3.17 is computed in a different background velocity, the last primary in the observed data for the double-sided approach (Fig. 3.11a) is slightly different.

Comparing the results of both approaches shows (Fig. 3.11) that the double-sided approach (Fig. 3.11c) can predict the reflected event coming from the lower boundary. Since we use a smooth background velocity here, this prediction is more
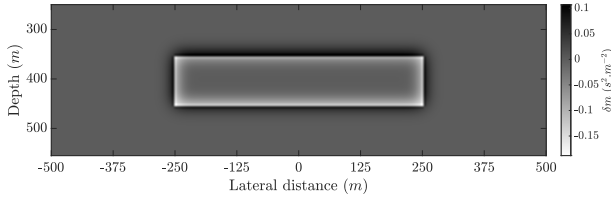
Figure 3.10.: True perturbation model in a smooth background.

accurate than the previous section's results (Fig. 3.6c). In the image domain (Fig. 3.12), the double-sided approach recovers a faint image of the vertical sides of the rectangular perturbation (Fig. 3.12d) whereas the single-sided results in a more standard image (Fig. 3.12c). Moreover, Fig. 3.13 shows the horizontal cross-section of the retrieved perturbation. In this figure, we can see the double-sided approach can recover the vertical boundaries of the perturbation. The double-sided image is more comparable to the true perturbation in Fig. 3.10. Finally, investigating the cost functions (Fig. 3.14) of these approaches shows that the double-sided approach converges better since it can predict the event coming from below the target.

3.3.2. VIRTUAL RECEIVERS

Here, we use the same setup as before but replace the Green's functions at the boundaries with their Marchenko counterparts. In other words, we create virtual receivers with the help of Marchenko redatuming. For a study about the benefits of using Marchenko redatuming instead of a more conventional redatuming algorithm for target-oriented LSRTM we refer to [27]. In this section, we only focus on including the lower boundary by utilizing virtual receivers created by Marchenko redatuming, and instead of using "double-sided", we use the "target-enclosed" term. Moreover, we show the results for both homogeneous and smooth background velocities in this section.

HOMOGENEOUS BACKGROUND VELOCITY

Fig. 3.15 shows the data obtained by Marchenko redatuming. In Fig. 3.16 the observed data calculated by Equation 3.17 (Fig. 3.16a) and the predicted data after 30 iterations (Fig. 3.16b) are shown. A comparison between Fig. 3.16b and Fig. 3.6c shows that even in the presence of redatuming error, such as limited aperture and lack of certain parts of the wavelength spectrum, our algorithm can predict acceptable data.

In the image domain, Fig. 3.17 shows the RTM (Fig. 3.17a) and LSRTM (Fig. 3.17b) image resulting from Marchenko redatumed data. Comparing Fig. 3.17b with Fig.

(a)

(b)

(c)
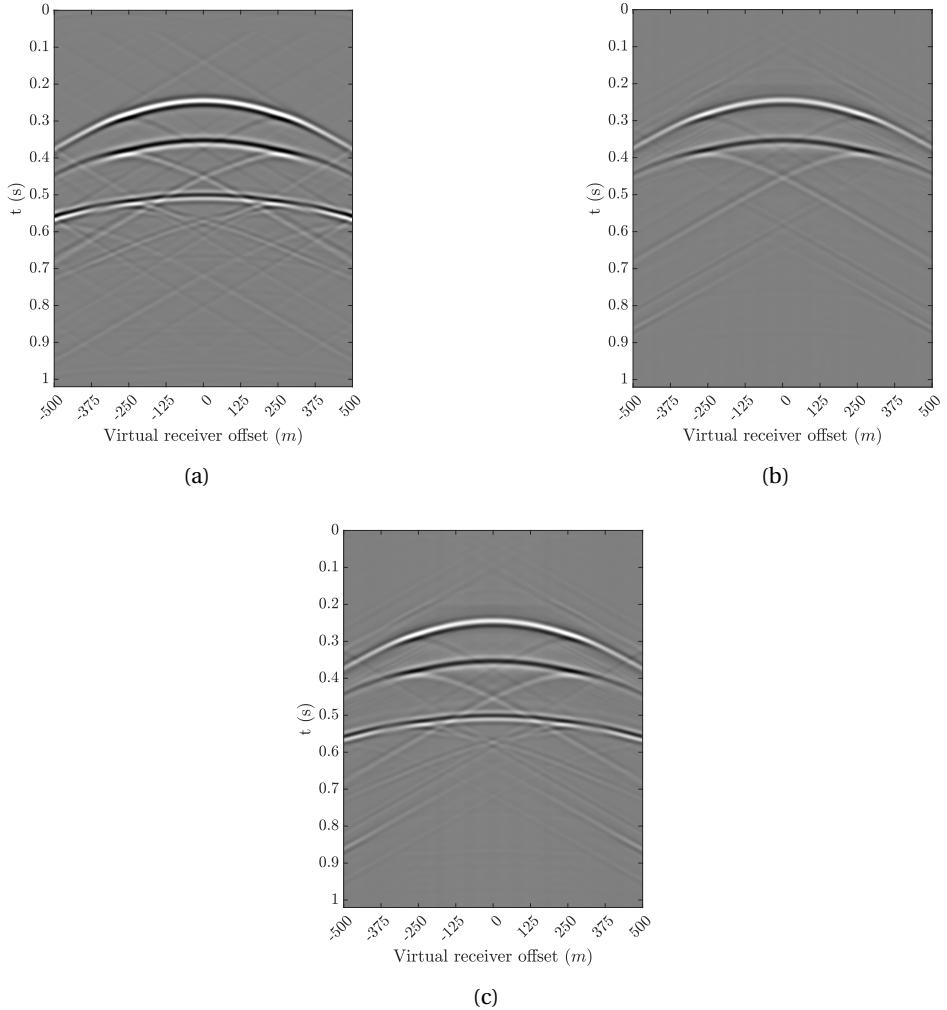
Figure 3.11.: Smooth background velocity case, data domain: (a) Upgoing component of double-sided observed data at the upper boundary (Equation 3.17), (b) predicted data of single-sided algorithm after 30 iterations of LSRTM, and (c) predicted data of double-sided algorithm after 30 iterations of LSRTM. All wavefields are recorded at the upper boundary of the target (250 *m*).

3.7d reveals our target-enclosed algorithm with redatumed data as input can not recover the long wavelength part of the model. This is due to the fact that the direct arrival of the Marchenko-based Green's function is incorrect since it is computed in the background model. Consequently, the forward-scattered waveforms responsible

(a)

(b)

(c)

(d)
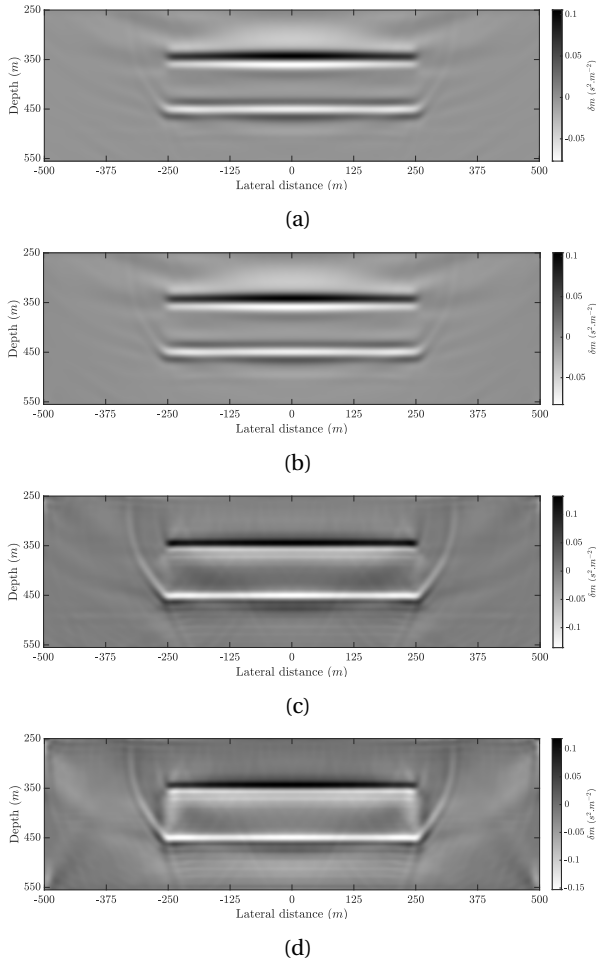
Figure 3.12.: Smooth background velocity case, image domain: (a) RTM image of the single-sided algorithm, (b) RTM image of the double-sided algorithm, (c) LSRTM image of the single-sided algorithm after 30 iterations, and (d) LSRTM image of the double-sided algorithm after 30 iterations.

for the long wavelength updates in Figure 7d can no longer be utilized.

SMOOTH BACKGROUND VELOCITY

In Fig. 3.18 the observed data calculated by Equation 3.17 (Fig. 3.18a) and the predicted data after 30 iterations (Fig. 3.18b) are shown. Similar to the homogeneous case, a comparison between Fig. 3.18 and Fig. 3.11 shows that our algorithm successfully predicts the data.

In the image domain, Fig. 3.19 shows the RTM (Fig. 3.19a) and LSRTM (Fig.

Figure 3.13.: Horizontal cross-section at the depth of 400 m of the retrieved perturbation with a smooth migration velocity.
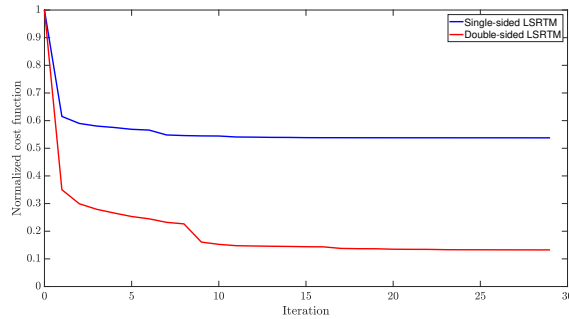
Figure 3.14.: Cost function comparison of smooth background velocity case.

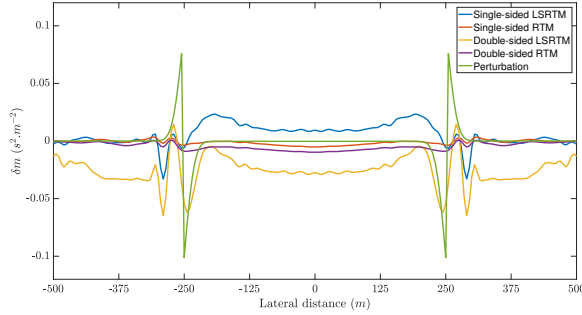3.19b) image resulting from Marchenko redatumed data. Comparing Fig. 3.19b with Fig. 3.12d shows that redatumed data reveals an acceptable perturbation model. However, the faint recovered vertical interfaces are not presented in Fig. 3.19b since forward-scattered waveforms are not processed correctly in the retrieved Marchenko Green's function at the lower boundary.

LSRTM RESULTS FOR THE ENTIRE MEDIUM

To make a fair comparison, we include the results of standard LSRTM for the entire medium with the smooth background model in this section. Figure 3.20 shows the LSRTM image after 30 iterations. Figure 3.20a shows the image of the entire medium and Figure 3.20b singled out the target area of it.

3.4. DISCUSSION

In Section 3.2, we develop a theory for target-enclosed LSRTM that can limit the computation domain by confining the target between two boundaries. Equations
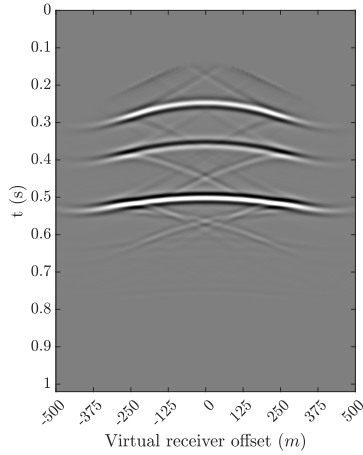
Figure 3.15.: Marchenko redatumed data with virtual receivers at the upper boundary (250 m) and a source located at $\mathbf{x}_s = (0,0)$.

(a)   (b)

Figure 3.16.: Homogeneous background velocity case with virtual receivers, data domain: (a) Upgoing component of Marchenko redatumed data at the upper boundary (Equation 3.17), (b) predicted data of target-enclosed LSRTM after 30 iterations at the upper boundary. All wavefields are redatumed to the upper boundary of the target (250 m).

3.17 and 3.22 enable us to account for any wavefield entering the target region by including the upper and lower boundaries in the inversion process.

(a)

(b)
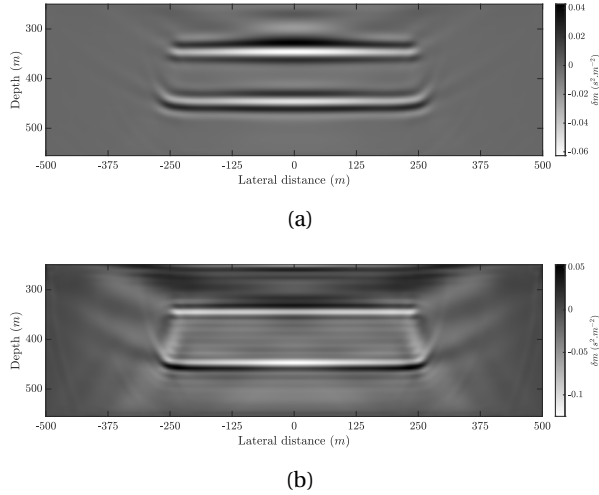
Figure 3.17.: Homogeneous background velocity case with virtual receivers, image
domain: (a) RTM image of the target-enclosed algorithm with Marchenko
wavefields, (b) LSRTM image of the target-enclosed algorithm with
Marchenko wavefields after 30 iterations.

Further, in section 3.3.1, several numerical tests are designed to demonstrate the
advantage of incorporating the lower boundary in the conventional target-oriented
LSRTM. From the data point of view, our double-sided target-enclosed LSRTM,
compared to a conventional single-sided target-oriented LSRTM, not only removes
the background arrival from the lower boundary to the upper boundary but also can
predict the forward scattered field inside the target (Fig. 3.6, Fig. 3.11, and Fig. 3.16).
Additionally, a comparison between the resulting images of both algorithms with a
homogeneous migration velocity (Fig. 3.7), shows that single-sided target-oriented
LSRTM can not update the long wavelength part of the model. In contrast,
the double-sided target-enclosed LSRTM updates the image according to the Born
inversion criteria by integrating the forward scattered wavefield information. In
the case of a smooth migration velocity, our algorithm recovers a higher-resolution
image and a faint estimation of the vertical sides of the rectangular perturbation
(Fig. 3.12).

Moreover, in section 3.3.2, we investigate the possibility of using virtual receivers
created by Marchenko redatuming in our target-enclosed algorithm. Fig. 3.17 shows
that in the case of a homogeneous background migration velocity, it is hardly
possible to update the long wavelengths with virtual receiver data, and only short
wavelength parts of the perturbation are recovered. Moreover, for the smooth
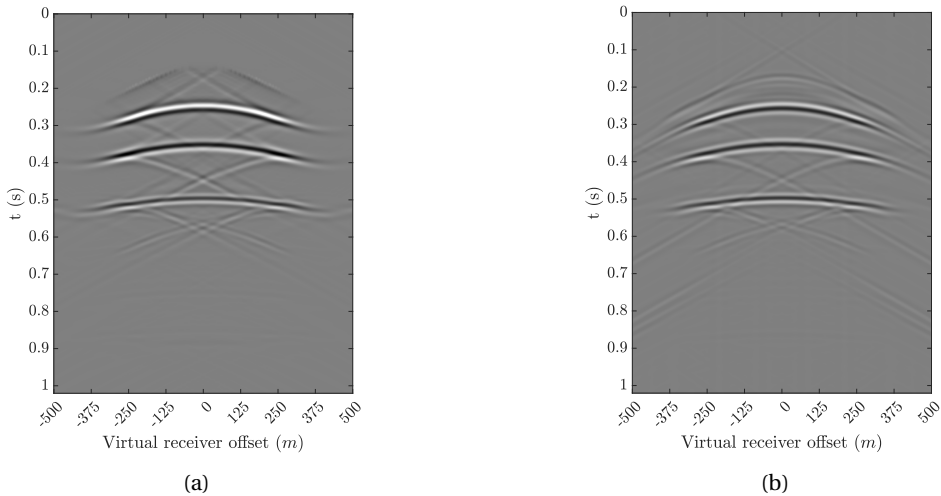background case, our algorithm increases the image's resolution by updating the
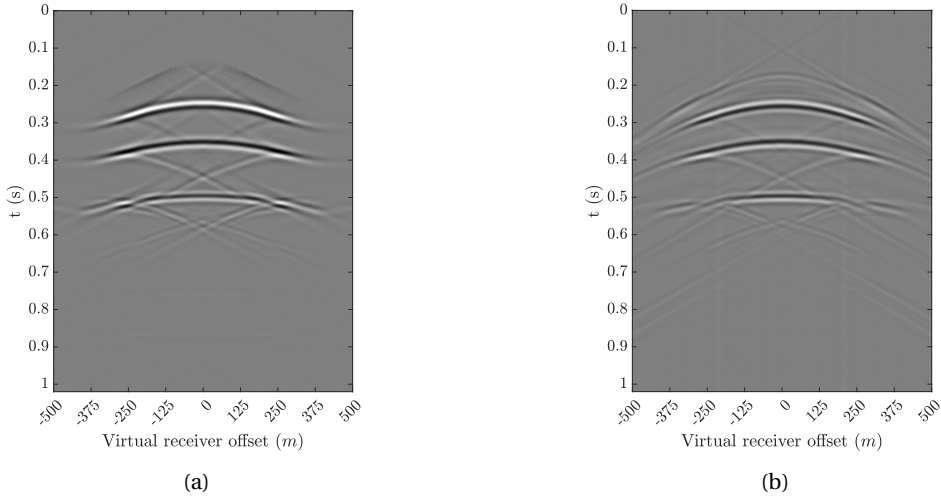
Figure 3.18.: Smooth background velocity case with virtual receivers, data domain: (a) Upgoing component of Marchenko redatumed data at the upper boundary (Equation 3.17), (b) predicted data of target-enclosed LSRTM after 30 iterations at the upper boundary. All wavefields are redatumed to the upper boundary of the target (250 m).

short wavelengths in this case.

Ultimately, we show the standard LSRTM image for the entire medium. Comparing Figure 3.20 with previous cases shows that our method is superior in imaging the target area in any case. Our method adds valuable information by explicitly incorporating transmitted wavefields. Further, with our setup and hardware, the computational time of a single iteration of LSRTM for the entire medium, which has 201 by 131 grid points, is about 45 seconds, and a single iteration of target-enclosed LSRTM, which has 201 by 61 grid points, is about 25 seconds. We do not consider the computational cost of the Marchenko redatuming method here since we only do it once and compared to the total time of LSRTM it is negligible. One disadvantage we can mention is saving the extra redatumed wavefields and focusing functions on the disk. However, relative to the reduction of the memory need by the reduction of the target dimensions, this can be neglected.

3.5. CONCLUSION

This chapter proposes a target-enclosed seismic imaging algorithm that can account for the wavefields entering the target region from the upper and lower boundaries of the region. The three main advantages of this chapter's algorithm are 1) It significantly reduces the computational domain by limiting it to a smaller domain,
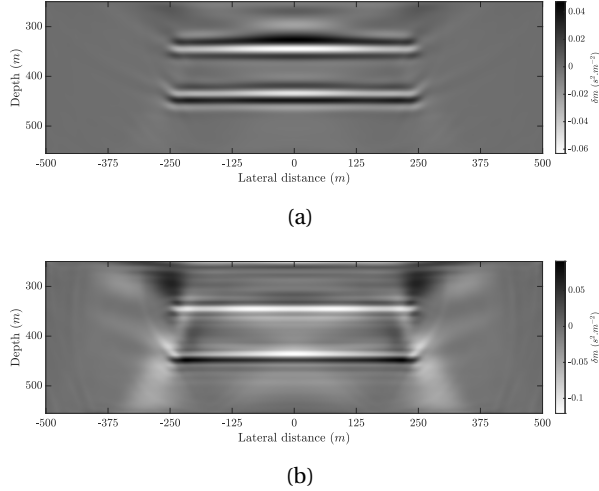
(a)

(b)

Figure 3.19.: Smooth background velocity case with virtual receivers, image domain: (a) RTM image of the target-enclosed algorithm with Marchenko wavefields, (b) LSRTM image of the target-enclosed algorithm with Marchenko wavefields after 30 iterations.

2) it removes interactions with the part of the medium above the upper boundary, and 3) it can incorporate the transmission information from the lower boundary to the upper one.

Nevertheless, our algorithm has also some limitations. First, we need access to the lower boundary of the target to deploy receivers at the boundaries of the target. Second, we need a background model of the target that can predict the arrival time from the lower boundary to the upper. It is possible to overcome the first limitation by using virtual seismology methods such as Marchenko redatuming to create virtual receivers around the target region [22, 25, 27, 39–43] as we showed in a numerical example in section 3.3.2. To address the second limitation, a reformulation of the target-enclosed LSRTM is possible to make it compatible with full waveform inversion to update the background velocity model [44].

The need for high-resolution images is increasing daily, which demands more computational power. This chapter's proposed target-enclosed LSRTM can produce less computationally demanding high-resolution images by focusing on a relatively small target of interest and including all the interactions between this region and the outside environment.
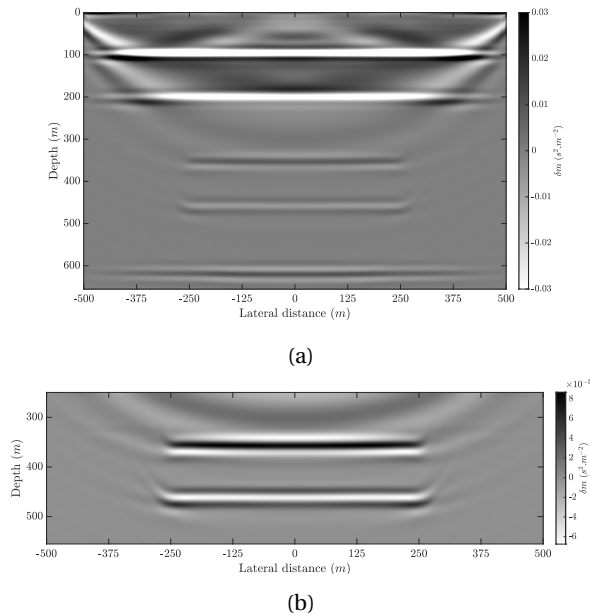
(a)

(b)

Figure 3.20.: Standard LSRTM with smooth background velocity for entire medium, image domain: (a) LSRTM image of the entire medium, (b) magnified target area of (a).

REFERENCES

[1]   A. Shoja, J. van der Neut and K. Wapenaar. 'Target-Enclosed Least-Squares Seismic Imaging'. In: *IEEE Transactions on Geoscience and Remote Sensing* 61 (2023), pp. 1–12. DOI: 10.1109/TGRS.2023.3293725.

[2]   J. F. Claerbout. *Imaging the Earth's Interior*. BlackWell Scientific Publications, 1985.

[3]   W. A. Mulder and R.-E. Plessix. 'A comparison between oneway and twoway waveequation migration'. In: *GEOPHYSICS* 69.6 (2004), pp. 1491–1504. DOI: 10.1190/1.1836822.

[4]   E. Baysal, D. D. Kosloff and J. W. C. Sherwood. 'Reverse time migration'. In: *GEOPHYSICS* 48.11 (1983), pp. 1514–1524. DOI: 10.1190/1.1441434.

[5]   H.-W. Zhou, H. Hu, Z. Zou, Y. Wo and O. Youn. 'Reverse time migration: A prospect of seismic imaging methodology'. In: *Earth-Science Reviews* 179 (2018), pp. 207–227. DOI: https://doi.org/10.1016/j.earscirev.2018.02.008.

[6]   L. Zhang, E. Slob, J. van der Neut and K. Wapenaar. 'Artifact-free reverse time migration'. In: *GEOPHYSICS* 83.5 (2018), A65–A68. DOI: 10.1190/geo2017-0795.1.

[7]   G. T. Schuster. *SEISMIC INVERSION*. Society of Exploration Geophysicists, 2017.

[8]   G. Dutta, M. Giboli, C. Agut, P. Williamson and G. T. Schuster. 'Least-squares reverse time migration with local Radon-based preconditioning'. In: *GEOPHYSICS* 82.2 (2017), S75–S84. DOI: 10.1190/geo2016-0117.1.

[9]   Y. Tang. 'Target-oriented wave-equation least-squares migration/inversion with phase-encoded Hessian'. In: *GEOPHYSICS* 74.6 (2009), WCA95–WCA107. DOI: 10.1190/1.3204768.

[10]   Y. Liu, X. Liu, A. Osen, Y. Shao, H. Hu and Y. Zheng. 'Least-squares reverse time migration using controlled-order multiple reflections'. In: *GEOPHYSICS* 81.5 (2016), S347–S357. DOI: 10.1190/geo2015-0479.1.

[11]   W. Dai, P. Fowler and G. T. Schuster. 'Multi-source least-squares reverse time migration'. In: *Geophysical Prospecting* 60.4 (2012), pp. 681–695. DOI: https://doi.org/10.1111/j.1365-2478.2012.01092.x.

[12]   F. J. Herrmann and X. Li. 'Efficient least-squares imaging with sparsity promotion and compressive sensing'. In: *Geophysical Prospecting* 60.4 (2012), pp. 696–712. DOI: https://doi.org/10.1111/j.1365-2478.2011.01041.x.

[13]   M. Farshad and H. Chauris. 'Sparsity-promoting multiparameter pseudoinverse Born inversion in acoustic media'. In: *GEOPHYSICS* 86.3 (2021), S205–S220. DOI: 10.1190/geo2020-0527.1.

[14]   A. A. Valenciano, B. Biondi and A. Guitton. 'Target-oriented wave-equation inversion'. In: *GEOPHYSICS* 71.4 (2006), A35–A38. DOI: 10.1190/1.2213359.

[15]   P. Haffinger, A. Gisolf and P. M. v. d. Berg. 'Towards high resolution quantitative subsurface models by full waveform inversion'. In: *Geophysical Journal International* 193.2 (Feb. 2013), pp. 788–797. ISSN: 0956-540X. DOI: 10.1093/gji/ggt021.

[16]   B. Willemsen, A. Malcolm and W. Lewis. 'A numerically exact local solver applied to salt boundary inversion in seismic full-waveform inversion'. In: *Geophysical Journal International* 204.3 (Feb. 2016), pp. 1703–1720. DOI: 10.1093/gji/ggv547.

[17]   S. Yuan, N. Fuji, S. Singh and D. Borisov. 'Localized time-lapse elastic waveform inversion using wavefield injection and extrapolation: 2-D parametric studies'. In: *Geophysical Journal International* 209.3 (Mar. 2017), pp. 1699–1717. DOI: 10.1093/gji/ggx118.

[18]   Z. Zhao and M. K. Sen. 'Fast image-domain target-oriented least-squares reverse time migration'. In: *GEOPHYSICS* 83.6 (2018), A81–A86. DOI: 10.1190/geo2018-0033.1.

[19]   Q. Guo and T. Alkhalifah. 'Target-oriented waveform redatuming and high-resolution inversion: Role of the overburden'. In: *GEOPHYSICS* 85.6 (2020), R525–R536. DOI: 10.1190/geo2019-0640.1.

[20]   M. Ravasi, I. Vasconcelos, A. Kritski, A. Curtis, C. A. d. C. Filho and G. A. Meles. 'Target-oriented Marchenko imaging of a North Sea field'. In: *Geophysical Journal International* 205.1 (Feb. 2016), pp. 99–104. DOI: 10.1093/gji/ggv528.

[21]   Q. Guo and T. Alkhalifah. 'Datum-based waveform inversion using a subsurface-scattering imaging condition'. In: *GEOPHYSICS* 84.4 (2019), S251–S266. DOI: 10.1190/geo2018-0615.1.

[22]   K. Wapenaar, J. Thorbecke, J. van der Neut, F. Broggini, E. Slob and R. Snieder. 'Marchenko imaging'. In: *GEOPHYSICS* 79.3 (2014), WA39–WA57. DOI: 10.1190/geo2013-0302.1.

[23]   D. Vargas, I. Vasconcelos, Y. Sripanich and M. Ravasi. 'Scattering-based focusing for imaging in highly complex media from band-limited, multicomponent data'. In: *GEOPHYSICS* 86.5 (2021), WC141–WC157. DOI: 10.1190/geo2020-0939.1.

[24]   G. T. Schuster and M. Zhou. 'A theoretical overview of model-based and correlation-based redatuming methods'. In: *GEOPHYSICS* 71.4 (2006), SI103–SI110. DOI: 10.1190/1.2208967.

[25]   M. Ravasi. 'Rayleigh-Marchenko redatuming for target-oriented, true-amplitude imaging'. In: *GEOPHYSICS* 82.6 (2017), S439–S452. DOI: 10.1190/geo2017-0262.1.

[26] N. Luiken and T. van Leeuwen. 'Seismic wavefield redatuming with regularized multi-dimensional deconvolution'. In: *Inverse Problems* 36.9 (Sept. 2020). DOI: 10.1088/1361-6420/aba9d1.

[27] A. Shoja, J. van der Neut and K. Wapenaar. 'Target-oriented least-squares reverse-time migration using Marchenko double-focusing: reducing the artefacts caused by overburden multiples'. In: *Geophysical Journal International* 233.1 (Apr. 2023), pp. 13–32. DOI: 10.1093/gji/ggac438.

[28] K. Wapenaar, J. Thorbecke and J. van der Neut. 'A single-sided homogeneous Green's function representation for holographic imaging, inverse scattering, time-reversal acoustics and interferometric Green's function retrieval'. In: *Geophysical Journal International* 205.1 (Feb. 2016), pp. 531–535. DOI: 10.1093/gji/ggw023.

[29] A. B. Weglein. 'Multiples: Signal or noise?' In: *GEOPHYSICS* 81.4 (2016), pp. V283–V302. DOI: 10.1190/geo2014-0486.1.

[30] T. Cui, J. Rickett, I. Vasconcelos and B. Veitch. ' Target-oriented full-waveform inversion using Marchenko redatumed wavefields'. In: *Geophysical Journal International* 223.2 (July 2020), pp. 792–810. ISSN: 0956-540X. DOI: 10.1093/gji/ggaa333.

[31] L. Diekmann, I. Vasconcelos, D. Cummings and A. Curtis. 'Towards exact linearized full-waveform inversion via Marchenko redatuming'. In: *First International Meeting for Applied Geoscience & Energy Expanded Abstracts*. 2021, pp. 3380–3384. DOI: 10.1190/segam2021-3583558.1.

[32] J. van der Neut, M. Ravasi, Y. Liu and I. Vasconcelos. 'Target-enclosed seismic imaging'. In: *GEOPHYSICS* 82.6 (2017), Q53–Q66. DOI: 10.1190/geo2017-0166.1.

[33] M. Born, E. Wolf, A. B. Bhatia, P. C. Clemmow, D. Gabor, A. R. Stokes, A. M. Taylor, P. A. Wayman and W. L. Wilcock. *Principles of Optics: Electromagnetic Theory of Propagation, Interference and Diffraction of Light*. 7th ed. Cambridge University Press, 1999. DOI: 10.1017/CBO9781139644181.

[34] P. M. van den Berg. 'Acoustic Waves'. In: *Forward and Inverse Scattering Algorithms based on Contrast Source Integral Equations*. John Wiley & Sons, Ltd, 2021. Chap. 2, pp. 79–179. ISBN: 9781119741602. DOI: https://doi.org/10.1002/9781119741602.ch2.

[35] D. W. Marquardt. 'An Algorithm for Least-Squares Estimation of Nonlinear Parameters'. In: *Journal of the Society for Industrial and Applied Mathematics* 11.2 (1963), pp. 431–441. URL: http://www.jstor.org/stable/2098941.

[36] 'APPENDIX B - Interactions of One-Way Acoustic Wave Fields'. In: *Elastic Wave Field Extrapolation*. Ed. by C. WAPENAAR and A. BERKHOUT. Vol. 2. Advances in Exploration Geophysics. Elsevier, 1989, pp. 433–447. DOI: https://doi.org/10.1016/B978-0-444-88472-5.50019-9.

[37] J. W. Thorbecke, E. Slob, J. Brackenhoff, J. van der Neut and K. Wapenaar. 'Implementation of the Marchenko method'. In: *GEOPHYSICS* 82.6 (2017), WB29–WB45. DOI: 10.1190/geo2017-0108.1.

[38] J. W. Thorbecke and D. Draganov. 'Finite-difference modeling experiments for seismic interferometry'. In: *GEOPHYSICS* 76.6 (2011), H1–H18. DOI: 10.1190/geo2010-0039.1.

[39] F. Broggini, R. Snieder and K. Wapenaar. 'Data-driven wavefield focusing and imaging with multidimensional deconvolution: Numerical examples for reflection data with internal multiples'. In: *GEOPHYSICS* 79.3 (2014), WA107–WA115. DOI: 10.1190/geo2013-0307.1.

[40] D. F. Barrera, J. Schleicher and J. Brackenhoff. 'Interferometric redatuming by deconvolution and correlation-based focusing'. In: *GEOPHYSICS* 86.1 (2021), Q1–Q13. DOI: 10.1190/geo2019-0208.1.

[41] L. Diekmann and I. Vasconcelos. 'Focusing and Green's function retrieval in three-dimensional inverse scattering revisited: A single-sided Marchenko integral for the full wave field'. In: *Phys. Rev. Research* 3 (1 2021), p. 013206. DOI: 10.1103/PhysRevResearch.3.013206.

[42] M. Dukalski and K. de Vos. 'Marchenko inversion in a strong scattering regime including surface-related multiples'. In: *Geophysical Journal International* 212.2 (Oct. 2017), pp. 760–776. DOI: 10.1093/gji/ggx434.

[43] M. Staring, R. Pereira, H. Douma, J. van der Neut and K. Wapenaar. 'Source-receiver Marchenko redatuming on field data using an adaptive double-focusing method'. In: *GEOPHYSICS* 83.6 (2018), S579–S590. DOI: 10.1190/geo2017-0796.1.

[44] S. Shoja, G. Meles and K. Wapenaar. 'A Proposal for Marchenko-Based Target-Oriented Full Waveform Inversion'. In: *Proceedings of EAGE 2020 Annual Conference & Exhibition Online* 2020.1 (2020), pp. 1–5. DOI: https://doi.org/10.3997/2214-4609.202011020.

4

TARGET-ORIENTED LEAST-SQUARES REVERSE-TIME MIGRATION WITH MARCHENKO REDATUMING AND DOUBLE-FOCUSING: FIELD DATA APPLICATION

Recently, the focus of reflection seismologists has shifted to applications where a high-resolution image of the subsurface is required. Least-Squares Reverse-Time Migration (LSRTM) is a common tool used to compute such images. Still, its high computational costs have led seismologists to use target-oriented LSRTM for imaging only a small target of interest within a larger subsurface block. Redatuming the data to the upper boundary of the target of interest is one approach to target-oriented LSRTM. Still, many redatuming methods cannot account for multiple scatterings within the overburden. An algorithm for target-oriented least-squares reverse time migration that integrates Marchenko redatuming and double-focusing is presented. This redatuming method accounts for all orders of multiple scattering in the overburden, thus improving the accuracy of target-oriented LSRTM. Moreover, the effectiveness of a double-focusing algorithm in reducing the data size by decreasing both spatial and temporal dimensions is demonstrated. The algorithm's performance is evaluated using field data acquired in the Norwegian Sea. The numerical results show that our target-oriented LSRTM algorithm can reduce the internal multiple effects and increase the resolution of the resulting image.

4.1. INTRODUCTION

Seismic imaging and inversion are a set of techniques used by geophysicists to estimate parameters related to wave propagation, such as reflectivity, velocity, and density, within the Earth's subsurface. A network of sources and receivers is positioned on the Earth's surface to produce and record seismic waves, from which these parameters are determined. Geophysicists typically assume a subsurface model that consists of a background model (m_0) for long wavelengths and a perturbation model for short wavelengths (δm), based on a weak-scattering assumption [1, 2]. The primary objective of seismic imaging is to generate a structural image of the short-wavelength perturbation model (δm).

Reverse-Time Migration (RTM) is a popular method among different imaging techniques since it can produce high-resolution images and better handle complex geological structures [3–6]. RTM creates images by cross-correlating the forward-propagated wavefield and its back-propagated counterpart based on the Born approximation. However, improving the resolution and quality of RTM images is still possible by inverting the Lippmann-Schwinger integral under the Born approximation for the perturbation model with a least-squares algorithm [7–11]. This inversion process is known as Least-Squares Reverse-time migration (LSRTM).

However, LSRTM is a computationally expensive algorithm [8, 12–14]. To reduce the computational cost of LSRTM, one can restrict the model's dimensions by focusing on a small area inside the big block of the subsurface model. To compute the image of this smaller region, the wavefield on the upper boundary of this region is needed at least. The process of computing the wavefield on the boundary of this target from surface recorded data is called redatuming [15–23]. One prominent redatuming technique is Marchenko redatuming [24–26].

Marchenko redatuming [24, 25, 27–30] can create virtual receivers on the boundary of the target of interest while accounting for all orders of internal multiple scattering effects and reflections. Since Marchenko redatuming and Green's functions retrieval are powerful tools, researchers use them to address seismic imaging and inversion issues [6, 31–33]. Moreover, it is possible to perform a double-sided redatuming using Marchenko focusing functions. Double-sided redatuming creates virtual sources in addition to virtual receivers at the boundary of the target. The process of double-sided redatuming is called double-focusing [34, 35]. Marchenko double-focused wavefields account for all orders of internal multiples generated inside the overburden, enabling us to create images with less impact from internal multiples. Moreover, Marchenko double-focusing compacts the data's time axis, reducing its size even more.

This chapter combines the Marchenko double-focusing and target-oriented LSRTM algorithm to create high-resolution artifact-free images of a marine data set from the Vøring region in the Norwegian Sea. First, we review the theory of target-oriented LSRTM with Marchenko double-focusing, which is fully developed and is validated with synthetic models by Shoja et. al, 2023[35]. Second, we apply this algorithm to a

marine dataset, and finally, we discuss the results and conclude the paper.

4.2. THEORY

4.2.1. LEAST-SQUARES REVERSE-TIME MIGRATION

[12] show that classical RTM can be derived from the Born approximation of seismic reflection data. In the Born approximation, the incident wavefield (P^{inc}) can be estimated using the background Green's function. The perturbation model is expressed as $\delta m = (\frac{1}{c^2} - \frac{1}{c_0^2})$ where c represents the medium velocity and c_0 represents the background velocity. This equation links δm to the scattered data (P^{scat}) through a linear equation [1, 36, 37]:

$$P_{pred}^{scat}(\mathbf{x}_r, \mathbf{x}_s, \delta m, \omega) = \frac{\omega^2}{\rho_0} \int_V G_0(\mathbf{x}_r, \mathbf{x}, \omega) \delta m(\mathbf{x}) G_0(\mathbf{x}, \mathbf{x}_s, \omega) W(\omega) \, d\mathbf{x}. \tag{4.1}$$

The integral in Equation 4.1 is computed throughout the model's volume (V). Here, $P^{inc}(\mathbf{x}, \mathbf{x}_s, \omega) \approx G_0(\mathbf{x}, \mathbf{x}_s, \omega) W(\omega)$. Moreover, ω is the angular frequency, W is the source signature, G_0 is the Green's function computed in the background model (c_0), ρ_0 is the background density, and P_{pred}^{scat} is the scattered predicted data. The subscripts "r" and "s" indicate the receiver and source, respectively. This equation can be expressed in an operator format as follows:

$$P_{pred}^{scat}(\mathbf{x}_r, \mathbf{x}_s, \delta m, \omega) = \mathscr{L} \delta m. \tag{4.2}$$

Here $\mathscr{L}$ is the forward Born operator.

The standard method of reverse-time migration involves obtaining an approximate reflectivity model by taking the adjoint of $\mathscr{L}$ and applying it to the observed scattered data:

$$\delta m^{mig}(\mathbf{x}) = \mathscr{L}^\dagger P_{obs}^{scat}. \tag{4.3}$$

Since the adjoint of this kernel is merely an approximation of its inverse, the resolution of the perturbation model obtained through this process is limited.

To tackle the problem of limited resolution, scholars have adopted a least-squares strategy in which the adjoint operator ($\mathscr{L}^\dagger$) is substituted with a damped least-squares solution [7, 12, 38]:

$$\delta m^{mig} = [\mathscr{L}^\dagger \mathscr{L} + \epsilon]^{-1} \mathscr{L}^\dagger P_{obs}^{scat}. \tag{4.4}$$

Here, $\mathscr{L}^\dagger \mathscr{L}$ is the Hessian matrix, and ϵ is a damping factor. Unfortunately, calculating the Hessian matrix ($\mathscr{L}^\dagger \mathscr{L}$) and its inverse is computationally infeasible. As an alternative, an iterative algorithm that minimizes the L2-norm of the discrepancy between the observed and anticipated data is often used to update the reflectivity model:

$$C(\delta m) = \frac{1}{2} \| P_{pred}^{scat}(\delta m) - P_{obs}^{scat} \|_2^2. \tag{4.5}$$

One potential way to tackle this optimization problem is by utilizing a conjugate gradient algorithm [39]. In least-squares reverse-time migration, the background velocity model ($c_0(\mathbf{x})$) is not changed, and only the reflectivity model (δm) is updated, resulting in the Green's functions of Equation 4.1 being calculated only once. To learn more about least-squares reverse-time migration, please see [1].

4.2.2. MARCHENKO REDATUMING AND DOUBLE-FOCUSING

Marchenko redatuming is an innovative data-driven technique that can recover the Green's function above the target area's surface, including all orders of multiple-scattered events. This method only requires the reflection response at the surface and a smooth background velocity model of the overburden capable of predicting the direct arrival from the surface to the redatuming level.

The following coupled Marchenko-type representations are solved iteratively to retrieve the Green's functions at the redatuming level [24]:

$$G_{Mar}^-(\mathbf{x}_v,\mathbf{x}_r,\omega) = \int_{\mathscr{D}_{acq}} R(\mathbf{x}_r,\mathbf{x}_s,\omega) f_1^+(\mathbf{x}_s,\mathbf{x}_v,\omega) \, d\mathbf{x}_s - f_1^-(\mathbf{x}_r,\mathbf{x}_v,\omega), \tag{4.6}$$

and

$$G_{Mar}^+(\mathbf{x}_v,\mathbf{x}_r,\omega) = -\int_{\mathscr{D}_{acq}} R(\mathbf{x}_r,\mathbf{x}_s,\omega) f_1^-(\mathbf{x}_s,\mathbf{x}_v,\omega)^* \, d\mathbf{x}_s + f_1^+(\mathbf{x}_r,\mathbf{x}_v,\omega)^*. \tag{4.7}$$

In these equations, $\mathscr{D}_{acq}$ represents the acquisition surface where $\mathbf{x}_s$ and $\mathbf{x}_r$ are situated. G_{Mar}^- and G_{Mar}^+ denote the up-going and down-going components of the Marchenko redatumed Green's function, respectively (see Fig. 4.1a and 4.1b). Additionally, $f_1^-(\mathbf{x}_s,\mathbf{x}_v,\omega)$ and $f_1^+(\mathbf{x}_s,\mathbf{x}_v,\omega)$ denote the up-going and down-going parts of the focusing function, respectively, with the subscript "v" denoting a virtual point situated on the redatuming level denoted by $\mathscr{D}_{tar}$. Furthermore, $R(\mathbf{x}_r,\mathbf{x}_s,\omega)$ refers to the dipole response of the medium at the acquisition surface, and it is related to the up-going Green's function (G^-) via the following relationship:

$$R(\mathbf{x}_r,\mathbf{x}_s,\omega) = \frac{\partial_{3,s} G^-(\mathbf{x}_r,\mathbf{x}_s,\omega)}{\frac{1}{2} i\omega\rho(\mathbf{x}_s)}, \tag{4.8}$$

The partial derivative in the downward direction taken at $\mathbf{x}_s$ is denoted by $\partial_{3,s}$. This partial vertical derivative is computed in the frequency-wavenumber domain by multiplying the wavefield by ik_z, where k_z is the vertical wavenumber. $\rho(\mathbf{x}_s)$ is the density at $\mathbf{x}_s$. It is important to remove horizontally propagating waves and surface-related multiples before inserting $R(\mathbf{x}_r,\mathbf{x}_s,\omega)$ into Equations 4.6 and 4.7. The detailed derivation of these integrals and their solution for computing the focusing functions and Green's functions can be found in [24] and [40].

The above-mentioned equations correspond to single-sided redatuming. To perform a double-sided redatuming, a convolution operation on the up-going and down-going parts of the Marchenko redatumed Green's function is proposed by

[34]. This operation involves filtering the down-going focusing function in a multi-dimensional manner:

$$G_{df}^{-,+}(\mathbf{x}_v,\mathbf{x}_v',\omega) = \int_{\mathcal{D}_{acq}} G_{Mar}^{-}(\mathbf{x}_v,\mathbf{x}_r,\omega)\mathscr{F}_1^{+}(\mathbf{x}_r,\mathbf{x}_v',\omega)\,d\mathbf{x}_r, \tag{4.9}$$

and

$$G_{df}^{+,+}(\mathbf{x}_v,\mathbf{x}_v',\omega) = \int_{\mathcal{D}_{acq}} G_{Mar}^{+}(\mathbf{x}_v,\mathbf{x}_r,\omega)\mathscr{F}_1^{+}(\mathbf{x}_r,\mathbf{x}_v',\omega)\,d\mathbf{x}_r, \tag{4.10}$$

where

$$\mathscr{F}_1^{+}(\mathbf{x}_r,\mathbf{x}_v',\omega) = \frac{\partial_{3,r} f_1^{+}(\mathbf{x}_r,\mathbf{x}_v',\omega)}{\frac{1}{2}i\omega\rho(\mathbf{x}_r)}. \tag{4.11}$$

Here the vertical derivative is taken with respect to $\mathbf{x}_r$. Equations 4.9 and 4.10 use superscripts to indicate the direction of propagation at the receiver and source locations, respectively. The term "df" stands for "double-focused." This process is referred to as "Marchenko double-focusing."

The Marchenko double-focusing technique yields two Green's functions, namely a down-going ($G_{df}^{+,+}$) and an up-going ($G_{df}^{-,+}$) Green's function (fig. 4.1c and 4.1d). The down-going Green's function consists of a band-limited delta function and interactions between the target and the overburden. $G_{df}^{-,+}$ can be interpreted as the continuation of propagation of $G_{df}^{+,+}$ through the target and recording the up-going part of it at the redatuming level. This up-going wavefield includes interactions between the target and the overburden on the source side. In contrast, the conventional double-focusing approach involves using the inverse of the direct arrival of the transmission response of the overburden instead of the down-going Marchenko focusing function. However, this approach cannot predict and remove the multiples generated by the overburden. In subsequent sections, the term "double-focusing" is a general expression that refers to both approaches, and it is explicitly mentioned where a distinction between the methods is necessary.

4.2.3. TARGET-ORIENTED LSRTM BY MARCHENKO DOUBLE-FOCUSING

I fully developed this theory in Chapter 2. The following integral is the base for target-oriented LSRTM by Marchenko double-focusing:

$$\hat{P}_{pred}^{scat}(\mathbf{x}_{vr}',\mathbf{x}_{vs}',\delta m,\omega) = \frac{\omega^2}{\rho_0}\int_v \hat{G}_0(\mathbf{x}_{vr}',\mathbf{x},\omega)\delta m(\mathbf{x}) P_{df}^{inc}(\mathbf{x},\mathbf{x}_{vs}',\omega)\,d\mathbf{x}. \tag{4.12}$$

Here, v is the target volume, $\mathbf{x}$ is a point inside the target, and $\mathbf{x}_{vs}'$ and $\mathbf{x}_{vr}'$ are the virtual source and virtual receiver locations on the upper boundary of the target, respectively. Moreover,

$$P_{df}^{inc}(\mathbf{x},\mathbf{x}_{vs}',\omega) = \int_{\mathcal{D}_{tar}} \frac{\partial_{3,vs} G_0(\mathbf{x},\mathbf{x}_{vs},\omega)}{\frac{1}{2}i\omega\rho(\mathbf{x}_{vs})} G_{df}^{+,+}(\mathbf{x}_{vs},\mathbf{x}_{vs}',\omega)W(\omega)\,d\mathbf{x}_{vs}, \tag{4.13}$$
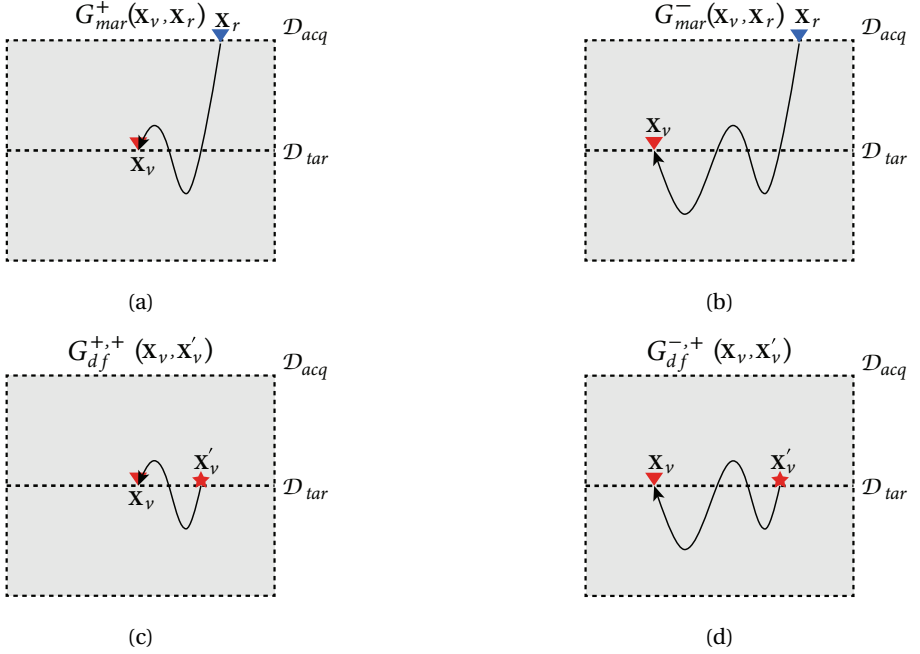
Figure 4.1.: The Green's functions resulting from Marchenko redatuming and double-focusing. a) down-going part of Marchenko Green's function, b) up-going part of Marchenko Green's function, c) down-going Marchenko double-focused Green's function, and d) up-going Marchenko double-focused Green's function.

and

$$\hat{G}_0(\mathbf{x}'_{vr}, \mathbf{x}, \omega) = \int_{\mathcal{D}_{tar}} \Gamma(\mathbf{x}'_{vr}, \mathbf{x}_{vr}, \omega) G_0(\mathbf{x}_{vr}, \mathbf{x}, \omega) \, d\mathbf{x}_{vr}, \tag{4.14}$$

where

$$\Gamma(\mathbf{x}'_{vr}, \mathbf{x}_{vr}, \omega) = \int_{\mathcal{D}_{acq}} G_d^+(\mathbf{x}'_{vr}, \mathbf{x}_s, \omega)^{-1} G_d^+(\mathbf{x}_{vr}, \mathbf{x}_s, \omega) \, d\mathbf{x}_s \tag{4.15}$$

is a point-spread function that acts as a band limitation filter on the predicted data. In Equation 4.15, G_d^+ is the first arrival of the Green's function between the target boundary and the surface. For a complete derivation of the above equations and an analysis of the effects of the point-spread function ($\Gamma(\mathbf{x}'_{vr}, \mathbf{x}_{vr}, \omega)$), we refer to Chapter 2. Thus, the new cost function is:

$$C(\delta m) = \frac{1}{2} \left\| \hat{P}^{scat}_{pred}(\delta m) - \hat{P}^{scat}_{obs} \right\|_2^2, \tag{4.16}$$

which we solve with a conjugate gradient algorithm.

4.3. FIELD DATA EXAMPLE

4.3.1. FIELD DATA EXPLANATION

This part of the chapter shows the results of the Marchenko-based target-oriented LSRTM on a field dataset provided by Equinor, which was acquired in the Norwegian Sea in 1994. The depth of the water bottom is $1.5km$, which is deep enough to separate the free-surface multiple reflections from the primary and internal multiple reflections. The field dataset contains 399 shot gathers with 180 traces per gather, and the spatial sampling of sources and receivers is $25m$. The field dataset was processed according to [41] methodology, which involved muting the direct wave, estimating near-offset traces through the parabolic Radon transform [42], compensating for 3D effects by multiplying with $\sqrt{t}$, and deconvolving the source wavelet. Source-receiver reciprocity is also applied to create offsets in the positive direction to prepare the dataset for the Estimation of Primaries through the Sparse Inversion (EPSI) method to remove free-surface multiples [43]. After source-receiver reciprocity, each gather contains 371 receivers. Table 4.1 shows the acquisition parameters, and Figure 4.2 shows the acquisition geometry of this dataset. We apply a gain of $1.73e^{1.3t}$ to the reflection response as recommended by [44] to compensate for the absorption effect. However, with this scaling function, the Marchenko redatuming procedure does not sufficiently reduce the multiple reflections energy for imaging. A wrong scaling function can result in more artifacts [27]. Thus, we multiplied the reflection response already scaled with the aforementioned scaling function, with a range of values to adjust it for imaging. Then, we measured the L2-norm of the double-focused gather to find the value which produces the minimum energy [29, 45]. Figure 4.3 shows the L2 norm of the double-focused gather against the values we use. According to Figure 4.3, we choose value 10, which results in an adjusted scaling factor of $17.3e^{1.3t}$ for a non-scaled reflection response.

Table 4.1.: Acquisition Parameters for the dataset

Parameter	Value
Number of source positions	399
Source spacing	25 m
First source position	5,000 m
Final source position	14,950
Number of receiver positions per source	180
Receiver spacing	25m
Minimum source-receiver offset	150 m
Maximum source-receiver offset	4,625 m
Number of time samples	2001
Sampling rate	0.004 s
High-cut frequency	90 Hz

Figure 4.4 shows the surface reflection response after preprocessing, with a source
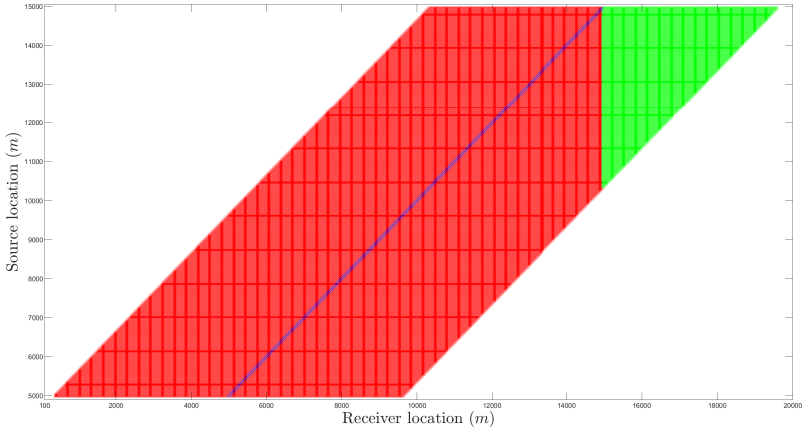
Figure 4.2.: The acquisition geometry of the data set. Blue crosses show the source locations, red crosses show the receivers' locations and green crosses show the dummy traces added after source-receiver reciprocity to have an equal number of receivers per shot. The receivers on the left side of the sources are the real ones, and the receivers on the right side are added by source-receiver reciprocity.
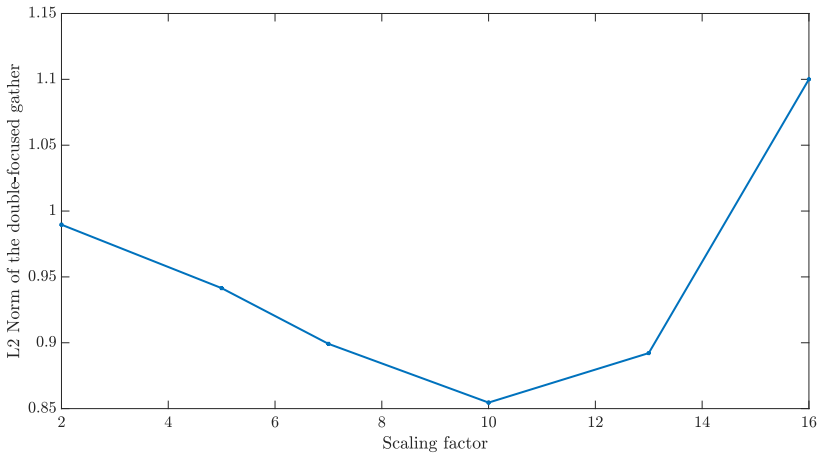

Figure 4.3.: L2 norm of the gather shown in Figure 4.6a against different scaling values.

located at $\mathbf{x}_s = (5000m, 0m)$. We choose two different targets inside the medium.
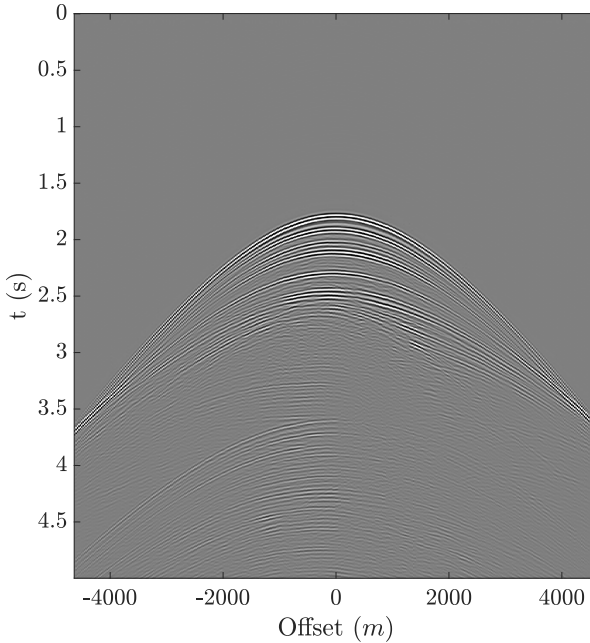
Figure 4.4.: Reflection response with a source located at $\mathbf{x}_s = (5000m, 0m)$. A Ricker wavelet with a dominant frequency of $30Hz$ is convolved with the data for better visualization.

4.3.2. LSRTM WITH DOUBLE-FOCUSING

We choose two targets of interest below a complex overburden that produces strong internal multiples, and we aim to show that our algorithm can handle these internal multiples correctly and reduce the artifacts imposed by them in the image.

TARGET OF INTEREST 1

Figure 4.5 shows the smooth velocity model provided by Equinor for migration. The red rectangle inside the velocity model indicates the target area and the virtual sources and receivers' positions are at the upper boundary of this target area.

We apply the double-focusing algorithm to the field data for this target. For this, we define 241 virtual sources and 241 virtual receivers with a spacing of $12.5m$ at $2500m$ depth extending from $9000m$ to $12000m$ over the upper boundary of the first target area. The up-going wavefield resulting from double-focusing is used as input for LSRTM and is called 'observed data' in the following. Figure 4.6 shows the observed, and predicted data, and the residuals of Marchenko double-focusing target-oriented LSRTM. Moreover, Figure 4.7 shows the same but for a conventional double-focusing approach. Conventional means using the inverse of the direct
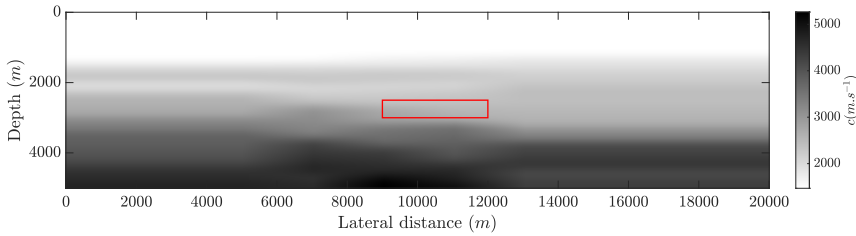
Figure 4.5.: The smooth velocity model provided by Equinor for migration. The red rectangle inside the velocity model indicates the first target area. The virtual sources and receivers' positions are at the upper boundary of this target area.

arrival between the target and the surface as the redatuming operator instead of the Marchenko focusing functions. The non-physical noises inside the data are mostly caused by imperfect surface multiple elimination in this part of the data and 3D effects in 2D gathers. The computational advantage of target-oriented LSRTM with double-focused data is twofold. First, this algorithm reduces the spatial dimension of the problem, and second, it reduces the temporal dimension of the problem as well. The original recording time of the data at the surface is 8 seconds, whereas the temporal length of the double-focused data is 0.5 seconds.

Figure 4.8 compares the LSRTM images of using Marchenko and conventional double-focused data as input. Figure 4.8 shows some improvements from using Marchenko double-focused wavefields compared to conventional double-focused ones.

Moreover, Figure 4.9 compares the RTM and LSRTM images of Marchenko double-focused data as input. The LSRTM algorithm improved the quality of the image.

TARGET OF INTEREST 2

Here we choose another target. This target is located between depths of $2100m$ and $2600m$ and lateral extension from $7000m$ to $10000m$ as shown in Figure 4.10. Virtual sources and receivers are located at the upper boundary of this target area.

Figure 4.11 shows the observed, and predicted data, and the residuals of the Marchenko double-focusing approach. Figure 4.12 shows the same for the

Figure 4.6.: Marchenko double-focused data with a virtual source located at
$\mathbf{x}_{\nu s} = (10500m, 2500m)$ and virtual receivers at the same depth as virtual
sources. a) observed data, b) predicted data after 35 iterations of LSRTM,
and c) residuals after 35 iterations of LSRTM.

Figure 4.7.: Conventional double-focused data with a virtual source located at
$\mathbf{x}_{\nu s} = (10500m, 2500m)$. a) observed data, b) predicted data after 35
iterations of LSRTM, and c) residuals after 35 iterations of LSRTM.

conventional double-focusing approach.

Moreover, Figure 4.13 shows the LSRTM images of the target-oriented algorithm
with Marchenko and conventional double-focusing. The red arrows, rectangle, and

Figure 4.8.: Comparison of images obtained with Marchenko target-oriented LSRTM
(a) and Conventional target-oriented LSRTM (b). Red lines in panel
(a) delineate some trends that are not visible in panel (b), and the
red arrows and rectangles in panel (b) show some events that may be
internal multiple reflection artifacts that are suppressed in panel (a).

Figure 4.9.: Comparison of images obtained with Marchenko target-oriented RTM (a)
and LSRTM (b) of the first target.

ellipse indicate the internal multiple reflections that are suppressed by our method.
Figure 4.14 shows the RTM and LSRTM images of the target-oriented algorithm with
Marchenko double-focusing. The quality and resolution of the image are increased
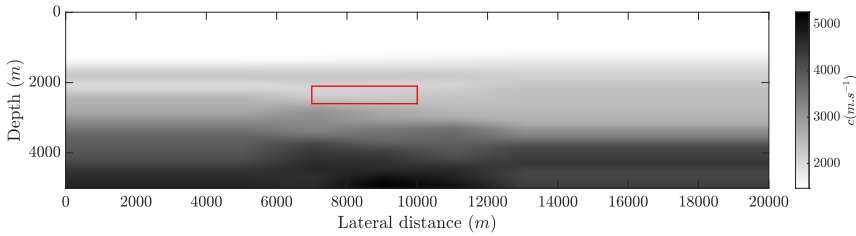
Figure 4.10.: The smooth velocity model provided by Equinor for migration. The red rectangle inside the velocity model indicates the second target area and the virtual sources and receivers' positions are at the upper boundary.
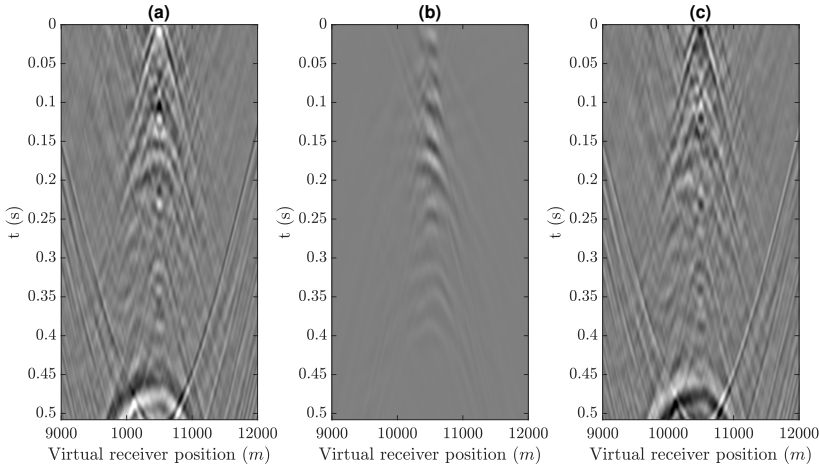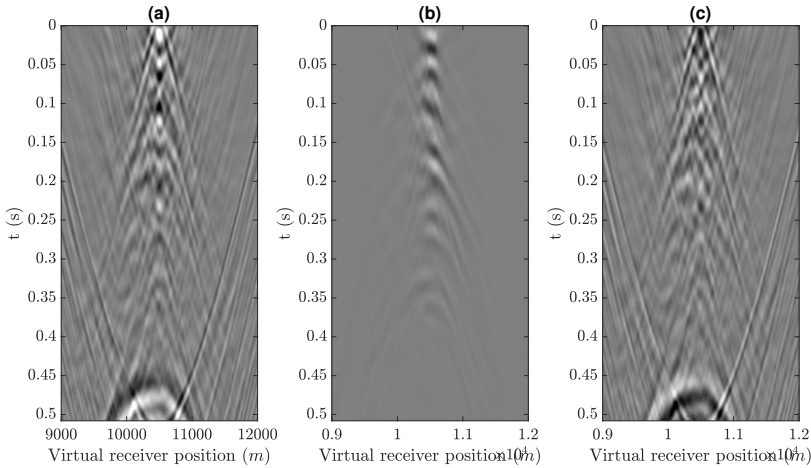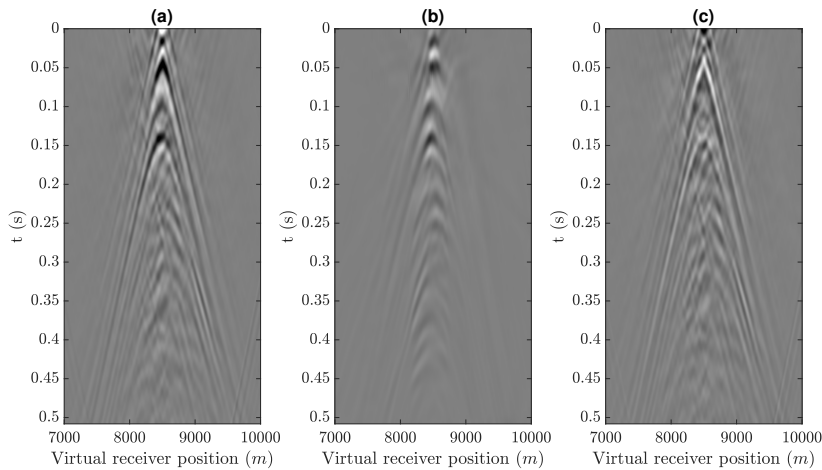

Figure 4.11.: Marchenko double-focused data with a virtual source located at $\mathbf{x}_{vs} = (8500m, 2100m)$ and virtual receivers at the same depth as virtual sources. a) observed data, b) predicted data after 35 iterations of LSRTM, and c) residuals after 35 iterations of LSRTM.

by the LSRTM algorithm.
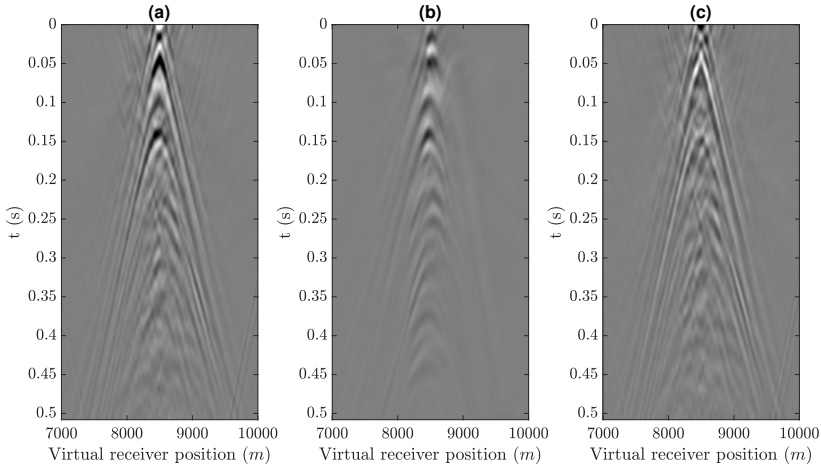
Figure 4.12.: Convetional double-focused data with a virtual source located at $\mathbf{x}_{vs} = (8500m, 2100m)$. a) observed data, b) predicted data after 35 iterations of LSRTM, and c) residuals after 35 iterations of LSRTM.
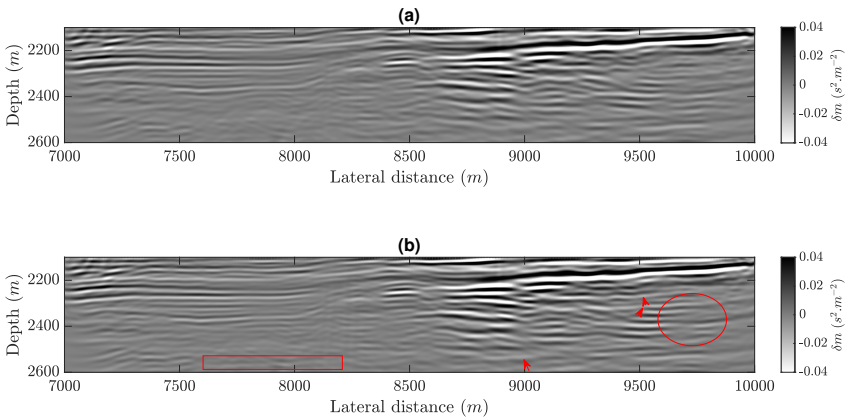
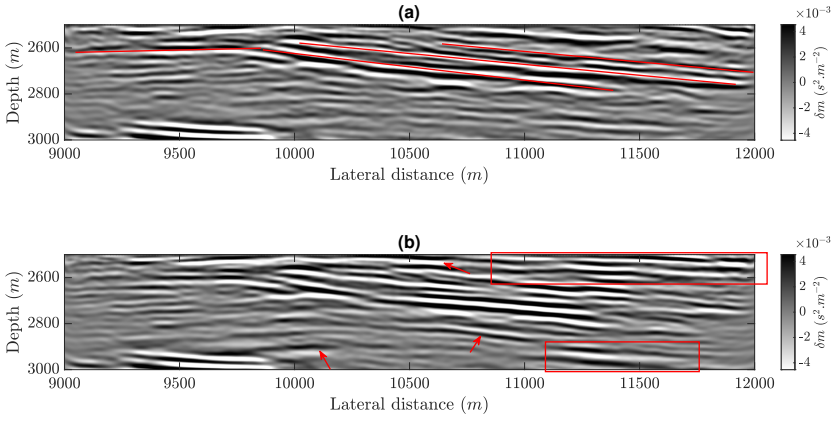

Figure 4.13.: Comparison of images obtained with Marchenko target-oriented LSRTM (a) and Conventional target-oriented LSRTM (b). The red arrows, rectangle, and ellipse in panel (b) indicate some of the internal multiple reflection artifacts that are suppressed in panel (a)

4.4. DISCUSSION

In section 2 of this chapter, we derive a target-oriented LSRTM algorithm based on double-focusing that can significantly reduce the dimensions of the problem, which
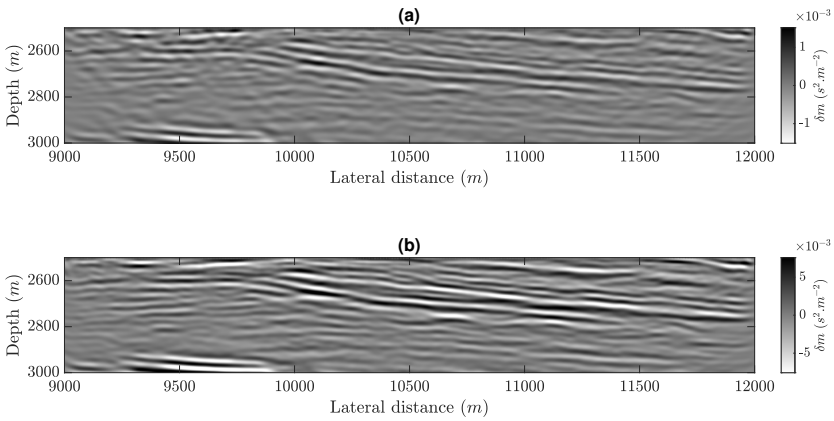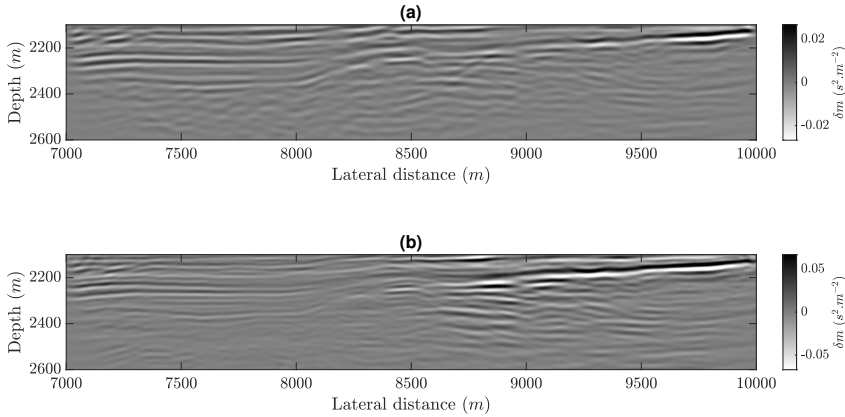
Figure 4.14.: Comparison of images obtained with Marchenko target-oriented RTM (a) and LSRTM (b) of the second target.

also reduces the computational costs of the LSRTM algorithm. We also integrate the Marchenko double-focusing algorithm with our target-oriented LSRTM algorithm to reduce the artifacts caused by internal multiple reflections.

To demonstrate the advantages of our proposed algorithm, we applied it to a dataset acquired by Equinor in the Norwegian Sea in 1994. We chose two different target zones. Figures 4.5 and 4.10 show our targets of interest embedded in the entire domain of the region. This spatial dimension reduction is to validate the first advantage we mentioned above. Figures 4.6a, 4.7a, 4.11a, and 4.12a show the double-focused data with a recording duration of 0.5s, whereas the recording time of the original data is 8s.

To move forward with our investigation, we showed the imaging results with double-focusing for both targets. Figure 4.8 compares the imaging results of the conventional and Marchenko double-focusing target-oriented LSRTM. The first panel (fig. 4.8a) shows the LSRTM result of our proposed algorithm with Marchenko double-focused data, and the second panel (fig. 4.8b) shows the LSRTM results with conventional double-focused data. Comparing these two panels reveals that using Marchenko wavefields leads to better visualization of true events and fewer artifacts due to internal multiples, delineated by the lines and arrows in those panels. Moreover, Figure 4.9 shows the resolution and quality improvement of target-oriented LSRTM compared to target-oriented RTM with Marchenko double-focusing.

The same discussion stands for the second target. Figure 4.13 shows a comparison between conventional and Marchenko double-focusing target-oriented

LSRTM images where the internal multiple suppression is visible and indicated by arrows and an ellipse, and Figure 4.14 shows the RTM and LSRTM images of Marchenko double-focusing target-oriented LSRTM. The quality and resolution of the image are increased noticeably. The internal multiple suppression results of this chapter are in agreement with the findings of [41] and [46].

In both target areas, the double-focused gathers experience multiple flawed preprocessing stages that cannot be adequately explained by the forward modeling or the Marchenko approach. The non-physical artifacts within the data primarily arise from incomplete surface multiple removal and the impact of 3D effects in 2D datasets. These spurious elements in the data have led to a substantial residual vector.

4

4.5. CONCLUSION

This chapter discusses a target-oriented LSRTM algorithm based on double-focusing. The advantages of this algorithm are: 1) reduction of the spatial dimensions of the problem by choosing a smaller target of interest, and 2) reduction of the temporal dimension of the problem by creating both virtual sources and receivers at the boundary of the target, which leads to lower computational costs. One can also opt for more sophisticated redatuming algorithms such as Marchenko redatuming and double-focusing to create virtual sources and receivers. The advantage of using Marchenko double-focusing compared to a more conventional redatuming algorithm is the ability to predict the internal multiple reflections inside the overburden and a reduction of artifacts due to these multiple reflections.

The reason for choosing double-focusing instead of multidimensional deconvolution (MDD) is to avoid another inversion step in our algorithm. MDD is an inversion process with its own uncertainties and associated errors. On the other hand, the double-focusing is a multidimensional convolution process with a unique output. As it is shown in [35] and this paper, the predicted data, which uses the double-focused down-going wavefield at the boundary of the target, can predict the interactions between the target and the overburden and fit them to the double-focused observed data.

Present-day seismic imaging and inversion applications need more accurate and higher-resolution images. Computing higher-resolution images demands significant amounts of computational power and time. Thus, devising algorithms that can reduce this computational burden is essential. Our proposed target-oriented algorithm is not only able to greatly reduce the spatial and temporal dimensions of the problem but also can reduce the artifacts due to internal multiple reflections by integrating Marchenko double-focusing with LSRTM algorithm. Consequently, our algorithm enables us to create higher-resolution images with fewer artifacts at a lower computational cost.

REFERENCES

[1] G. T. Schuster. *SEISMIC INVERSION*. Society of Exploration Geophysicists, 2017.

[2] J. F. Claerbout. *Imaging the Earth's Interior*. BlackWell Scientific Publications, 1985.

[3] E. Baysal, D. D. Kosloff and J. W. C. Sherwood. 'Reverse time migration'. In: *GEOPHYSICS* 48.11 (1983), pp. 1514–1524. DOI: 10.1190/1.1441434.

[4] G. A. McMechan. 'MIGRATION BY EXTRAPOLATION OF TIME-DEPENDENT BOUNDARY VALUES'. In: *Geophysical Prospecting* 31.3 (1983), pp. 413–420. DOI: https://doi.org/10.1111/j.1365-2478.1983.tb01060.x.

[5] H.-W. Zhou, H. Hu, Z. Zou, Y. Wo and O. Youn. 'Reverse time migration: A prospect of seismic imaging methodology'. In: *Earth-Science Reviews* 179 (2018), pp. 207–227. DOI: https://doi.org/10.1016/j.earscirev.2018.02.008.

[6] L. Zhang, J. Thorbecke, K. Wapenaar and E. Slob. 'Transmission compensated primary reflection retrieval in the data domain and consequences for imaging'. In: *GEOPHYSICS* 84.4 (2019), Q27–Q36. DOI: 10.1190/geo2018-0340.1.

[7] G. Dutta, M. Giboli, C. Agut, P. Williamson and G. T. Schuster. 'Least-squares reverse time migration with local Radon-based preconditioning'. In: *GEOPHYSICS* 82.2 (2017), S75–S84. DOI: 10.1190/geo2016-0117.1.

[8] Y. Tang. 'Target-oriented wave-equation least-squares migration/inversion with phase-encoded Hessian'. In: *GEOPHYSICS* 74.6 (2009), WCA95–WCA107. DOI: 10.1190/1.3204768.

[9] Y. Liu, X. Liu, A. Osen, Y. Shao, H. Hu and Y. Zheng. 'Least-squares reverse time migration using controlled-order multiple reflections'. In: *GEOPHYSICS* 81.5 (2016), S347–S357. DOI: 10.1190/geo2015-0479.1.

[10] X. Huang. 'Full wavefield inversion with multiples: Nonlinear Bayesian inverse multiple scattering theory beyond the Born approximation'. In: *GEOPHYSICS* 88.6 (2023), T289–T303. DOI: 10.1190/geo2022-0604.1.

[11] H. Kaur, N. Pham and S. Fomel. 'Improving the resolution of migrated images by approximating the inverse Hessian using deep learning'. In: *GEOPHYSICS* 85.4 (2020), WA173–WA183. DOI: 10.1190/geo2019-0315.1. URL: https://doi.org/10.1190/geo2019-0315.1.

[12] W. Dai, P. Fowler and G. T. Schuster. 'Multi-source least-squares reverse time migration'. In: *Geophysical Prospecting* 60.4 (2012), pp. 681–695. DOI: https://doi.org/10.1111/j.1365-2478.2012.01092.x.

[13]   F. J. Herrmann and X. Li. 'Efficient least-squares imaging with sparsity promotion and compressive sensing'. In: *Geophysical Prospecting* 60.4 (2012), pp. 696–712. DOI: https://doi.org/10.1111/j.1365-2478.2011.01041.x.

[14]   M. Farshad and H. Chauris. 'Sparsity-promoting multiparameter pseudoinverse Born inversion in acoustic media'. In: *GEOPHYSICS* 86.3 (2021), S205–S220. DOI: 10.1190/geo2020-0527.1.

[15]   A. A. Valenciano, B. Biondi and A. Guitton. 'Target-oriented wave-equation inversion'. In: *GEOPHYSICS* 71.4 (2006), A35–A38. DOI: 10.1190/1.2213359.

[16]   P. Haffinger, A. Gisolf and P. M. v. d. Berg. 'Towards high resolution quantitative subsurface models by full waveform inversion'. In: *Geophysical Journal International* 193.2 (Feb. 2013), pp. 788–797. ISSN: 0956-540X. DOI: 10.1093/gji/ggt021.

[17]   B. Willemsen, A. Malcolm and W. Lewis. 'A numerically exact local solver applied to salt boundary inversion in seismic full-waveform inversion'. In: *Geophysical Journal International* 204.3 (Feb. 2016), pp. 1703–1720. DOI: 10.1093/gji/ggv547.

[18]   S. Yuan, N. Fuji, S. Singh and D. Borisov. 'Localized time-lapse elastic waveform inversion using wavefield injection and extrapolation: 2-D parametric studies'. In: *Geophysical Journal International* 209.3 (Mar. 2017), pp. 1699–1717. DOI: 10.1093/gji/ggx118.

[19]   Z. Zhao and M. K. Sen. 'Fast image-domain target-oriented least-squares reverse time migration'. In: *GEOPHYSICS* 83.6 (2018), A81–A86. DOI: 10.1190/geo2018-0033.1.

[20]   Q. Guo and T. Alkhalifah. 'Target-oriented waveform redatuming and high-resolution inversion: Role of the overburden'. In: *GEOPHYSICS* 85.6 (2020), R525–R536. DOI: 10.1190/geo2019-0640.1.

[21]   M. Ravasi, I. Vasconcelos, A. Kritski, A. Curtis, C. A. d. C. Filho and G. A. Meles. 'Target-oriented Marchenko imaging of a North Sea field'. In: *Geophysical Journal International* 205.1 (Feb. 2016), pp. 99–104. DOI: 10.1093/gji/ggv528.

[22]   X. Huang, M. Jakobsen, K. Solberg Eikrem and G. Nævdal. 'Target-Oriented Inversion of Time-Lapse Seismic Waveform Data'. In: *Communications in Computational Physics* 28.1 (2020), pp. 249–275. ISSN: 1991-7120. DOI: https://doi.org/10.4208/cicp.OA-2018-0143.

[23]   E. Biondi, G. Barnier, B. Biondi and R. G. Clapp. 'Target-oriented elastic full-waveform inversion through acoustic extended image-space redatuming'. In: *GEOPHYSICS* 88.3 (2023), R269–R296. DOI: 10.1190/geo2022-0404.1.

[24]   K. Wapenaar, J. Thorbecke, J. van der Neut, F. Broggini, E. Slob and R. Snieder. 'Marchenko imaging'. In: *GEOPHYSICS* 79.3 (2014), WA39–WA57. DOI: 10.1190/geo2013-0302.1.

[25] K. Wapenaar, J. Brackenhoff, M. Dukalski, G. Meles, C. Reinicke, E. Slob, M. Staring, J. Thorbecke, J. van der Neut and L. Zhang. 'Marchenko redatuming, imaging, and multiple elimination and their mutual relations'. In: *GEOPHYSICS* 86.5 (2021), WC117–WC140. DOI: 10.1190/geo2020-0854.1.

[26] L. Diekmann and I. Vasconcelos. 'Focusing and Green's function retrieval in three-dimensional inverse scattering revisited: A single-sided Marchenko integral for the full wave field'. In: *Phys. Rev. Research* 3 (1 2021), p. 013206. DOI: 10.1103/PhysRevResearch.3.013206.

[27] J. van der Neut, I. Vasconcelos and K. Wapenaar. 'On Green's function retrieval by iterative substitution of the coupled Marchenko equations'. In: *Geophysical Journal International* 203.2 (Sept. 2015), pp. 792–813. DOI: 10.1093/gji/ggv330.

[28] K. Wapenaar and M. Staring. 'Marchenko-Based Target Replacement, Accounting for All Orders of Multiple Reflections'. In: *Journal of Geophysical Research: Solid Earth* 123.6 (2018), pp. 4942–4964. DOI: https://doi.org/10.1029/2017JB015208.

[29] J. van der Neut, K. Wapenaar, J. Thorbecke and E. Slob. 'Practical challenges in adaptive Marchenko imaging'. In: *SEG Technical Program Expanded Abstracts 2015*. 2015, pp. 4505–4509. DOI: 10.1190/segam2015-5791035.1.

[30] M. Dukalski and K. de Vos. 'Marchenko inversion in a strong scattering regime including surface-related multiples'. In: *Geophysical Journal International* 212.2 (Oct. 2017), pp. 760–776. DOI: 10.1093/gji/ggx434.

[31] T. Cui, J. E. Rickett and I. Vasconcelos. 'Target-oriented waveform inversion'. In: *The Journal of the Acoustical Society of America* $144.3_S upplement$ (Sept. 2018), pp. 1792–1792. ISSN: 0001-4966. DOI: 10.1121/1.5067912.

[32] T. Cui, J. Rickett, I. Vasconcelos and B. Veitch. ' Target-oriented full-waveform inversion using Marchenko redatumed wavefields'. In: *Geophysical Journal International* 223.2 (July 2020), pp. 792–810. ISSN: 0956-540X. DOI: 10.1093/gji/ggaa333.

[33] L. Diekmann, I. Vasconcelos and T. van Leeuwen. 'A note on Marchenko-linearised full waveform inversion for imaging'. In: *Geophysical Journal International* 234.1 (Feb. 2023), pp. 228–242. DOI: 10.1093/gji/ggad066.

[34] M. Staring, R. Pereira, H. Douma, J. van der Neut and K. Wapenaar. 'Source-receiver Marchenko redatuming on field data using an adaptive double-focusing method'. In: *GEOPHYSICS* 83.6 (2018), S579–S590. DOI: 10.1190/geo2017-0796.1.

[35] A. Shoja, J. van der Neut and K. Wapenaar. 'Target-oriented least-squares reverse-time migration using Marchenko double-focusing: reducing the artefacts caused by overburden multiples'. In: *Geophysical Journal International* 233.1 (Apr. 2023), pp. 13–32. DOI: 10.1093/gji/ggac438.

4

[36] M. Born, E. Wolf, A. B. Bhatia, P. C. Clemmow, D. Gabor, A. R. Stokes, A. M. Taylor, P. A. Wayman and W. L. Wilcock. *Principles of Optics: Electromagnetic Theory of Propagation, Interference and Diffraction of Light*. 7th ed. Cambridge University Press, 1999. DOI: 10.1017/CBO9781139644181.

[37] P. M. van den Berg. 'Acoustic Waves'. In: *Forward and Inverse Scattering Algorithms based on Contrast Source Integral Equations*. John Wiley & Sons, Ltd, 2021. Chap. 2, pp. 79–179. ISBN: 9781119741602. DOI: https://doi.org/10.1002/9781119741602.ch2.

[38] D. W. Marquardt. 'An Algorithm for Least-Squares Estimation of Nonlinear Parameters'. In: *Journal of the Society for Industrial and Applied Mathematics* 11.2 (1963), pp. 431–441. URL: http://www.jstor.org/stable/2098941.

[39] J. Nocedal and S. J. Wright. *Numerical optimization*. Springer, 2006.

[40] J. W. Thorbecke, E. Slob, J. Brackenhoff, J. van der Neut and K. Wapenaar. 'Implementation of the Marchenko method'. In: *GEOPHYSICS* 82.6 (2017), WB29–WB45. DOI: 10.1190/geo2017-0108.1.

[41] M. Davydenko and D. J. Verschuur. 'Including and using internal multiples in closed-loop imaging - Field data examples'. In: *GEOPHYSICS* 83.4 (2018), R297–R305. DOI: 10.1190/geo2017-0533.1.

[42] M. N. Kabir and D. Verschuur. 'Restoration of missing offsets by parabolic Radon transform1'. In: *Geophysical Prospecting* 43.3 (1995), pp. 347–368. DOI: https://doi.org/10.1111/j.1365-2478.1995.tb00257.x.

[43] G. J. van Groenestijn and D. J. Verschuur. 'Estimating primaries by sparse inversion and application to near-offset data reconstruction'. In: *GEOPHYSICS* 74.3 (2009), A23–A28. DOI: 10.1190/1.3111115.

[44] J. Brackenhoff, J. Thorbecke and K. Wapenaar. 'Virtual Sources and Receivers in the Real Earth: Considerations for Practical Applications'. In: *Journal of Geophysical Research: Solid Earth* 124.11 (2019), pp. 11802–11821. DOI: https://doi.org/10.1029/2019JB018485.

[45] J. Brackenhoff. *Rescaling of incorrect source strength using Marchenko Redatuming*. Master's thesis. Available at http://resolver.tudelft.nl/uuid:0f0ce3d0-088f-4306-b884-12054c39d5da. Aug. 2016.

[46] F. Ypma and D. Verschuur. 'Estimating primaries by sparse inversion, a generalized approach'. In: *Geophysical Prospecting* 61.s1 (2013), pp. 94–108. DOI: https://doi.org/10.1111/j.1365-2478.2012.01095.x.

5

CONCLUSION AND FUTURE OUTLOOK

5.1. CONCLUSION

This thesis introduces target-oriented algorithms for seismic imaging and inversion. The proposed LSRTM algorithm effectively handles internal multiple reflections and interactions between the target and overburden, resulting in high-resolution images with reduced artifacts. The thesis discusses the advantages of a target-oriented LSRTM algorithm based on double-focusing, which reduces the spatial and temporal dimensions of the problem, leading to lower computational costs. Additionally, The target-enclosed seismic imaging algorithm accounts for wavefields entering the target region from the upper and lower boundaries, significantly reducing the computational domain while incorporating transmission information. Overall, these target-oriented algorithms provide practical solutions for achieving fast and high-resolution imaging in seismic exploration.

In Chapter 2, a target-oriented LSRTM algorithm is introduced, specifically designed to handle internal multiple reflections in the overburden and interactions between the target and overburden. By solving the Marchenko equations, we obtain the Marchenko double-focused data and the downgoing part of the focusing function. Utilizing these Green's functions and focusing operators, we formulate a Born integral, which serves as the forward modeling operator. Additionally, an adjoint modeling operator is constructed for target-oriented LSRTM. To accurately account for the finite spatial bandwidth caused by the overburden and the finite recording aperture at the acquisition surface, we apply a point-spread function to the reflection response of the target. This formulation results in a target-oriented LSRTM algorithm that can predict the interactions between the target and the overburden and greatly suppress the artifacts caused by these interactions in the target image. Numerical tests with synthetic models show that even in the presence of high-velocity inclusions in the overburden and kinematic errors in the velocity model, our target-oriented LSRTM algorithm is successful in retrieving an artifact-free high-resolution image.

In Chapter 3, a target-enclosed seismic imaging algorithm is proposed, which effect-

ively considers wavefields entering the target region from both upper and lower boundaries. This algorithm offers three key advantages:

1. A significant reduction in the computational domain by limiting it to a smaller region.

2. The elimination of interactions with the portion of the medium above the upper boundary.

3. The ability to incorporate transmission information from the lower boundary to the upper boundary.

However, certain limitations exist in our algorithm. Firstly, it requires access to the lower boundary of the target in order to deploy receivers at the target boundaries. To overcome this, virtual seismology methods such as Marchenko redatuming can be utilized to create virtual receivers around the target region, as demonstrated in a numerical example. Secondly, a background model of the target is needed to accurately predict the arrival time from the lower boundary to the upper boundary. The redatumed wavefields at the lower boundary suffer from kinematic errors, which hinder the recovery of the long wavelength part of the LSRTM image. Addressing this limitation involves reformulating the target-enclosed LSRTM to ensure compatibility with full waveform inversion, enabling the update of the background velocity model.

In Chapter 4, the target-oriented LSRTM algorithm based on double-focusing is applied to a dataset acquired by Equinor in the Norwegian Sea in 1994. The advantages of this algorithm are:

1. Reduction of the spatial dimensions of the problem by choosing a smaller target of interest.

2. Reduction of the temporal dimension of the problem by creating both virtual sources and receivers at the boundary of the target, which leads to lower computational costs.

One can opt for more sophisticated redatuming algorithms such as Marchenko redatuming and double-focusing to create virtual sources and receivers. The advantage of using Marchenko double-focusing compared to a more conventional redatuming algorithm is the ability to predict the internal multiple reflections inside the overburden and a reduction of artifacts due to these multiple reflections. Another critical aspect of working with field data that needs to be carefully taken care of is preprocessing. Marchenko redatuming requires the surface-related multiples to be eliminated. Additionally, we need to scale the reflection response to compensate for an unknown source amplitude and absorption effects. As we showed in the numerical examples section of Chapter 4, an imperfect elimination of surface-related multiples will result in non-physical errors in the double-focused data.

The appendix shows that Marchenko-based target-oriented Full Waveform Inversion can compensate for the need for Hessian matrix inversion by reducing the nonlinearity

due to overburden effects. This is achieved by exploiting Marchenko-based target re-placement to remove the overburden response and its interactions with the target zone from residuals and inserting the response of the updated target zone into the response of the entire medium. With a 1D model, we also show that this method is more robust with respect to prior information than the standard gradient FWI. Similarly to standard Marchenko imaging, the proposed method only requires knowledge of the direct arrival time from a focusing point to the surface and the reflection response of the medium.

In recent years, the seismic exploration community has shifted its focus towards fast and high-resolution imaging and inversion methods, aiming to produce accurate and de-tailed images while accounting for multiple reflections caused by the overburden. How-ever, computing higher-resolution images requires significant computational power and time, necessitating the development of algorithms that can reduce this burden. Our pro-posed target-oriented LSRTM algorithm addresses these challenges by effectively redu-cing the spatial and temporal dimensions of the problem, resulting in higher-resolution images with fewer artifacts. By integrating Marchenko double-focusing with LSRTM, our algorithm not only reduces the computational cost but also mitigates the artifacts caused by internal multiple reflections. With the increasing need for high-resolution im-ages, our target-enclosed LSRTM approach provides a practical solution by focusing on a smaller target region of interest and considering all interactions with the surrounding environment.

5.2. FUTURE OUTLOOK

There are numerous directions for advancing the integration of the Marchenko Green's function retrieval scheme with imaging and inversion problems. The following outlines a few potential directions:

1. One promising direction involves exploring the method's potential to enhance in-version techniques reliant on reflections, such as Full wavefield migration (FWM) and joint migration inversion (JMI). Given that FWM depends on an estimated re-flection response to update the model, our suggested target-oriented algorithm in this thesis can be instrumental in devising a target-oriented FWM algorithm that accounts for internal multiple reflections generated by the overburden. This ap-proach could also enhance the velocity estimation process in JMI.

2. Another direction for study is to utilize Marchenko wavefields as input for the JMI or Full waveform inversion process and attempt to match observed data with pre-dicted data computed using Marchenko-retrieved Green's functions. Achieving this requires updating Marchenko Green's functions iteratively with the evolving velocity model. Utilizing Marchenko Green's functions can reduce the nonlinear-ity of the inverse problem since they already incorporate higher-order scattering events.

3. An additional research focus could be on investigating the role of the Marchenko focusing function as a backward propagator operator as a basis for estimating the

Hessian matrix. The Marchenko focusing function is the inverse of the transmission response between the surface and the focal point within the subsurface. This property offers researchers the advantage of using them as backward propagator operators in imaging problems, potentially reducing the reliance on the Hessian matrix. Like in the case of Marchenko Green's functions, the focusing function needs to be updated after each velocity update.

4. Lastly, there is potential to extend the proposed method outlined in the appendix to accommodate 2D and 3D scenarios. This expansion of the method could enhance its applicability.

5

A

A PROPOSAL FOR MARCHENKO-BASED TARGET-ORIENTED FULL WAVEFORM INVERSION

The Hessian matrix plays an important role in correctly interpreting the multiple scattered wave fields inside the FWI framework. Due to the high computational costs, the computation of the Hessian matrix is not feasible. Consequently, FWI produces overburden-related artifacts inside the target zone model due to the lack of the exact Hessian matrix. We have shown that Marchenko-based target-oriented Full Waveform Inversion can compensate for the need for Hessian matrix inversion by reducing the non-linearity due to overburden effects. This is achieved by exploiting Marchenko-based target replacement to remove the overburden response and its interactions with the target zone from residuals and inserting the response of the updated target zone into the response of the entire medium. We have also shown that this method is more robust with respect to prior information than the standard gradient FWI. Similarly to standard Marchenko imaging, the proposed method only requires knowledge of the direct arrival time from a focusing point to the surface and the reflection response of the medium.

A.1. Introduction

Nowadays, the interest in the inversion of a relatively small target zone of the subsurface, especially for reservoir monitoring applications, is increasing. One of the main inversion techniques for this purpose is full waveform inversion (FWI). The Hessian matrix plays an important role in correctly interpreting the multiple scattered wave fields inside the FWI framework [1]. Due to the high computational costs, the computation of the Hessian matrix is not feasible. Consequently, FWI produces overburden-related artifacts inside the target zone model due to the lack of the exact Hessian matrix.

Different target-oriented approaches have been proposed to compensate for the lack of the exact Hessian: Data redatuming techniques [2] and model domain cost functions [3], to name but a few.

Recently, Marchenko-based target replacement has been introduced as a method to predict the response of the overburden and remove the response of the target zone and insert the response of a new one into the response of the medium. This method only needs a smooth model of the overburden and surface reflection data [4]. With this, one can do target-oriented FWI without data redatuming or computing model domain cost functions.

First, a short description of full waveform inversion is given, followed by a short explanation of Marchenko-based target replacement. Next, we combine these methods to obtain Marchenko-based target-oriented FWI. Finally, this method is validated through a numerical test.

A.2. Full waveform inversion

In general, full waveform inversion is formulated as a partial differential equation-constrained optimization problem in which a data-driven cost function is minimized with the constraint of solving the wave equation [1]. This cost function is defined as the square of the L2 norm of the data residuals:

$$C(\mathbf{m}) = \frac{1}{2} \left\| \mathbf{d}_{pred}(\mathbf{m}) - \mathbf{d}_{obs} \right\|_2^2. \tag{A.1}$$

Here, $\mathbf{d}_{pred}(\mathbf{m})$ is the predicted data vector and $\mathbf{d}_{obs}$ is the observed data vector. To minimize this cost function, gradient-based optimization methods are used. The gradient of this cost function with respect to the model parameters is [5]:

$$\nabla C(\mathbf{m}) = -\mathscr{R}\left[\mathbf{J}^\dagger \Delta \mathbf{d} \right]. \tag{A.2}$$

Here, † symbol means complex conjugate transpose, $\mathbf{J}$ is the Fréchet derivative matrix, $\Delta \mathbf{d}$ is the data residuals vector, and $\mathscr{R}$ denotes the real part. It is possible to find an expression for the Fréchet derivative matrix entries in terms of Greens

A

functions by considering the Born approximation and taking the slowness ($s(\mathbf{x})$ as the model parameter [6]:

$$\frac{\partial d_{pred}(\mathbf{x}_r,\mathbf{x}_s,\omega)}{\partial s(\mathbf{x})} = 2\omega^2 s(\mathbf{x}) G(\mathbf{x}_r,\mathbf{x},\omega) G(\mathbf{x},\mathbf{x}_s,\omega) W(\omega), \tag{A.3}$$

where $G(\mathbf{x},\mathbf{x}_s,\omega)$ and $G(\mathbf{x}_r,\mathbf{x},\omega)$ are Greens functions from source to the scatterer and from scatterer to the receiver location, respectively, and $W(\omega)$ is the source wavelet. Therefore, the gradient at the position of a model parameter can be rewritten as:

$$\nabla C(\mathbf{m}) = 2\mathscr{R}\left[s(\mathbf{x})\int \omega^2 G(\mathbf{x}_r,\mathbf{x},\omega) G(\mathbf{x},\mathbf{x}_s,\omega) W(\omega) \Delta d^* d\omega\right], \tag{A.4}$$

where $*$ means complex conjugate.

A.3. MARCHENKO-BASED TARGET REPLACEMENT

Wapenaar and Staring (2018) [4] devised a method to remove the effects of a target zone inside the medium from the reflection response of the entire medium and insert a changed target zone inside the medium response.

To this end, they employed the one-way reciprocity theorem to derive a representation for the reflection response of the entire medium in terms of responses to the overburden and the target zone:

$$R_B^{\cup}(\mathbf{x}_r,\mathbf{x}_s,\omega) = R_A^{\cup}(\mathbf{x}_r,\mathbf{x}_s,\omega) + \int_{S_1}\int_{S_1} T_A^-(\mathbf{x}_r,\mathbf{x}',\omega) R_b^{\cup}(\mathbf{x}',\mathbf{x},\omega) G_B^{+,+}(\mathbf{x},\mathbf{x}_s,\omega) d\mathbf{x} d\mathbf{x}' \tag{A.5}$$

Here, A, B, and b refer to overburden, entire medium, and target zone, respectively. $R^{\cup}$ is the reflection response of the specified medium from above, T^- denotes the upward propagating transmission response and $G_B^{+,+}(\mathbf{x},\mathbf{x}_s,\omega)$ is the downward propagating Greens function of a downward emitting source. $\mathbf{x}_s$ and $\mathbf{x}_r$ are located just above the surface (S_0). $\mathbf{x}$ and $\mathbf{x}'$ are at S_1, a transparent boundary between the overburden and the target zone.

In order to find the responses of overburden, i.e., medium A, one can apply the Marchenko method to reflection response $R_B^{\cup}$ to find the so-called focusing functions and use Multi-dimensional deconvolution (MDD) to resolve the responses of medium A. The Greens function $G_B^{+,+}(\mathbf{x},\mathbf{x}_s,\omega)$ can be retrieved by inverting the following equation:

$$T_A^+(\mathbf{x}'',\mathbf{x}_s,\omega) = \int_{S_1} C_{Ab}(\mathbf{x}'',\mathbf{x},\omega) G_B^{+,+}(\mathbf{x},\mathbf{x}_s,\omega) d\mathbf{x} \tag{A.6}$$

where

$$C_{Ab}(\mathbf{x}'',\mathbf{x},\omega) = \delta(\mathbf{x}''_H - \mathbf{x}_H) - \int_{S_1} R_A^{\cap}(\mathbf{x}'',\mathbf{x}',\omega) R_b^{\cup}(\mathbf{x}',\mathbf{x}) d\mathbf{x}'. \tag{A.7}$$

A

Here, $R_A^{\cap}(\mathbf{x}'',\mathbf{x}',\omega)$ is the reflection response of the overburden from below, and $\delta(\mathbf{x}''_H - \mathbf{x}_H)$ is a delta function. Moreover, $\mathbf{x}$, $\mathbf{x}'$ and $\mathbf{x}''$ are at S_1 and H denotes the horizontal coordinates.

A.4. Marchenko-based target-oriented Full Waveform Inversion

In each iteration of FWI, a new updated model of the target zone is generated. Using Equation A.5 and modeling just inside the target zone, it is possible to insert the response of the updated target zone into the reflection response of the medium ($R_B^{\cup}$) and use its result as the new predicted data. Let's explain it in more detail. Consider b_i as the updated model of the target zone in i^{th} iteration and denote changed quantities with an overbar. By modeling inside the target zone in each iteration, the reflection response of b_i, $\bar{R}_{b_i}^{\cup}$, is generated. Then, by applying the Marchenko method and Multi-dimensional deconvolution and inverting Equations A.6 and A.7, one can calculate $\bar{G}_B^{+,+}(\mathbf{x},\mathbf{x}_s,\omega)$, $T_A^{-}(\mathbf{x}_s,\mathbf{x}',\omega)$ and $R_A^{\cup}(\mathbf{x}_r,\mathbf{x}_s,\omega)$ with $\mathbf{x}$ and $\mathbf{x}'$ at S_1, and $\mathbf{x}_s$ and $\mathbf{x}_r$ at S_0. Thus:

$$d_{pred_i} = \bar{R}_{B_i}^{\cup}(\mathbf{x}_r,\mathbf{x}_s,\omega), \tag{A.8}$$

and

$$\Delta d_i = \bar{R}_{B_i}^{\cup}(\mathbf{x}_r,\mathbf{x}_s,\omega) - d_{obs}(\mathbf{x}_r,\mathbf{x}_s,\omega). \tag{A.9}$$

Since the first term of the Equation A.5 is the response of the overburden, and it also exists inside the observed data, by computing the data residuals, the response of the overburden is completely removed, and the data residuals only contain the response of the target zone in each iteration.

Up to this point, a method has been presented for making the predicted data without knowing the overburden model and removing the overburden effects from the data residuals. Since the gradient of the cost function needs the Greens functions inside the target zone with a source at S_0 (see Equation A.4, for the next step, these Greens functions need to be calculated.

Let's call the Greens functions inside the target zone with $\mathbf{x}'$ at S_1 and $\mathbf{x}$ variable inside b_i, $\bar{G}_{b_i}^{p,+}(\mathbf{x},\mathbf{x}',\omega)$, and the Greens functions inside the target zone with $\mathbf{x}_s$ at S_0, $\bar{G}_{B_i}^{p,+}(\mathbf{x},\mathbf{x}_s,\omega)$, where superscript p means the whole Greens function, i.e., $G^{p,+} = G^{-,+} + G^{+,+}$. By inverting Equation A.6, it is possible to find $\bar{G}_{B_i}^{+,+}(\mathbf{x}'',\mathbf{x}_s,\omega)$ where $\mathbf{x}''$ is at S_1. Finally, by using $\bar{G}_{b_i}^{p,+}(\mathbf{x},\mathbf{x}',\omega)$ as a propagator, one can calculate $\bar{G}_{B_i}^{p,+}(\mathbf{x},\mathbf{x}_s,\omega)$ as follows:

$$\bar{G}_{B_i}^{p,+}(\mathbf{x},\mathbf{x}_s,\omega) = \int_{S_1} \bar{G}_{b_i}^{p,+}(\mathbf{x},\mathbf{x}',\omega)\bar{G}_{B_i}^{+,+}(\mathbf{x}'',\mathbf{x}_s,\omega)d\mathbf{x}'. \tag{A.10}$$

Considering the Greens functions reciprocity, this Greens function, i.e., $\bar{G}_{B_i}^{p,+}(\mathbf{x},\mathbf{x}_s,\omega)$, is used for both Greens functions inside the Equation A.4. Ultimately, we will end up with the following expression for the target-oriented gradient ($\nabla C(\mathbf{m})_{tar}$):

$$\nabla C(\mathbf{m})_{tar} = 2\mathscr{R}\left[s(\mathbf{x})\int \omega^2 \bar{G}_{B_i}^{p,+}(\mathbf{x}_r,\mathbf{x},\omega)\bar{G}_{B_i}^{p,+}(\mathbf{x},\mathbf{x}_s,\omega)W(\omega)\Delta d^* d\omega\right], \qquad (A.11)$$

A.5. NUMERICAL EXAMPLES

To confirm the effectiveness of the proposed method in this appendix, a comparison between FWI for the entire medium and Marchenko-based target-oriented FWI with a one-dimensional acoustic model with a constant density (Fig. A.1) was done. For this purpose, a gradient descent algorithm is used. A delta function with a time sampling of 10^{-2} seconds is used as the source signature, and the depth sampling is set to 10 meters. For the Target-oriented case, a focusing depth of 2800 meters is chosen. In Figure A.2, a comparison between the retrieved velocity models is shown, and in Figure A.3, residual vectors are compared. In addition, Figure A.4 cost functions are illustrated.
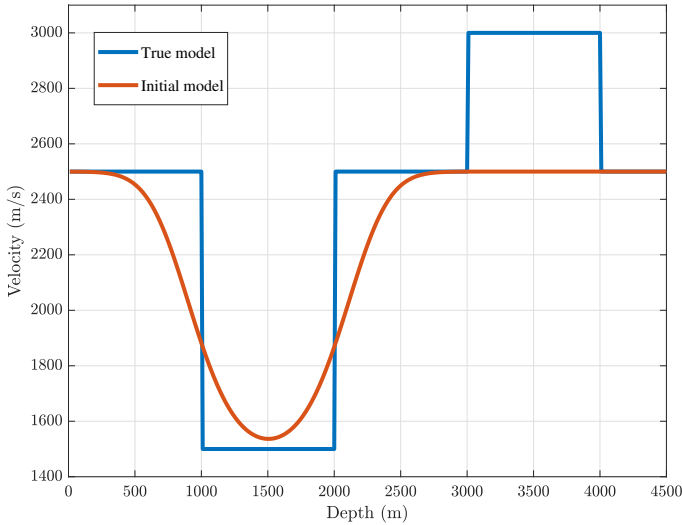

Figure A.1.: True and initial model

These results clearly show that this proposed method can remove the overburden multiple reflection artifacts from the updated model of the target zone. It also produced a more accurate model of the target zone regarding amplitude and reflector positioning.

A.6. CONCLUSION

We have shown that Marchenko-based target-oriented Full Waveform Inversion can compensate for the need for Hessian matrix inversion by reducing the non-linearity
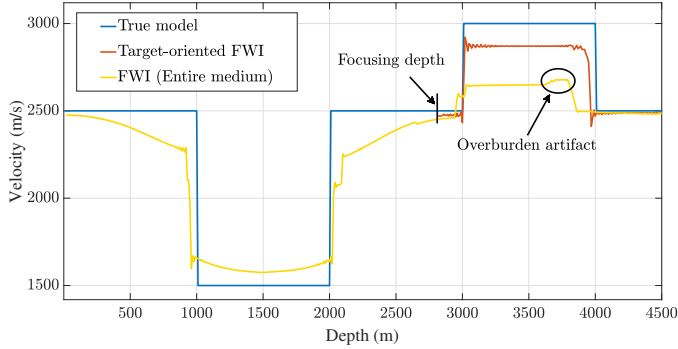
Figure A.2.: Comparison between FWI for the entire medium and Marchenko-based target-oriented FWI. The internal multiple of the overburden created an artifact inside the target zone, but it disappeared from the results of the Target-oriented FWI.
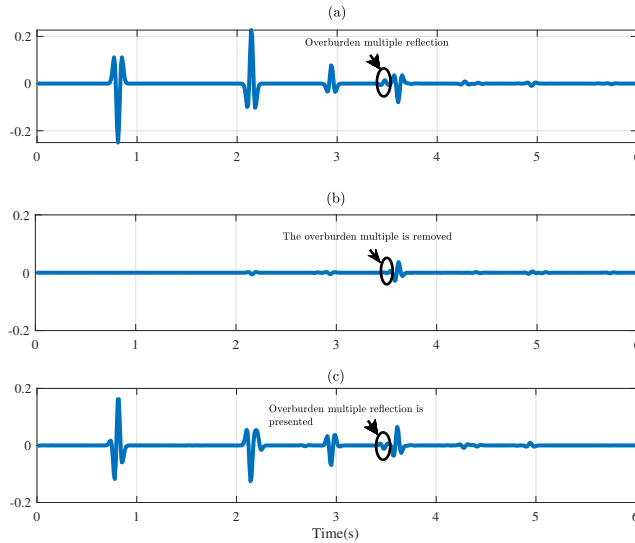
Figure A.3.: Comparison between a) Observed data, b) the residual vector of Target-oriented FWI, and c) the residual vector of FWI for the entire medium. The overburden response is removed from the residuals of the target-oriented FWI by the Marchenko-based target replacement method. Whereas it is still presented in FWI for the entire medium. For better visualization, traces are convolved with a Ricker wavelet with a dominant frequency of 40 Hz.
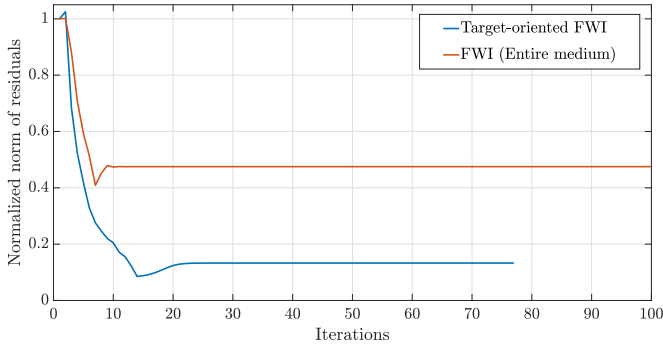
Figure A.4.: Comparison between cost functions

due to overburden effects. This is achieved by exploiting Marchenko-based target replacement to remove the overburden response and its interactions with the target zone from residuals (see figure A.3) and inserting the response of the updated target zone into the response of the entire medium. With a 1D model, we have also shown that this method is more robust with respect to prior information than the standard gradient FWI. Similarly to standard Marchenko imaging, the proposed method only requires knowledge of the direct arrival time from a focusing point to the surface and the reflection response of the medium.

REFERENCES

[1] L. Métivier, R. Brossier, S. Operto and J. Virieux. 'Full Waveform Inversion and the Truncated Newton Method'. In: *SIAM Review* 59.1 (2017), pp. 153–195. DOI: 10.1137/16M1093239.

[2] D. Yang, Y. Zheng, M. Fehler and A. Malcolm. 'Target-oriented Time-lapse Waveform Inversion using Virtual Survey'. In: *SEG Technical Program Expanded Abstracts 2012*. 2012, pp. 1–5. DOI: 10.1190/segam2012-1308.1.

[3] Y. Tang. 'Target-oriented wave-equation least-squares migration/inversion with phase-encoded Hessian'. In: *GEOPHYSICS* 74.6 (2009), WCA95–WCA107. DOI: 10.1190/1.3204768.

[4] K. Wapenaar and M. Staring. 'Marchenko-Based Target Replacement, Accounting for All Orders of Multiple Reflections'. In: *Journal of Geophysical Research: Solid Earth* 123.6 (2018), pp. 4942–4964. DOI: https://doi.org/10.1029/2017JB015208.

[5] J. Virieux and S. Operto. 'An overview of full-waveform inversion in exploration geophysics'. In: *GEOPHYSICS* 74.6 (2009), WCC1–WCC26. DOI: 10.1190/1.3238367.

[6] G. T. Schuster. *SEISMIC INVERSION*. Society of Exploration Geophysicists, 2017.

ACKNOWLEDGEMENTS

I want to express my deep thanks to my respected promotor, **Kees Wapenaar**, whose insight and support have been the bedrock of my doctoral experience. Your faith in my abilities, along with your commitment to fostering my development, has played a pivotal role in finishing this thesis. Your accessibility and eagerness to engage in profound conversations have truly transformed this academic journey. Your profound expertise and enthusiasm for our field have not only influenced the course of this research but have also significantly contributed to my intellectual growth. As we always said, "We love challenges."

In addition to my promotor, my friend and supervisor, **Joost van der Neut**, has played a pivotal role in shaping this research into a meaningful contribution. Your meticulous feedback, endless patience, and unwavering commitment to excellence have not only improved this thesis but have honed my research skills for life. Your ability to identify the strengths and weaknesses of my work and your guidance in navigating the intricate research process have been invaluable. I particularly enjoyed our shared travels across the Netherlands and Spain. It was during some of these train journeys that we brainstormed new ideas and found solutions to our challenges.

I am equally thankful to my other scientific supporters, my promotor **Evert Slob**, **Eric Verschuur**, **Jan Thorbecke**, and **Giovanni Meles** for your unwavering support and invaluable insights, which have added depth and breadth to this thesis. Your expertise and encouragement have been pivotal in addressing the challenges and uncertainties inherent in any substantial research project. Your ability to inspire creative thinking and your relentless pursuit of academic excellence have left a lasting impact on my scholarly pursuits.

I want to express my deep gratitude to my fellow associates at the University of Utrecht and SENAI CIMATEC, namely **Ivan Vasconcelos**, **Leon Diekmann**, **David Vargas**, and **Diego Barrera**. Our productive and enlightening conversations regarding the Marchenko scheme served as a great source of inspiration for me. Regrettably, the COVID-19 lockdowns limited our ability to meet in person more frequently. I truly wish we had more chances to engage in collaborative endeavors.

I wish to express my deep gratitude to my cherished friends who have been a constant source of emotional support and encouragement throughout the challenging phases of this journey. **Siamak** and **Sanaz**, I would not be here if it were not for you, and I am happy that you accepted to be my paranymphs. **Fardad**, we embarked on this scientific journey together 14 years ago, and I'm profoundly grateful for your unwavering support

over the years. **Milad**, **Francis**, **Ali**, **Faezeh**, and **Sepideh**, your addition to my close-knit circle of friends has been a tremendous source of strength during this journey, and for that, I'm truly thankful. Without you, I couldn't have persevered through the hardships of this pursuit. **Morteza**, **Maryam** and **Maryam**, despite the considerable physical distance that has separated us, our friendship has only grown stronger, and we've remained like a close-knit family. **Mohammad**, the memories we've created since our days studying geophysics at the University of Tehran are filled with laughter, and I'm delighted to see you achieving the success you rightfully deserve. **Azin**, your kindness is a rarity in this world, and I sincerely hope that your deserving wishes come true soon. **Shahrzad**, we have known each other since childhood, but only recently did we have the chance to get to know each other better and become good friends. I cannot deny the numerous positive influences that you have had in my life. I wish you success in all your endeavors and that all your wishes come true. To **Alesandro** and **Francesca**, I eagerly anticipate attending your wedding next summer, and I extend my heartfelt wishes for a lifetime filled with happiness and love as you embark on this new journey together. **Mahtab** and **Tina**, I sincerely wish for both of you to find happiness in your individual journeys, and may you each have the strength and resilience to overcome any challenges that come your way. I am also thankful to **Pooneh** and **Lily**, whom I have never met in person, but their virtual presence in my life is invaluable.

I want to convey my heartfelt thanks to my wonderful friends, **Hafez Jafari**, **Sadegh Taghinezhad**, **Liliana Vargas**, **Dieter Werthmüller**, **Ali Golchin**, **Behnaz Fazlali**, **Joeri Brackenhoff**, **Max Holicki**, **David Naranjo Hernandez**, **Amin Rahimi**, **Entela Kane**, **Elahe Kamel**, **Nazife Onaral**, **Hamed Diab Montero**, **Jingming Ruan**, **Aukje Veltmeijer**, **Billy Revelo Obando**, **Eddy Revelo Obando**, **Maria Carrizo Mascarell**, **Rigo**, **Emilio Cecchetti**, **Camille Chapeland**, **Andrea Cuesta Cano**, **Jasper Hupkes**, **Samantha Kim**, **Myrna Staring**, **Florencia Balestrini**, and **Christian Reinicke** for their unwavering support and motivation during the tough times I've faced in this journey.

Dear Mom, your boundless love, unwavering support, and the countless sacrifices you've made have been the very foundation of my life and accomplishments. Your unshakable belief in my potential, even during moments of self-doubt, has been not only my guiding light but also the very essence of my academic journey. This thesis stands as a living tribute to the values you've instilled in me - values of perseverance, diligence, and a relentless pursuit of excellence. It's a small token of the enormous appreciation that resides in my heart, a testament to your unwavering faith in me. Your sacrifices, your guidance, and your profound love have not only shaped my journey but have defined who I am. I am eternally grateful, and I love you beyond words.

Dear Dad, as I reflect on my academic journey, I can't help but think of the countless lessons and values you've imparted to me. This thesis represents not just my academic accomplishments but also a testament to the strong foundation you've provided me with. Your belief in my potential has inspired me in every step of this journey. I'm thankful for your constant presence in my life, and I hope to continue making you proud in all that I do.

I would also like to acknowledge the broader academic community and the numerous scholars whose work has informed and inspired my research. The body of knowledge in our field is a testament to the collective efforts of countless individuals, and I am humbled to contribute to it. Their contributions have provided the foundation upon which my research stands, and for that, I am deeply thankful.

In closing, the completion of this thesis represents a profound milestone in my academic and personal development. It is a testament to the collective efforts of those who have supported and guided me along the way. Each individual mentioned here has contributed to the success of this work in their unique way and I am grateful beyond words. This thesis is a reflection of the collaborative spirit, perseverance, and unwavering support of my mentors, colleagues, friends, and family. Thank you all for being a part of this journey.

CURRICULUM VITÆ

Seyed Mohammad Aydin SHOJA

17-01-1991   Born in Kerman, Iran.

EDUCATION

2008–2015   BSc of Mining Engineering
Shahid Bahonar University of Kerman, Kerman, Iran

2015–2018   MSc of Geophysics
University of Tehran, Tehran, Iran

Thesis: Two-Dimensional Acoustic Time-Domain Full Waveform Inversion Using Multiscale Method
Supervisor: Dr. N. Amini

2018–2023   PhD of Applied Geophysics
Delft University of Technology, Delft, The Netherlands

Thesis: Target-oriented seismic imaging and inversion with Marchenko redatuming and double-focusing
Promotor: Prof. dr. C.P.A. Wapenaar
Promotor: Prof. dr. E.C. Slob

EXPERIENCE

2023–2024   Postdoctoral researcher in Applied Geophysics
Delft University of Technology, Delft, The Netherlands

Supervisor: Dr. D.J. Verschuur

LIST OF PUBLICATIONS

JOURNAL PAPERS

3. A. Shoja, J. van der Neut and K. Wapenaar. 'Target-oriented least-squares reverse-time migration with Marchenko redatuming and double-focusing: Field data application'. In: *Geophysics* (Submitted)

2. A. Shoja, J. van der Neut and K. Wapenaar. 'Target-Enclosed Least-Squares Seismic Imaging'. In: *IEEE Transactions on Geoscience and Remote Sensing* 61 (2023), pp. 1–12. DOI: 10.1109/TGRS.2023.3293725

1. A. Shoja, J. van der Neut and K. Wapenaar. 'Target-oriented least-squares reverse-time migration using Marchenko double-focusing: reducing the artefacts caused by overburden multiples'. In: *Geophysical Journal International* 233.1 (Apr. 2023), pp. 13–32. DOI: 10.1093/gji/ggac438

CONFERENCE ABSTRACTS

3. S. Shoja, J. Van der Neut and K. Wapenaar. 'Reducing the Overburden-Related Artifacts in Target-Oriented Least-Squares Migration by Marchenko Double-Focusing'. In: *Proceedings of 83rd EAGE Annual Conference & Exhibition* 2022.1 (2022), pp. 1–5. DOI: https://doi.org/10.3997/2214-4609.202210258

2. S. Shoja, G. Meles and K. Wapenaar. 'A Proposal for Marchenko-Based Target-Oriented Full Waveform Inversion'. In: *Proceedings of EAGE 2020 Annual Conference & Exhibition Online* 2020.1 (2020), pp. 1–5. DOI: https://doi.org/10.3997/2214-4609.202011020

1. S. Shoja, S. Abolhassani and N. Amini. 'A Comparison between Time-Domain and Frequency-Domain Full Waveform Inversion'. In: *Proceedings of 80th EAGE Conference and Exhibition 2018* 1 (2018), pp. 1–3. DOI: https://doi.org/10.3997/2214-4609.201801667